

**PACKING AND CHARACTERIZATION OF CAPILLARY COLUMNS FOR  
ULTRAHIGH PRESSURE LIQUID CHROMATOGRAPHY**

Justin Miller Godinho

A dissertation submitted to the faculty at the University of North Carolina at Chapel Hill in partial fulfillment of the requirements for the degree of Doctor of Philosophy in the Department of Chemistry.

Chapel Hill  
2016

Approved by:

James W. Jorgenson

Matthew R. Lockett

J. Michael Ramsey

Jillian L. Dempsey

Matthew R. Redinbo

© 2016  
Justin Miller Godinho  
ALL RIGHTS RESERVED

## **ABSTRACT**

Justin Miller Godinho: Packing and Characterization of Capillary Columns for Ultrahigh Pressure Liquid Chromatography  
(Under the direction of James W. Jorgenson)

Improving the performance of the column remains paramount to the continued growth of ultrahigh pressure liquid chromatography. Realization of the theoretical benefits associated with sub-2  $\mu\text{m}$  chromatographic supports requires homogenous packing of the sorbent into a column. This is challenging as dispersion due to transcolumn heterogeneities become increasingly important as packing material continues towards smaller particles.

Although there are many studies on slurry packing, the process is highly dynamic and influenced by many interdependent parameters. The results of these studies have yielded many opinions on the “art” of column packing as opposed to the science. The experiments presented here aim to explore packing variables and associate them with column performance and the packed bed’s microstructure.

Packing heterogeneities associated with slurry concentrations are identified through reconstructions of packed beds via confocal laser scanning microscopy. These heterogeneities are induced by extreme slurry concentrations. They manifest as increased local porosity and particle size segregation at low concentrations, and numerous large packing voids at high slurry concentration. It was found that an intermediate slurry concentration yields repeatable, high efficiency columns by balancing competing packing heterogeneities. These studies inspired use of high slurry concentrations and sonication to achieve highly efficient capillary columns. The

resulting columns exhibit the highest ever efficiency for columns packed with porous particles with reduced plate heights of 1.

These studies on the packed bed microstructure also revealed a trend in increasing interparticle porosity for columns packed with smaller particles. These trends were explored with methods to quantify the column's total liquid volume.

As instruments with increased pressure capabilities become available, longer columns can be implemented. Unfortunately, increasing a column's length while maintaining its efficiency is difficult. In this vein, an on-column detection method to identify local column performance is described. The method allows for non-destructive measurements and may support future studies of column length as a packing variable.

Although the method to pack a sorbent into a column homogeneously is important to overall efficiency, the sorbent's particle size uniformity cannot be overlooked. A hydrodynamic chromatography method is designed and used to size refine a novel macroporous particle material.



## **ACKNOWLEDGEMENTS**

To begin, I need to thank my research advisor, Dr. Jorgenson, for the opportunity to study under him for the last five years. I have learned much from his thoughtful approach to research, and greatly appreciate his encouragement and advice. I am also thankful for my colleagues along the way. Ed Franklin deserves special recognition for his help when I first joined the lab and his continued friendship. Thanks must go to Jim Grinias and Dan Lunn for their help with Chapter 6 and their friendship.

I am very thankful for my collaborators who have helped me reach the results and conclusions presented in this dissertation. Chapter 2 and 3 are the results of an exciting and illuminating collaboration with Professor Ulrich Tallarek and Arved Reising of Philipps-Universität Marburg. The USP material presented in Chapter 6 is the product of collaboration with Dr. Milos Novoty. I have learned much from these collaborators and our discussions on chromatography.

Waters Corporation has been vital to the completion of this dissertation. They have provided expertise, discussion and many of the materials used throughout this dissertation. In particular, I am very thankful for a month long opportunity to research at Waters Corporation. Special thanks must go to Dr. Martin Gilar for hosting me and offering advice on my project, as well as Dr. Fabrice Gritti for insights into my project. While there, I was able to collect the majority of the data presented in Chapter 4 and gain new perspectives on chromatography.

I am thankful for many friends and mentors along the way, and I would be remiss not to

thank my former professors at Davidson college Dr. Cindy Hauser and Dr. Felix Carroll. I also must thank my grandparents, brother and parents for their unwavering support and encouragement. I am so very thankful for my parents and all they have done to get me here. Finally, I must thank my wife, Kelly, who has always been there for me and helped me with everything.

## TABLE OF CONTENTS

LIST OF TABLES .....	xii
LIST OF FIGURES .....	xiii
LIST OF ABBREVIATIONS .....	xx
LIST OF SYMBOLS .....	xxii
Chapter 1. Theory and Background .....	1
1.1 Overview .....	1
1.2 Chromatographic Theory .....	1
1.2.1 Chromatographic Separations .....	1
1.2.2 Separation Efficiency .....	3
1.2.3 Van Deemter Theory .....	3
1.2.3.1 A-term .....	5
1.2.3.2 B-term .....	6
1.2.3.3 C-term .....	6
1.2.3.4 Limitations of the van Deemter Equation .....	7
1.3 Correction for Interstitial Velocities .....	7
1.4 Ultrahigh Pressure Liquid Chromatography (UHPLC) .....	8
1.5 Scope of the Dissertation .....	9
1.6 Figures .....	10
1.7 References .....	11

Chapter 2. Investigation of Slurry Concentration's Effect on Column Performance .....	12
2.1 Introduction .....	12
2.2 Materials and Methods .....	13
2.2.1 Materials and Methods for the Preparation of UHPLC Columns and Characterization of Their Chromatographic Performance .....	13
2.2.2 Methods to Image and Analyze Packing Microstructure .....	13
2.3 Results and Discussion .....	14
2.3.1 Preliminary Studies on Slurry Concentration's Effect on Column Performance .	14
2.3.2 Columns Packed with 1.3 $\mu\text{m}$ BEH Material .....	18
2.3.3 Columns Packed with 1.9 $\mu\text{m}$ BEH Material .....	23
2.4 Conclusions .....	26
2.5 Tables .....	28
2.6 Figures .....	30
2.7 References .....	53
Chapter 3. Implementation of High Slurry Concentration and Sonication to Pack High- Efficiency, Meter-Long Capillary Ultrahigh Pressure Liquid Chromatography Columns .....	55
3.1. Introduction .....	55
3.2. Materials and Methods .....	56
3.2.1. Chemicals, Materials and Methods .....	56
3.3. Results and Discussion .....	58
3.4. Conclusions .....	62
3.5 Tables .....	63
3.6 Figures .....	64
3.7 References .....	68

Chapter 4. Total Liquid Volume as a Function of Particle Size and Mobile Phase .....	70
4.1 Introduction.....	70
4.1.1 Introduction of Variables Referenced in the Following Discussion.....	71
4.2 Methods for the Determination of the Total Liquid Volume in a Column.....	73
4.2.1 Unretained Neutral Marker .....	73
4.2.2 Pycnometry .....	74
4.2.3 Interpretation of Measurements .....	75
4.3 Measurement of the Total Liquid Fraction for 1.3 $\mu$ m BEH Capillary Columns .....	75
4.3.1 Materials and Methods.....	76
4.3.2 Discussion of CLSM Results and Confirmation by Pycnometry .....	76
4.3.3 Anomalous Total Volume Percentages as Measured by an Unretained Marker ..	78
4.4 Total Column Liquid Volume as a Function of Mobile Phase, Particle Size and Bonding.....	81
4.4.1 Modifications to Materials and Methods .....	81
4.4.2 Effects of Mobile Phase Percentage, Particle Size, and Bonding.....	82
4.5 Conclusions.....	85
4.6 Tables.....	86
4.7 Figures.....	92
4.8 References.....	104
Chapter 5. Impact of Column Length and Methods to Analyze Localized Axial Heterogeneity Amongst Subsections of Packed Capillary Columns.....	105
5.1 Introduction.....	105
5.2 Materials and Methods.....	106
5.3 Axial Heterogeneities for “Optimized” Slurry Concentrations .....	107

5.4	Theory of Additive Plates .....	108
5.5	On-Column Detection .....	109
5.5.1	NIRF as a Method for On-Column Detection.....	110
5.5.1.1	Materials and Methods.....	110
5.5.1.2	Results and Discussion .....	111
5.5.2	On-Column UV Detection: Method and Proof of Concept .....	112
5.5.2.1	Materials and Methods.....	112
5.5.2.2	Results and Discussion .....	112
5.6	Conclusions.....	114
5.7	Figures.....	116
5.8	References.....	126
Chapter 6. Hydrodynamic Chromatography as a Preparative Technique for Silica Supports Used in UHPLC .....		127
6.1	Introduction.....	127
6.1.1	Theory of Hydrodynamic Chromatography.....	127
6.1.2	HDC as a Preparative Technique.....	129
6.2	Materials and Methods.....	129
6.2.1	Preparation of a HDC Column for Preparative Scale Size Refinement.....	129
6.2.2	Implementation of the HDC Column.....	130
6.2.3	HDC Column Characterization and Analysis of Silica Particles.....	131
6.3	Results and Discussion .....	132
6.3.1	Determination of Mobile Phase Suitability by Separation of Size Standards ....	132
6.3.2	HDC Column and Packing Quality.....	133
6.3.3	Particle Recovery for NPS Standards .....	134

6.3.4	Size Refinement and Recovery of 1.0 $\mu\text{m}$ BEH Particles by HDC .....	134
6.3.5	Refinement of Ultrasonic Spray Pyrolysis Particles .....	135
6.4	Conclusions .....	136
6.5	Tables .....	138
6.6	Figures .....	140
6.7	References .....	149
APPENDIX 1: MATERIALS AND METHODS .....		150
1.	Chemicals and Materials .....	150
2.	Chemicals and Methods Used for Slurry Packing and Column Creation .....	150
3.	Column Characterization .....	151
4.	References .....	153

## LIST OF TABLES

<b>Table 2-1.</b> Results of the analyses of packing defects from the preliminary of slurry concentration studies.....	28
<b>Table 2-2.</b> Values of the integral porosity deviation (IPD, Equation 2-1). (a) Calculated with the integration limits of $r = 0 \text{ }\mu\text{m}$ to $r = 10.5 \text{ }\mu\text{m}$ (b) Calculated with the integration limits from the first zero transition ( $\sim 1/3 d_p$ ) up to $r = 10.5 \text{ }\mu\text{m}$ (c) Biased value due to an optical artifact in the image stack. ....	29
<b>Table 3-1.</b> Reduced van Deemter terms for all six columns characterized in this study. ....	63
<b>Table 4-1.</b> The total liquid volume percentage as a function of %MeCN while using uracil as a dead time marker. The dimensions and flow rates for these columns were as follows: $1.7 \text{ }\mu\text{m}$ C18 BEH (9.95 cm x $75 \text{ }\mu\text{m}$ i.d., $0.38 \text{ }\mu\text{L/min}$ ), $1.36 \text{ }\mu\text{m}$ C18 BEH (a 9.8 cm x $75 \text{ }\mu\text{m}$ i.d., $0.15 \text{ }\mu\text{L/min}$ ), $0.96 \text{ }\mu\text{m}$ C18 BEH (8 cm x $75 \text{ }\mu\text{m}$ i.d., $0.15 \text{ }\mu\text{L/min}$ ). ....	86
<b>Table 4-2.</b> Dimensions of the columns and results of the total liquid fraction in a 100% MeCN mobile phase with toluene used as a dead time marker. ....	87
<b>Table 4-3.</b> Dimensions of the columns and results of total liquid fraction in a 100% THF mobile phases with toluene used as the dead time marker. ....	88
<b>Table 4-4.</b> Presentation of porosity fractions calculated from an assumption of $\epsilon_{interparticle}$ from previous CLSM studies. ....	89
<b>Table 4-5.</b> Total liquid volume of a column expressed as a percentage for a $9.5 \text{ cm} \times 75 \text{ }\mu\text{m}$ i.d. column packed with $1.7 \text{ }\mu\text{m}$ HILIC material. In all cases toluene was used as the dead time marker and the flow rate was $0.38 \text{ }\mu\text{L/min}$ . ....	90
<b>Table 4-6.</b> Presentation of porosity fractions calculated from an assumption of $\epsilon_{interparticle}$ from previous CLSM studies and a report of a manufacturer's value for $\epsilon_{intraparticle}$ . ....	91
<b>Table 6-1.</b> Presentation of the mass injected, mass recovered and the overall percent yield for NPS standards used to characterize the column and porous BEH material. ....	138
<b>Table 6-2.</b> Results of USP particle size refinement with HDC. The data is presented in terms of the first and second half of the eluting particle peak with individual notation of average particle diameter of the three different microstructure populations. Comparison is also made between the results of a single injection and a repeated throughput of 10 injections in a row. For comparison the particle diameter is provided for each particle type for the raw, unrefined material. ....	139



## LIST OF FIGURES

<b>Figure 1-1.</b> Representation of a packed bed presenting five regimes for A-term broadening: 1) transchannel 2) short-range interchannel 3) long-range interchannel 4) transcolumn 5) transparticle.....	10
<b>Figure 2-1.</b> Representation of CLSM image acquisition and enhancement A) represents an orthoslice view of the raw CLSM images recorded from 75 $\mu\text{m}$ i.d. capillary columns. Here three slices are shown. B) Shows the final 3D rendering of the processed images. This image presents a model of the packed section of capillary bed. Figures 2-1 C, D, and E present the stepwise image results from raw data, C, to restored data, E. Figure 2-1, D shows an image within the process of enhancement and removal of noise (intensity variations, bleaching, and deconvolution to increase contrast). .....	30
<b>Figure 2-2.</b> Example of how voids were determined. The restored image on the left panel was overlaid with the segmented image. Within this segmented image a sphere is inscribed that completely fills the void space. In this example, the column is packed with a 40 mg/mL slurry concentration of 1.3 $\mu\text{m}$ BEH particles. The inscribed sphere has a diameter of 1.62 $\mu\text{m}$ and could accommodate 99% of the 1.3 $\mu\text{m}$ BEH particle population. ....	31
<b>Figure 2-3.</b> Reduced plate height curves for HQ for beds packed with low and high slurry concentrations of 1.9 $\mu\text{m}$ and 1.7 $\mu\text{m}$ BEH material. ....	32
<b>Figure 2-4.</b> Plots for columns packed with 1.9 and 1.7 $\mu\text{m}$ BEH materials A) Radial porosity profiles in the wall region for the reconstructed sections of the capillary columns. B) Relative mean particle size as a function of position from the wall.....	33
<b>Figure 2-5.</b> Reduced plate height curves for HQ. The reduced van Deemters are for columns packed with low and high slurry concentrations of 1.9 $\mu\text{m}$ Kinetex material. ....	34
<b>Figure 2-6.</b> Plots for columns packed with 1.9 $\mu\text{m}$ Kinetex A) Radial porosity profiles in the wall region for the reconstructed sections of the capillary columns. B) Relative mean particle distance as a function of position from the wall with the results of the 1.9 $\mu\text{m}$ BEH columns overlaid. ....	35
<b>Figure 2-7.</b> Minimum plate heights, $H_{min}$ , for the entire set of columns (34 cm x 75 $\mu\text{m}$ i.d.) packed with 1.3 $\mu\text{m}$ BEH particles using HQ as the test analyte. The points in red represent the columns reconstructed with CLSM. ....	36
<b>Figure 2-8.</b> Minimum plate heights, $H_{min}$ , for the entire set of columns packed with 1.3 $\mu\text{m}$ BEH particles. The results for the test analyte HQ are plotted in black and the more retained analyte 4-MC ( $k' = 0.6$ ) are plotted in black. ....	37

<b>Figure 2-9.</b> Plate height curves, $H$ , vs. the average velocity, $u_{av}$ , for the three reconstructed columns packed 1.3 $\mu\text{m}$ BEH particles. The curves are the results for HQ. ....	38
<b>Figure 2-10.</b> Example chromatogram for the column packed with a 40 mg/mL slurry of 1.3 $\mu\text{m}$ BEH. ....	39
<b>Figure 2-11.</b> Particle size distribution (PSD) analysis for the 1.3 $\mu\text{m}$ BEH particles. CLSM Imaging based sizing is plotted in comparison to SEM based measurements. ....	40
<b>Figure 2-12.</b> Radial distribution of relative porosity used to calculate the integral porosity deviation (IPDs) for the three analyzed 1.3 $\mu\text{m}$ BEH columns. The dashed line represents the limit of integration, 10.5 $\mu\text{m}$ . ....	41
<b>Figure 2-13.</b> Number of voids for the three reconstructed 1.3 $\mu\text{m}$ BEH column bed sections per 1000 packed particles (A) Absolute and (B) Cumulative number of voids depending on their diameter. ....	42
<b>Figure 2-14.</b> 3D visualization of larger voids in the CLSM-based reconstructions of the 1.3 $\mu\text{m}$ BEH columns. Green spheres represent voids that can accommodate 10-50% of the SEM based PSD, Yellow 50-90%, and red $\geq 90\%$ of the PSD. The top panel shows the structures with optically opaque particles while the bottom panel presents transparent particles to highlight the larger voids in the packing. ....	43
<b>Figure 2-15.</b> XZ-views of the reconstructions of the 10 and 40 mg/mL 1.3 $\mu\text{m}$ BEH columns including the larger voids in the CLSM-based reconstructions. Green spheres represent voids that can accommodate 10-50% of the SEM based PSD, yellow 50-90%, and red $\geq 90\%$ of the PSD. ....	44
<b>Figure 2-16.</b> Examples of large voids identified during the bed reconstruction of the 1.3 $\mu\text{m}$ BEH column packed with a slurry concentration of 40 mg/mL. ....	45
<b>Figure 2-17.</b> A) Minimum reduced plate heights, $h_{min}$ , for the entire set of columns packed with 1.9 $\mu\text{m}$ BEH particles using HQ as the test analyte. The points in red represent the columns reconstructed with CLSM. B) Plate height curves, $H_{min}$ , vs. the average velocity, $u_{av}$ , for the three reconstructed columns packed with 1.9 $\mu\text{m}$ BEH particles. The curves are the results for HQ. ....	46
<b>Figure 2-18.</b> Particle size distribution (PSD) analysis for the 1.9 $\mu\text{m}$ BEH particles. CLSM imaging based sizing is plotted in comparison to SEM based measurements. ....	47
<b>Figure 2-19.</b> A) Radial porosity profiles for the analyzed 1.9 $\mu\text{m}$ BEH columns B) Plot of the mean relative particle size as a function of radial position. ....	48

<b>Figure 2-20.</b> Radial distribution of relative porosity used to calculate the integral porosity deviation (IPDs) for the three analyzed 1.9 $\mu\text{m}$ BEH columns. ....	49
<b>Figure 2-21.</b> Plot of the IPD values extracted from Figure 2-20 as a function of distance from the column wall of the three 1.9 $\mu\text{m}$ BEH columns. ....	50
<b>Figure 2-22.</b> Number of voids for the three reconstructed 1.9 $\mu\text{m}$ BEH column bed sections per 1000 packed particles (A) Absolute and (B) Cumulative number of voids depending on their diameter. ....	51
<b>Figure 2-23.</b> Visualization of larger voids in the CLSM-based reconstructions of the three 1.9 $\mu\text{m}$ BEH columns. Green spheres represent voids that can accommodate 10-50% of the SEM based PSD, Yellow 50-90%, and red $\geq 90\%$ of the PSD.....	52
<b>Figure 3-1.</b> Example chromatogram for one of the three columns packed with sonication and run at 1630 bar. This column is represented by red triangles in Figures 3-3 and 3-4. Peaks from left to right are L-ascorbic acid, hydroquinone, resorcinol, catechol and 4-methyl catechol. ....	64
<b>Figure 3-2.</b> Example enlargement of the hydroquinone peak used for the reduced plate height curves in Figure 3-3. This peak is enlarged from Figure 3-1. The experimental data is plotted in black, the Gaussian fit in blue and the residuals are plotted in red. A black dashed line is overlaid at 0 signal for reference. ....	65
<b>Figure 3-3.</b> Plot of reduced van Deemter fits for hydroquinone on each of the 6, 1-meter long columns. Columns packed with sonication are presented in red while columns prepared without sonication are plotted in black. Marker shapes (circles, squares and triangles) distinguish each column within the parameters represented by color. ....	66
<b>Figure 3-4.</b> Plot of the linear velocity of the dead time marker, L-ascorbic acid, against pressure drop normalized for column length. Columns packed with sonication are presented in red while columns prepared without sonication are plotted in black. Marker shapes (circles, squares and triangles) distinguish each column within the parameters represented by color. ....	67
<b>Figure 4-1.</b> Radial porosity profiles for columns packed with 1.3 $\mu\text{m}$ BEH particles at three slurry concentrations. The interstitial void volume fraction as a function of position is plotted from the wall of the capillary column to 18 $\mu\text{m}$ into the capillary column.....	92
<b>Figure 4-2.</b> SEM image of an extruded section of the bed for a 15 mg/mL packing of 1.3 $\mu\text{m}$ BEH particles. The extruded portion of the packed bed was dried, mounted and exposed to a strong nitrogen stream. A rigid bed structure is firmly anchored and indicative of particle cohesion. ....	93
<b>Figure 4-3.</b> Particle size distribution for the 1.3 $\mu\text{m}$ BEH particles as measured by CLSM	

images and SEM images.....	94
<b>Figure 4-4.</b> Plot of $t_m$ vs. the gauge pressure (actual applied pressure is multiplied by 1038) for 24 mg/mL, 33.6 cm x 75 $\mu$ m column packed with 1.3 $\mu$ m BEH particles used for pycnometry. Points plotted in black were from the original column characterization. The red point is from the column stability confirmation approximately two years later.....	95
<b>Figure 4-5.</b> Plot of flow rate vs. the gauge pressure (actual applied pressure is multiplied by 1038) for 24 mg/mL, 33.6 cm x 75 $\mu$ m column packed with 1.3 $\mu$ m BEH particles used for pycnometry.....	96
<b>Figure 4-6.</b> Plot of $\epsilon_T$ vs. the gauge pressure (actual applied pressure is multiplied by 1038) for 24 mg/mL, 33.6 cm x 75 $\mu$ m column packed with 1.3 $\mu$ m BEH particles used for pycnometry. Points plotted with circles are the direct resultant of experimental measurements. Points plotted in squares represent a 71 ppm/bar pressure correction for mobile phase compressibility. Points plotted in red represent the result of experiments conducted approximately 2 years after initial characterization. Dashed red lines are lines of best fit. Notably, at low pressure both intercept at nearly the same $\epsilon_T$ .....	97
<b>Figure 4-7.</b> Plot of three different dead time markers: ascorbic acid (blue), thiourea (red), sodium nitrate (purple). All samples were run in 50:50 water:MeCN for 24 mg/mL, 33.6 cm x 75 $\mu$ m column packed with 1.3 $\mu$ m BEH particles later used for pycnometry. Detection was conducted by UV absorbance at 230 nm with a 75 $\mu$ m capillary butt connected to the end of the capillary column.....	98
<b>Figure 4-8.</b> Chromatogram for the 24 mg/mL, 33.6 cm x 75 $\mu$ m column packed with 1.3 $\mu$ m BEH particles used for pycnometry. The mobile phase used is 80:20 water:MeCN + 0.1% TFA and run at 21 kpsi. Ascorbic acid is plotted in red and sodium nitrate is plotted in blue. Detection was conducted at 230 nm with a 75 $\mu$ m i.d. capillary butt connected to the capillary column.....	99
<b>Figure 4-9.</b> Chromatogram for the 24 mg/mL, 33.6 cm x 75 $\mu$ m column packed with 1.3 $\mu$ m BEH particles used for pycnometry. The mobile phase used is 150 mM NaCl in 80:20 water:MeCN + 0.1% TFA and run at 15 kpsi. Ascorbic acid is plotted in red and sodium nitrate is plotted in blue. Detection was conducted at 230 nm with a 75 $\mu$ m i.d. capillary butt connected to the capillary column. ....	100
<b>Figure 4-10.</b> Plot of flow rate vs. the gauge pressure (actual applied pressure is multiplied by 1038) for 24 mg/mL, 33.6 cm x 75 $\mu$ m column packed with 1.3 $\mu$ m BEH particles used for pycnometry. Colors of points represent the following methods: black- normal unaided measurements, red- microscope aided measurements, blue-saturated atmosphere aided measurements. The gray dashed line is the line of best fit for the normal, unaided measurements.....	101

<b>Figure 4-11.</b> Plot of flow rate vs. the gauge pressure (actual applied pressure is multiplied by 1038) for 24 mg/mL, 33.6 cm x 75 $\mu$ m column packed with 1.3 $\mu$ m BEH particles used for pycnometry. Flow rate measurements were conducted by the “bubble method” in 50:50 water:MeCN and presented in red, while flow rate measurements made with a 10 $\mu$ L capillary are presented in black.....	102
<b>Figure 4-12.</b> Plot of flow rate vs. the gauge pressure (actual applied pressure is multiplied by 1038) for 24 mg/mL, 33.6 cm x 75 $\mu$ m column packed with 1.3 $\mu$ m BEH particles later used for pycnometry. Flow rate measurements were conducted by the “bubble method” in 80:20 water:MeCN. ....	103
<b>Figure 5-1.</b> Plotted in black is the performance of a 100 cm x 75 $\mu$ m i.d. column packed with 1.3 $\mu$ m BEH material in a slurry with a concentration of 20 mg/mL. This column was subsequently sectioned into three subsections representing the inlet (25 cm and plotted in green), middle (32.5 cm and plotted in blue), and outlet (31 cm and plotted in red) of the original 100 cm column.....	116
<b>Figure 5-2.</b> Overlay of the reduced van Deemter plots for the outlet subsection (31 cm long column and plotted in red in Figure 5-1, red) of the original 100 cm long column and the 34 cm long column used in the slurry optimization experiments in Chapter 2 (gray). Both columns were packed with 20 mg/mL slurries of 1.3 $\mu$ m BEH particles. ....	117
<b>Figure 5-3.</b> Diagram of the NIRF instrument. The housing is shown in tan and the components are as follows: A) Si photodiode with a spectral range of 320 to 1100 nm and peak sensitivity at 960 nm, B) plano-convex lenses, 15 mm diameter x 15 mm focal length, C) 832-center wavelength, 25 mm diameter, 37 nm bandwidth, optical density 6, fluorescence filter, D) capillary column positioning during detection, E) 780 nm center wavelength, 10 nm full width at half max, 25 mm diameter bandpass interference filter, F) 780 nm laser.....	118
<b>Figure 5-4.</b> Structure of IR 125.....	119
<b>Figure 5-5.</b> Example of an NIRF on-column detection experiment on a 101 cm x 75 $\mu$ m long capillary was packed with 1.9 $\mu$ m BEH particles. The first eluted peak occurs at approximately 21 minutes and corresponds to a length of 17 cm from the inlet. Each subsequent peak is the result of detection further down the column’s length. Noise spikes are seen between each peak and are due to the movement of the capillary through the NIRF detector. ....	120
<b>Figure 5-6.</b> Plot of axial position of the on-column detection measurement for the IR125 peak vs. the time elapsed in the experiment. Data is extracted from Figure 5-5. The plot displays deviation from linearity and increasing band velocity. ....	121
<b>Figure 5-7.</b> Plot of velocity of HQ (detection position vs. elapsed experimental time). Linearity is seen, indicating a constant velocity of the analyte across the length of	

column for a 106.4 cm x 75 $\mu\text{m}$ column packed with 1.9 $\mu\text{m}$ BEH. ....	122
<b>Figure 5-8.</b> Plot of $h_i$ as a function of window position in cm from the column's inlet for an on-column UV detection experiment on a 106.4 cm x 75 $\mu\text{m}$ column packed with 1.9 $\mu\text{m}$ BEH particles. Here $\bar{h}$ is 4.26 (dashed red line) and $h_L$ is 4.06 as measured by electrochemical detection. ....	123
<b>Figure 5-9.</b> Plot of $h_i$ as a function of window position in cm from the column's inlet for an on-column UV detection experiment for an 80 cm x 75 $\mu\text{m}$ column packed with 1.9 $\mu\text{m}$ BEH particles. Here $v = 3.88$ , and $h_L = 5.29$ while $\bar{h} = 5.11$ (dashed red line). This experiment represents performance in the c-term dominated region. ....	124
<b>Figure 5-10.</b> Plot of $h_i$ as a function of window position in cm from the column's inlet for an on-column UV detection experiment for an 80 cm x 75 $\mu\text{m}$ column packed with 1.9 $\mu\text{m}$ BEH particles. Here $v = 0.76$ , and $h_L = 3.83$ while $\bar{h} = 3.76$ (dashed red line). This experiment represents performance in the b-term dominated region. ....	125
<b>Figure 6-1.</b> HDC runs of 0.5 $\mu\text{m}$ (red) and 1.5 $\mu\text{m}$ (blue) NPS standards. Here water is used as a mobile phase. For comparison the eluted peak for urea is plotted in black. ....	140
<b>Figure 6-2.</b> HDC runs of 0.5 $\mu\text{m}$ (red) and 1.5 $\mu\text{m}$ (blue) NPS standards with 1 mM ammonium hydroxide used as a mobile phase. For comparison the eluted peak for urea is plotted in black. ....	141
<b>Figure 6-3.</b> HDC separation of 1.5 and 0.5 $\mu\text{m}$ NPS size standards when injected together (blue). Overlaid are reference chromatograms for injections containing just one of the two size standards (1.5 $\mu\text{m}$ in black and 0.5 $\mu\text{m}$ in red). ....	142
<b>Figure 6-4.</b> Histograms for the data representing the refinement of 0.9 $\mu\text{m}$ BEH material. Figure A represents the raw PSD while frames B and C represent the 1 <sup>st</sup> and 2 <sup>nd</sup> halves of the eluted BEH peak respectively. A clear difference in PSD is seen as a function of fractionation. The number of particles sized for each panel: A) 101 B) 112 C) 105. ....	143
<b>Figure 6-5.</b> Overview image for the diversity in particle structure created when synthesizing sub-2 $\mu\text{m}$ particles by USP. The three particle types characterized in the discussion presented herein are circled: macroporous (green), hybrid (blue), microporous (red). ....	144
<b>Figure 6-6.</b> Overlay of the eluted USP peak (green), on HDC runs of 0.5 (red) and 1.5 (blue) $\mu\text{m}$ NPS, and urea (black) demonstrating the suitability of the column and method for material in this size range. ....	145

<b>Figure 6-7.</b> Example 1 hour run with staggered injections for the refinement of USP material. For each two peak pair, the first eluting peak was split into a 1 <sup>st</sup> and 2 <sup>nd</sup> fraction at the peak's maximum intensity. The second peak in each pair represents the elution of urea. ....	146
<b>Figure 6-8.</b> Panel A is an representative SEM image of the 1 <sup>st</sup> eluting half of the USP peak. A clear population of larger, hybrid material is detectable by eye. Panel B is a representative SEM image for the 2 <sup>nd</sup> half of the eluting USP peak and portrays a significant number of smaller particles that do not have the characteristic macroporous features. ....	147
<b>Figure 6-9.</b> Graphical representations of the fraction of population for the 1 <sup>st</sup> and 2 <sup>nd</sup> half of a fractioned USP peak. The results of 10 repeated injects are also shown and all are compared to the raw material. Green represents the larger macroporous material, blue the hybrid, and red the microporous. The number of sized particles is listed in Table 6-2. ....	148

## LIST OF ABBREVIATIONS

3D	Three dimensional
4-MC	4-methyl catechol
AA	Ascorbic acid
BEH	Bridged-ethyl hybrid
C18	n-Octadecyl
CAT	Catechol
CLSM	Confocal laser scanning microscopy
HDC	Hydrodynamic chromatography
HETP	Height equivalent to a theoretical plate
HPLC	High pressure liquid chromatography
HILIC	Hydrophilic interaction chromatography
HQ	Hydroquinone
IPD	Integral porosity deviation
i.d.	Inner diameter
LC	Liquid chromatography
MeCN	Acetonitrile
NIRF	Near infrared fluorescence
NPS	Nonporous silica
o.d.	Outer diameter
PEEK	Polyether ether ketone
PSD	Particle size distribution
PTFE	Polytetrafluoroethylene



RES	Resorcinol
RSD	Relative standard deviation
SEM	Scanning electron microscopy
SPV	Specific pore volume
TFA	Trifluoroacetic acid
THF	Tetrahydrofuran
UHPLC	Ultra-high pressure liquid chromatography
USP	Ultrasonic spray pyrolysis
UV	Ultraviolet

## LIST OF SYMBOLS

$A$	Multiple flow path van Deemter coefficient
$a$	Reduced multiple flow path van Deemter coefficient
$B$	Longitudinal diffusion van Deemter coefficient
$b$	Reduced longitudinal diffusion van Deemter coefficient
$C$	Resistance to mass transfer van Deemter coefficient
$c$	Reduced resistance to mass transfer van Deemter coefficient
$C_{HDC}$	Hydrodynamic chromatography quadratic correction term
$C_M$	Concentration of analyte in mobile phase
$C_m$	Resistance to mass transfer in the mobile phase van Deemter Coefficient
$C_S$	Concentration of analyte in stationary phase
$C_s$	Resistance to mass transfer in stationary phase van Deemter coefficient
$C_{slurry}$	Particle slurry concentration
$C_{sm}$	Resistance to mass transfer in the stagnant mobile phase van Deemter coefficient
$D_M$	Diffusion coefficient in the mobile phase
$D$	Diffusion coefficient
$d_c$	Diameter of the column
$d_p$	Particle diameter
$d_{p,HDC}$	Hydrodynamic chromatography packing material particle diameter
$F$	Flow rate
$H$	Height equivalent to a theoretical plate

$H_A$	Height equivalent to a theoretical plate due to multiple flow path broadening
$H_{A,Giddings}$	Height equivalent to a theoretical plate due to multiple flow path broadening in the Giddings model
$H_B$	Height equivalent to a theoretical plate due to longitudinal diffusion
$H_C$	Height equivalent to a theoretical plate due to resistance to mass transfer
$H_i$	Height equivalent to a theoretical plate due to a column subsection
$H_L$	Height equivalent to a theoretical plate for the entire column length
$H_{min}$	Minimum height equivalent to a theoretical plate
$\bar{H}$	Weighted average of height equivalent to a theoretical plate for each column subsection
$h$	Reduced height equivalent to a theoretical plate
$h_i$	Reduced height equivalent to a theoretical plate due to a column subsection
$h_L$	Reduced height equivalent to a theoretical plate for the entire column length
$h_{min}$	Minimum reduced height equivalent to a theoretical plate
$\bar{h}$	Weighted average of reduced height equivalent to a theoretical plate for each column subsection
$i. d.$	Inner diameter
$K$	Partition coefficient
$k'$	Retention factor
$L$	Column length
$l_i$	Length of a column subsection
$N$	Number of theoretical plates
$n_m$	Number of moles in mobile phase

$n_s$	Number of moles in stationary phase
$r$	Distance from column wall (radial position)
$r_c$	Column (capillary column) radius
$r_{c,HDC}$	Interstitial capillary radius in a particle packed hydrodynamic chromatography column
$r_p$	Particle radius
$t_M$	Time analyte spends in mobile phase
$t_S$	Time analyte spends in stationary phase
$t_o$	Column dead (void) time
$t_R$	Analyte retention time
$t_p$	Particle elution time in hydrodynamic chromatography
$u$	Mobile phase velocity
$u_{av}$	Average mobile phase velocity
$u_i$	Interstitial mobile phase velocity
$u_{measured}$	Measured mobile phase velocity
$u_{optimal}$	Optimal mobile phase velocity
$u_p$	Particle velocity in hydrodynamic chromatography
$u_r$	Local velocity at radial position $r$
$V_{blank}$	Volume of empty column
$V_L$	Total liquid volume in a column
$V_M$	Volume of mobile phase
$V_o$	Total liquid volume within a packed column
$V_{particle}$	Volume occupied by the particle

$V_{pores}$	Volume occupied by the pores within a particle
$V_S$	Volume of stationary phase
$V_{SPV}$	Volume of particle that is empty or occupied by pores
$\beta$	Phase ratio
$\gamma$	Tortuosity factor
$\Delta m$	Average mass difference
$\Delta P$	Pressure drop
$\Delta P_{optimal}$	Pressure drop for optimal reduced velocity
$\varepsilon(r)$	Local interstitial porosity at a radial position from the column wall
$\varepsilon_{bulk}$	Interstitial porosity in the bulk packing region
$\varepsilon_{interparticle}$	Interparticle porosity
$\varepsilon_{intraparticle}$	Intraparticle porosity
$\varepsilon_{rel}(r)$	Relative Local interstitial porosity at a radial position from the column wall
$\eta$	Mobile phase viscosity
$\lambda_A$	A-term packed bed structure coefficient
$\lambda_{HDC}$	Ratio of particle radius to capillary radius in hydrodynamic chromatography
$\lambda_i$	Advection structural parameter in the Giddings model
$v$	Reduced mobile phase velocity
$\rho_{silica}$	Density of the skeleton of a particle
$\rho_{liquid}$	Density of a liquid
$\sigma_L^2$	Spatial variance

$\sigma_{L,A}^2$	Contribution to multiple flow path van Deemter coefficient measured as a spatial variance
$\sigma_{L,B}^2$	Contribution to longitudinal diffusion van Deemter coefficient measured as a spatial variance
$\sigma_{L,C}^2$	Contribution to resistance to mass transfer van Deemter coefficient measured as a spatial variance
$\sigma_t^2$	Temporal variance
$\tau_{HDC}$	Hydrodynamic chromatography particle elution factor
$\omega_i$	Diffusion structural parameter in the Giddings model

## **Chapter 1. Theory and Background**

### **1.1 Overview**

One of the most important analytical techniques, high pressure liquid chromatography (HPLC) continues to grow in popularity and application [1,2]. Current developments are focused on improving the performance and speed of the method with many changes specifically made to column hardware. The column is key to any HPLC separation and is the main focus of this dissertation.

HPLC instrumentation is capable of generating operating pressures up to 6,000 psi. This pressure limits the field to short columns (typically only up to 25 cm in length) packed with 3 to 5  $\mu\text{m}$  particles. The Jorgenson group has demonstrated significant improvements in performance and speed of the analytical technique by increasing the available operating pressure. This method was termed ultrahigh pressure liquid chromatography (UHPLC) and allows for the implementation of longer columns packed with sub-2  $\mu\text{m}$  particles [3,4].

The following discussion in Chapter 1 outlines the theory of band broadening in liquid chromatography (LC) columns and is meant to provide the reader with the necessary background to understand the following chapters.

### **1.2 Chromatographic Theory**

#### **1.2.1 Chromatographic Separations**

Chromatographic separations are based on harnessing the relative differences in affinities analytes have for a stationary phase or mobile phase. This affinity is described by

the partition coefficient,  $K$  (Equation 1-1).

$$K = \frac{C_S}{C_M} \quad \text{Equation 1-1}$$

Here  $C_S$  is the concentration of the analyte in the stationary phase and  $C_M$  is the concentration in the mobile phase. A larger  $K$  means that the analyte will partition into the stationary phase for longer periods of time.

This distribution of the analyte molecule can also be described by the retention factor,  $k'$  (Equation 1-2).

$$k' = \frac{n_s}{n_M} \quad \text{Equation 1-2}$$

Here  $n_s$  is the number of moles of analyte in the stationary phase and  $n_M$  is the number of moles in the mobile phase. The phase ratio,  $\beta$ , between the volumes of phases in a column is presented in Equation 1-3.

$$\beta = \frac{V_s}{V_M} \quad \text{Equation 1-3}$$

Here,  $V_s$  and  $V_M$  are volumes of the stationary phase and mobile phase, respectively.

Combination of Equations 1-1 and 1-3 gives Equation 1-4, an expression equivalent to Equation 1-2:

$$k' = K\beta \quad \text{Equation 1-4}$$

In practice retention factor is often recorded in terms of the time an analyte spends in the stationary phase ( $t_s$ ) versus the time in mobile phase ( $t_M$ ):

$$k' = \frac{t_s}{t_M} \quad \text{Equation 1-5}$$

Allowing the analytes retention time to be  $t_R$ , or the time spent in both the stationary and mobile phase, one can rewrite the equation in its typical form of use (Equation 1-6).



$$k' = \frac{t_R - t_M}{t_M} \quad \text{Equation 1-6}$$

### 1.2.2 Separation Efficiency

The previous discussion is somewhat incomplete because it does not account for the width of the eluting band. Each analyte band migrates the length of the column and will separate based on their retention factor. However, occurring simultaneously are mechanisms that broaden each band. These band broadening processes are the summation of random events that result in a Gaussian distribution of the analyte in space and time. The distribution can be described in terms of a variance. The more analyte zones broaden, the more difficult it is to resolve any given pair.

Band broadening is characterized as a variance per distance or time and is a measure of the column's separation efficiency. The height equivalent to a theoretical plate (HETP), often abbreviated as  $H$ , is defined in Equation 1-7 [1].

$$H = \frac{\sigma_L^2}{L} \quad \text{Equation 1-7}$$

In Equation 1-7,  $\sigma_L^2$  is the spatial variance and  $L$  is the length of column travelled by the analyte band. The efficiency of a separation is often described by theoretical plate ( $N$ ) count, which can also be related to a variance in time,  $\sigma_t^2$ , and an elapsed experimental time,  $t_R$ .

$$N = \frac{L}{H} = \frac{L^2}{\sigma_L^2} = \frac{t_R^2}{\sigma_t^2} \quad \text{Equation 1-8}$$

The number of theoretical plates,  $N$ , is a dimensionless parameter and is most often calculated by retention time and temporal variance.

### 1.2.3 Van Deemter Theory

The band broadening process of a given peak is the summation of several random processes. These processes can be thought of as summed contributions to the overall peak's

variance (Equation 1-9).

$$H = \frac{\sigma_{L,A}^2 + \sigma_{L,B}^2 + \sigma_{L,C}^2 + \dots}{L} \quad \text{Equation 1-9}$$

Grouping these contributions according to their dependence on the mobile phase velocity ( $u$ ) yields the van Deemter equation (Equation 1-10). This can be rewritten so each term's dependence on linear velocity is explicit (Equation 1-11) [5].

$$H = H_A + H_B + H_C \quad \text{Equation 1-10}$$

$$H = A + \frac{B}{u} + Cu \quad \text{Equation 1-11}$$

The  $A$ ,  $B$  and  $C$  terms of the van Deemter equation are descriptors of the chromatographic band broadening process and describe the contributions from eddy dispersion, longitudinal diffusion, and resistance to mass transfer, respectively.

Often columns are compared independently of particle diameter,  $d_p$ , and diffusion coefficients,  $D_M$ . In order to do this reduced parameters,  $h$  and  $v$ , are used. These relationships are presented in Equations 1-12 and 1-13.

$$h \equiv \frac{H}{d_p} \quad \text{Equation 1-12}$$

$$v \equiv \frac{ud_p}{D_M} \quad \text{Equation 1-13}$$

One can substitute these equations into the van Deemter equation (Equation 1-11) to reach the reduced form:

$$h = a + \frac{b}{v} + cv \quad \text{Equation 1-14}$$

The reduced parameters  $a$ ,  $b$ , and  $c$  are dimensionless and allow for direct comparison between columns.

To implement these reduced parameters an accurate measurement of  $D_M$  is required.

Solvents are compressed under high pressure and in turn, the viscosities tend to increase and an analyte's diffusion coefficient decreases. Commonly used analytes in the Jorgenson lab have been measured to determine their pressure dependent diffusion coefficients for use in the reduced van Deemter analyses presented in this dissertation [6]

### 1.2.3.1 A-term

The multiple flow path or eddy dispersion term describes band broadening that occurs due to variation in flow paths that an analyte may travel through in a column. These paths will differ in length and linear velocity causing the spread of the analyte band. A simplified understanding of this is presented in Equation 1-15.

$$H_A = \lambda_A d_p \quad \text{Equation 1-15}$$

Here  $d_p$  is the diameter of the packing material and  $\lambda_A$  describes the homogeneity of the packed bed. This simplified equation assumes the analyte only migrates through advection and neglects diffusion. The Giddings model incorporates exchange by both flow and diffusion:

$$H_{A,Giddings} = \sum_{i=1}^5 \frac{1}{\left(\frac{1}{2\lambda_i d_p}\right) + \left(\frac{D_m}{\omega_i u} d_p^2\right)} \quad \text{Equation 1-16}$$

In Equation 1-16  $\lambda_i$  and  $\omega_i$  are parameters related to the bed structure related to advection and diffusion. Gidding's model represents five regimes for A-term broadening: transchannel, short-range interchannel, long-range interchannel, transcolumn and transparticle (Figure 1-1) [7]. Estimates for  $\lambda_i$  and  $\omega_i$  have been made through computational modeling and suggest that the modes of band broadening actually reduce to a velocity-dependent C-term [8,9]. Thus, some of the contributions to the A-term are actually being masked in the description of the C-term [10,11]. Studies that separate the velocity dependent A-term from the C-term

suggest approximately 75% of the total value of  $H$  is dependent on the A-term [12]. Thus, the importance of improving column efficiency through more homogeneous packing is paramount.

### 1.2.3.2 B-term

Broadening due to the B-term occurs because of longitudinal molecular diffusion of the analyte molecule in the column and is described by Equation 1-17.

$$H_B = \frac{2\gamma D}{u} \quad \text{Equation 1-17}$$

Here  $\gamma$  is the tortuosity factor accounts for the resistance to free diffusion,  $D$ , of the molecules by the packed bed.

### 1.2.3.3 C-term

The resistance to mass transfer or the C-term is often divided into the resistance in three regions: the mobile phase ( $C_m$ ), stationary phase ( $C_s$ ) and the stagnant mobile phase ( $C_{sm}$ ). The resistance to mass transfer in the mobile phase describes the movement of the analyte between the interstitial volume and the particle surface. The resistance to mass transfer in the stationary phase relates to the time it takes for the analyte to diffuse into and out of the phase.  $C_{sm}$  describes the resistance to mass transfer in the stagnant phase, the region of mobile phase within particles pores and can be eliminated by use of nonporous particles [1,13]. Although detailed mathematical descriptions exist for each of these terms they are outside the scope of this dissertation. However, an important relationship between the  $C_m$  and  $C_{sm}$  should be noted. That is both terms are proportional to  $d_p^2$ . Thus, a decrease in particle size will help decrease the C-term contribution to band broadening. The reader can find very detailed reviews of these terms in these citations: [1,7-9,13-15].

#### 1.2.3.4 Limitations of the van Deemter Equation

Although a good model for fitting the data in  $H$  vs.  $u$  curves many of the factors contributing to these equations are far from exact and are instead simplified models of the actual phenomena [1]. For example, a more complete model of band broadening is based on empirical measurements and computational modeling [11]. This method isolates the contributions from longitudinal diffusion, slow absorption-desorption kinetics at the stationary phase surface, and resistances to mass transfer in the mobile phases and stationary phases. Descriptions of band broadening can be highly complex and do not affect general daily practice [1,2,7,16,17]

### 1.3 Correction for Interstitial Velocities

The mobile phase velocity,  $u$ , used throughout the presentation of chromatographic theory above is the interstitial velocity,  $u_i$ . In the experiments following, the velocity is measured by the elution of a dead time marker  $u_{measured} = L/t_o$ . If a packing material is non-porous,  $u_i$  and  $u_{measured}$  are identical. However, for particles with porosity (those used throughout) an adjustment must be made (Equation 1-18) [1]. Here  $\varepsilon_T$ , presented in Equation 1-19, is the total column porosity. The total column porosity can be subdivided into two separate regions of volume in a column:  $\varepsilon_{interparticle}$  (Equation 1-20) the porosity between particles (dependent on the volume occupied by particles,  $V_{particles}$ , and the volume of the empty column,  $V_{blank}$ ), and  $\varepsilon_{intraparticle}$  (Equation 1-21) the porosity of the particles (dependent on the volume occupied by the pores,  $V_{pores}$ , within  $V_{particles}$ ).

$$u = u_i = \frac{u_{measured} \varepsilon_T}{\varepsilon_{interparticle}} \quad \text{Equation 1-18}$$

$$\varepsilon_T = \varepsilon_{interparticle} + \varepsilon_{intraparticle}(1 - \varepsilon_{interparticle}) \quad \text{Equation 1-19}$$

$$\varepsilon_{interparticle} = 1 - \frac{V_{particles}}{V_{blank}} \quad \text{Equation 1-20}$$

$$\varepsilon_{intraparticle} = \frac{V_{pores}}{V_{particles}} \quad \text{Equation 1-21}$$

In the following chapters  $u_{measured}$  is utilized for experimental results as the porosities of the column and particles are difficult to characterize for each individual column. The difficulties of these measured porosities are discussed in Chapter 4.

#### 1.4 Ultrahigh Pressure Liquid Chromatography (UHPLC)

The linear velocity of the mobile phase and the pressure drop across a column can be related by the Kozeny-Carman equation (Equation 1-22) [1].

$$u_i = \frac{1}{185} \cdot \frac{\varepsilon_{interparticle}^3}{(1 - \varepsilon_{interparticle})^2} \cdot \frac{d_p^2 \Delta P}{\eta L} \quad \text{Equation 1-22}$$

Here,  $\Delta P$  is the pressure drop and  $\eta$  is the mobile phase viscosity. From this equation, it is clear that as the particle size decreases the pressure required to maintain a linear velocity increases with the inverse of the square of the particle diameter. Setting Equation 1-13 equal to 3, the typical optimal reduced velocity for a well packed column, it becomes clear that  $u_{optimal}$  is proportional to the inverse of  $d_p$  [1]. Combination of this with Equation 1-22 the following proportionality becomes apparent:

$$\Delta P_{optimal} \propto \frac{1}{d_p^3} \quad \text{Equation 1-23}$$

Thus, implementation of smaller particles greatly increases the required pressure. For example, halving the particle diameter requires an 8-fold increase in pressure to operate at with maximum efficiency.

The flow rate ( $F$ ) through the column is described in Equation 1-24 where  $r_c$  is the radius of the column.

$$F = u_{measured} \cdot \varepsilon_T \cdot \pi \cdot r_c^2 \quad \text{Equation 1-24}$$

This equation is considered in Chapter 5 as a model of packing particle flow into a column blank.

## **1.5 Scope of the Dissertation**

The work presented in the following chapters is focused on improving column technology. Chapter 2 looks at slurry concentration as a column packing variable and studies its affect through the lens of confocal laser scanning microscopy. Chapter 3 describes the application of the insights gained in Chapter 2 to produce the highest efficiency meter long packed capillary columns to date. Chapter 4 delves into the study of the column's total liquid volume and Chapter 5 provides methods to study axial heterogeneities in capillary columns. Finally, Chapter 6 looks at methods to refine particle batches through hydrodynamic chromatography.

## 1.6 Figures

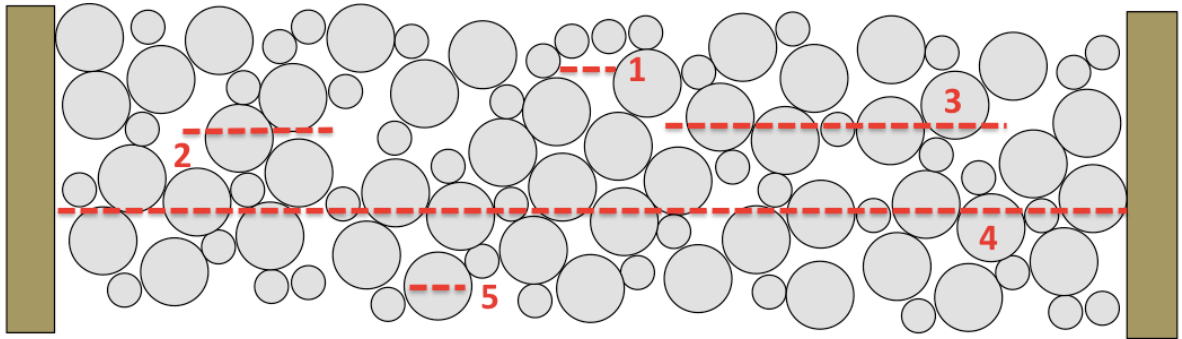


**Figure 1-1.** Representation of a packed bed presenting five regimes for A-term broadening:

1) transchannel 2) short-range interchannel 3) long-range interchannel 4) transcolumn 5)

transparticle



## 1.7 REFERENCES

- [1] U.D. Neue, Wiley-VCH, Inc.: New York, NY, 1997.
- [2] L.R. Snyder, J.J. Kirkland, J.W. Dolan, John Wiley & Sons: Hoboken, NJ, 2010.
- [3] J.E. MacNair, K.C. Lewis, J.W. Jorgenson, *Anal. Chem.* 69 (1997) 983–989.
- [4] J.E. MacNair, K.D. Patel, J.W. Jorgenson, *Anal. Chem.* 71 (1999) 700–708.
- [5] J.J. van Deemter, F.J. Zuiderweg, A. Klinkenberg, *Chem. Eng. Sci.* 5 (1956) 271–289.
- [6] T.J. Kaiser, J.W. Thompson, J.S. Mellors, J.W. Jorgenson, *Anal. Chem.* 81 (2009) 2860–2868.
- [7] J.C. Giddings, Marcel Dekker Inc.: New York, NY, 1965.
- [8] S. Khirevich, A. Höltzel, A. Seidel-Morgenstern, U. Tallarek, *Anal. Chem.* 81 (2009) 7057–7066.
- [9] A. Daneyko, S. Khirevich, A. Höltzel, A. Seidel-Morgenstern, U. Tallarek, *J. Chromatogr. A* 1218 (2011) 8231–8248.
- [10] F. Gritti, G. Guiochon, *J. Chromatogr. A* 1221 (2012) 2–40.
- [11] F. Gritti, G. Guiochon, *J. Chromatogr. A* 1302 (2013) 1–13.
- [12] F. Gritti, G. Guiochon, *Anal. Chem.* 85 (2013) 3017–3035.
- [13] N.B. Afeyan, N.F. Gordon, I. Mazsaroff, L. Varady, S.P. Fulton, Y.B. Yang, F.E. Regnier, *J. Chromatogr.* 519 (1990) 1–29.
- [14] C. F. Poole, Elsevier: Amsterdam, Netherlands, 2003.
- [15] N.B. Afeyan, S.P. Fulton, F.E. Regnier, *J. Chromatogr.* 544 (1991) 267–279.
- [16] K.M. Usher, C.R. Simmons, J.G. Dorsey, *J. Chromatogr. A* 1200 (2008) 122–128.
- [17] J.H. Knox, H.P. Scott, *J. Chromatogr.* 282 (1983) 297–313.

## Chapter 2. Investigation of Slurry Concentration's Effect on Column Performance<sup>1</sup>

### 2.1 Introduction

Recent advancements in the field of high-performance liquid chromatography have focused on size reduction of all aspects of analytical columns [1]. A decrease in particle size has pushed the field towards the implementation of ultrahigh-pressure liquid chromatography (UHPLC). Although the potential benefits of these smaller materials are numerous, difficulty in implementation continues due to the increased pressure requirements.

Assuming pressure requirements are met, perspectives have suggested that the transcolumn dispersion due to column cross-sectional heterogeneities will dominate the potential efficiency of packed beds [2]. Currently, it is accepted that a minimum reduced plate height,  $h$ , of  $\sim 2$  is representative of a homogeneous bed structure. The resulting homogeneity of a packed bed is highly dependent on the packing procedure and the product of many interdependent variables including packing pressure, slurry solvent, slurry concentration, pushing solvent, and post packing steps (for example, the application of ultrasound or solvent flushing densification steps) [3-13]. This large experimental space means that the rate-limiting step in producing new efficient columns with unique packing materials is often fleshing out the “optimal”, or at least sufficient, packing parameters.

---

<sup>1</sup> Portions of this chapter have been previously published and permission for inclusion has been granted by the publisher:

- 1) S. Bruns, E.G. Franklin, J.P. Grinias, J.M. Godinho, J.W. Jorgenson, U. Tallarek, J. Chromatogr. A. 1318 (2013) 189–197.
- 2) A.E. Reising, J.M. Godinho, K. Horman, J.W. Jorgenson, U. Tallarek, J. Chromatogr. A 1436 (2016) 118–132.

Collaboration between the Jorgenson and Tallarek groups has set out to explore this experimental space by systematic variation of packing parameters and implementation of confocal laser scanning microscopy (CLSM). Insights gained by CLSM allow us to observe and analyze the resulting bed microstructures and relate experimental packing procedures to column performance.

## **2.2 Materials and Methods**

### **2.2.1 Materials and Methods for the Preparation of UHPLC Columns and Characterization of Their Chromatographic Performance**

The materials and methods used to pack and characterize the following capillary columns are outlined in Appendix 1. Specific deviations from these methods are listed here. Kinetex particles, C18 modified 1.9  $\mu\text{m}$ , were also packed under the same procedure. The Kinetex particles were sourced from an unpacked commercially available 2.1 mm x 150 mm Kinetex column from Phenomenex (Torrance, CA). Due to the limited availability of these particles, they were packed into 50  $\mu\text{m}$  i.d. capillary.

All capillary columns used for the BEH slurry concentration studies were 75  $\mu\text{m}$  i.d. and were packed 4 cm over the final capillary length. That is 38 cm for the 1.3  $\mu\text{m}$  column study (final lengths were clipped to 34 cm) and 50 cm for the 1.9  $\mu\text{m}$  column study (final lengths were clipped to 46 cm).

### **2.2.2 Methods to Image and Analyze Packing Microstructure**

The following data sets are supported by detailed images collected via CLSM and computational analysis of the resulting renderings of the packing microstructure. Although the methods to collect and conduct these analyses are outside the scope of this dissertation, highlights of the imaging method will be presented here. Further details of these methods can be found in these citations [14,15,16].

Columns were flushed with a fluorescent dye to achieve staining of the reversed phase bonding. After staining, the excess dye was removed by flushing with an index matching liquid, in preparation for imaging. These columns were then fixed on a microscope slide and analyzed with a confocal microscope. The specifications of which have been described elsewhere [16]. The size of a slice was set to 30 nm and the step was set to 126 nm. The resulting images were then restored and used for computational reconstruction. Examples of the images resulting from this process are shown in Figure 2-1.

After computational reconstruction, a binarized image stack including a list of particles and the positioning of the column wall are used to calculate radial porosity profiles of external porosity,  $\varepsilon(r)$ , the relative porosity  $\varepsilon_{rel}(r) = \varepsilon(r) - \varepsilon_{bulk}$ . Packing voids were identified through the inscription of spheres into the reconstruction's void spaces and an example is shown in Figure 2-2.

## **2.3 Results and Discussion**

The following discussion reflects a series of experiments focused on elucidating the impact of slurry concentration on column performance. Section 2.3.2 and 2.3.3 directly followed a few preliminary results that will be outlined briefly in section 2.3.1.

### **2.3.1 Preliminary Studies on Slurry Concentration's Effect on Column Performance**

A series of columns were packed with low and high slurry concentrations. Reduced van Deemter analysis reflecting the kinetic performance of the columns were measured by the test analyte hydroquinone (HQ) and are plotted in Figure 2-3A and B for 1.9 and 1.7  $\mu\text{m}$  particles respectively. In both situations a marked improvement in performance is seen for the columns packed with higher slurry concentrations.

The reconstructions of the packed microstructures give insight into why the packed

beds formed with higher slurry concentrations are more efficient. Figure 2-4A presents the radial porosity profiles as computed from the reconstructed segments of these columns. It is immediately evident that the smaller 1.7  $\mu\text{m}$  BEH particles are more difficult to pack densely than the 1.9  $\mu\text{m}$  particles. The bulk porosity begins at  $\sim 3$  particle diameters ( $d_p$ ) from the capillary wall and is 0.44. This value is characteristic of “loose” packing. The 1.9  $\mu\text{m}$  particles approach a bulk porosity value of 0.39.

Radial particle size segregation across the bed was analyzed and presented in Figure 2-4B is the comparison of the mean relative particle size as a function of radial position in the column. This plot clearly shows that higher slurry concentrations exhibits constant mean particle size radially across the column while low slurry concentrations do not.

Analysis of these columns also looked at the number of packing voids. In these preliminary studies, voids are defined as defects that could be filled by at least 25% of the particles from the particle size distribution. In Table 2-1, it is clear that smaller particles tend to incorporate more defects in the bed structure. This is unsurprising as these beds are generally looser in the bulk region (Figure 2-4A). It is also evident that the packed beds created from higher slurry concentrations incorporate more packing voids than beds packed with lower slurry concentrations.

In summary, these preliminary results suggest that as one uses higher slurry concentrations, suppression of particle size segregation occurs. However, reduction of this packing heterogeneity is counteracted with an increase in the number of packing voids. Both kinds of heterogeneities will increase eddy dispersion and decrease performance

A logical next step was to investigate capillaries packed with core-shell material. Core-shell material has a very narrow PSD (for the Kinetex material used here a relative size

distribution (RSD) of ~6%) and would not allow for effective particle size segregation. Minimization of this packing heterogeneity should have a positive effect on separation efficiency. In this situation, because of the low RSD no significant improvement should be observed when higher slurry concentrations are used for packing.

A low slurry concentration of 3 mg/mL and a higher slurry concentration of 30 mg/mL were used for packing. Although less pronounced, an increase in performance in terms of  $h_{min}$  is seen, 2.6 to 2.4, with an increase in slurry concentration. Additionally a decrease in the slope of the reduced plate height c-term is seen (Figure 2-5).

The performances of both of these columns do not indicate a well-packed column. This is perhaps because experiments to “optimize” the appropriate slurry concentration were not conducted and the packing parameters for this very different particle structure may be distinctly different from fully porous BEH material. This poor performance is explained by the transcolumn porosity profiles of the reconstruction of these columns (Figure 2-6A). The very narrow PSD of these materials imparts a pronounced porosity oscillation in the wall region of the column and creates a very regular “crystal-like” bed microstructure, with a very low local porosity of 0.33 reached after  $\sim 4d_p$ . This is distinct from fully porous particles that show bulk behavior after  $\sim 3d_p$ . Moving further into the column, the porosity slowly increases to the bulk value. This large transition region results in an amplified wall effect and unsurprisingly poor performance. The number of packing voids within the analyzed region from this material is extremely low (Table 2-1). Here, the reconstructions of the 3 and 30 mg/mL slurry concentration columns only include 2 and 4 packing voids, respectively. Although significantly lower, it seems as though higher slurry concentrations increase the presence of voids in the packing of Kinetex material.

Figure 2-6B presents the mean relative distance between particle centers in the reconstruction plotted against the radial position in the column. These distances are smaller for the Kinetex packing than for 1.9  $\mu\text{m}$  BEH material (which is overlaid) and highlight the smaller packing distance between particles. This smaller particle distance indicates a denser packed wall region. At the wall the mean particle distance drops since only particles smaller than the mean particle diameter can approach the wall within a distance less than  $1 d_p$ . For distances greater than a particle diameter from the wall the profile remains flat for the BEH packing created with 100 mg/mL slurries and illustrates a homogeneous bed microstructure. However, the 3 mg/mL slurry of 1.9  $\mu\text{m}$  BEH material exhibits an increase in mean particle distance up to  $4.5 d_p$  from the wall. This is a result of particle size segregation. For core-shell columns the mean particle distance is constant in the region between 1 and  $4.5 d_p$  from the wall for the 30 mg/mL column and starts to increase when closer to the column's center. This is the result of a transition to the bulk properties of the bed. For the 3 mg/mL Kinetex column, the transition is also present. However, there is another region from 0 to  $2.5 d_p$  from the wall showing an increased mean particle distance. This originates from the locally increased external porosity. The analysis of the Kinetex columns suggests that the higher slurry concentration helps to compact the wall region. This is mimicked in the small but obvious difference in the porosity profiles (Figure 2-6A) and shows why slightly improved performance in terms of separation efficiency was seen.

The results of packing the Kinetex particles at two slurry concentrations, 3 and 30 mg/mL, highlight two effects of this packing variable. When using low slurry concentrations, a pronounced effect on the wall region's heterogeneity is seen, while at high slurry concentrations, a slight increase in overall packing voids is seen. Packing core-shell particles,

however, only seemed to include a few number of packing voids and higher slurry concentrations allowed for additional densification of the wall region.

The results of these studies, 1.7 and 1.9  $\mu\text{m}$  BEH as well as the 1.9  $\mu\text{m}$  Kinetex particles, led us to expect that an intermediate slurry concentration would provide the best separation efficiency. We reasoned that higher slurry concentrations seem to prevent particle size segregation and suppress wall heterogeneities but an intermediate slurry concentration should reduce incorporation of packing voids associated with very high slurry concentrations.

The following studies identify an “optimal” slurry concentration and confirm our hypothesis. The experiments and results presented here directly lead to the design of the experiment presented in Chapter 3.

### **2.3.2 Columns Packed with 1.3 $\mu\text{m}$ BEH Material**

A series of capillary columns were packed with slurry concentrations ranging from 5 to 50 mg/mL of 1.3  $\mu\text{m}$  C18 modified BEH particles. These columns were characterized with HQ as analyte in 50:50 water:MeCN + 0.1% TFA. Under these conditions HQ has a retention factor of 0.20 and reflects the kinetic column efficiency.

The minimum plate height,  $H_{min}$ , was determined from the van Deemter plots for each column and is plotted as a function of slurry concentration,  $C_{slurry}$ , in Figure 2-7. The results are very similar for a more retained analyte 4-methylcatechol (4-MC) and are overlaid in Figure 2-8. From these figures the lowest  $H_{min}$  is observed for an intermediate slurry concentration,  $C_{slurry} = 20$  mg/mL. Slurry concentrations both lower and higher produce columns with poorer efficiency. From this set of columns packed with incremental increases in slurry concentration, three columns were chosen: 10, 20 and 40 mg/mL representing a low, intermediate and high slurry concentration for CLSM analysis. The efficiency of these



columns are presented in Figure 2-7 and highlighted in red.

For these three columns full  $H-u_{av}$  plots are shown in Figure 2-9 where  $u_{av}$  is the length of the column divided by the elution time of ascorbic acid. For reference the 20 mg/mL column has a reduced plate height of 1.5 and is characteristic of a very well performing column. The other two columns have a reduced plate height of  $\sim 2.4$ . An example chromatogram for the 40 mg/mL column is presented in Figure 2-10. Here it is evident that all peaks, even for this poor performing column, are symmetrical. All columns analyzed by CLSM imaging showed PSD measurements comparable to SEM-based (Figure 2-11) and RSD's of  $\sim 15\%$ .

While packing replicate columns would likely yield slightly different plate height values, we do not believe repetition with additional columns would change the ultimate morphological structures underlying a decrease in performance as one moves away from a 20 mg/mL slurry concentration. The following discussion shows dominating morphological structures that contribute to a decrease in efficiency as the concentration is adjusted. For the work presented in this section, distinctly different features are attributed to the columns packed with 10 and 40 mg/mL slurry concentrations even though they perform similarly. Through CLSM, each column exhibits structural differences that independently explain the decrease performance when compared to the 20 mg/mL column. These conclusions only mean to elucidate morphologies dominant when one packs with a slurry concentration greater or less than the optimal.

The packing of 1.3  $\mu\text{m}$  particles in the Jorgenson lab has yielded repeatable performance when similar slurry concentrations are used. In fact, we have found slurry concentration to be one of the most dominant variables associated with ultimate column

performance. Additionally, Figure 2-7, is highly suggestive of repeatability. Here, a well-defined trend is seen as a function of slurry concentration for a series of columns packed identically except for slurry concentration. The performance markedly improves for all columns packed with slurries close to 20 mg/mL. General agreement in trend of nine packed capillaries is indicative of reproducibility.

Relative porosity differences between the bulk and wall regions were looked at as a potential contributor to performance deviations for low or high slurry concentrations. The relative porosity  $\varepsilon_{rel}(r)$  was calculated as  $\varepsilon_{rel}(r) = \varepsilon(r) - \varepsilon_{bulk}$ . The results of this calculation for each of three reconstructed packings are presented in Figure 2-12. The plots focus on the wall region, as this is the most critical region to achieve homogeneity. From previous studies we know that the wall can induce many heterogeneities. Possibilities include structural organization or specific particle arrangement and variance in mean porosity or local porosity distributions [14,15,17,18]. The results for all three columns are porosity plots that fluctuate around the bulk value and eventually reach the bulk porosity. To quantify this measurement a scalar measure, the integral porosity deviation (IPD), is used. This measure integrates the local porosity deviations with respect to  $\varepsilon_{bulk}$  over the column radius  $r_c$  (that is from  $r = 0$  at the wall to  $r = r_c$ ). This measure is expressed in Equation 2-1.

$$IPD = \int_0^{r_c} (\varepsilon(r) - \varepsilon_{bulk}) dr \quad \text{Equation 2-1}$$

The IPDs calculated from the profiles shown in Figure 2-12 are presented in Table 2-2. Since not all column images were reconstructed to the column center, the IPDs are calculated from the column wall ( $r = 0$ ) to  $r = 10.5 \mu\text{m}$  (this is a distance of  $8 d_p$  and where bulk behavior is achieved and the contribution to the IPD is zero by definition). It has been previously

shown that well performing columns should yield IPDs between 0.15 and 0.2 while poor performing columns are approximately 2.5 times as high [14].

An initial surprise was found for the 20 mg/mL column as it had not only the highest separation efficiency but also the highest IPD. A closer look at the stacked images revealed that a slight stage error (measurement error) had occurred in the z-step size, which yielded a slight offset in the radial porosity profile. Thus interpretation of the resulting IPD results will focus on the other two analyzed columns.

The main contributor to all IPD values is the first particle layer and so any minor differences between porosity profiles are often masked by this first particle. To extract the more telling data the integration limits are shifted to the first zero transition of  $\varepsilon_{rel}(r)$  which occurs at about  $1/3 d_p$  from the wall up to  $r = 10.5 \mu\text{m}$ . In this situation the column packed with the 10 mg/mL slurry shows an IPD value an order of magnitude greater than the column packed with 40 mg/mL. In a physical sense, this value represents a more loosely packed wall region for the low slurry concentration column. Chromatographically this will contribute to an increase flow velocities in this region between the wall and the bulk packing and a significant contribution to transcolumn eddy dispersion [14,17-20]. This effect is suppressed with higher slurry concentrations and is responsible for a decreased slope in the plate height curve. While the slope of the 20 mg/mL column is lower than the 10 mg/mL column (Figure 2-9) this alone can not explain the poor performance of the 40 mg/mL column which actually has nearly identical performance to the 10 mg/mL column. Therefore the features at the column wall that contribute to transcolumn eddy dispersion can not explain the differences in performance seen for each slurry concentration, so other morphological features must be examined.

As seen in previous reports (section 2.3.1) voids seem to be favored in the packed beds prepared with higher slurry concentrations. We had originally proposed that an increase in slurry concentration would eventually reach a critical point in which larger voids would begin to severely affect the column efficiency and decided to observe this in this incremental slurry concentration study.

For the results presented here significant voids are defined as a spherical void that can accommodate particles with a diameter of at least 1.08  $\mu\text{m}$ . This threshold represents 10 % of the SEM-based PSD. The results of this study are presented in Figure 2-13A (absolute number of voids) and B (cumulative number of voids). For greater detail, the voids are distinguished by size into certain bins: 10-50% of the PSD are voids sized from 1.08 to 1.31  $\mu\text{m}$ , 50-90% are voids sized 1.32-1.43  $\mu\text{m}$  and  $\geq 90\%$  are  $\geq 1.44$   $\mu\text{m}$  and are represented by vertical lines in Figure 2-13A and B.

From this data it is clear that there is an increase in the number of packing voids as higher slurry concentrations are used for packing. Moreover, larger voids are incorporated as a function of increased slurry concentration. In this case voids  $\geq 1.44$   $\mu\text{m}$  are only present in the highest slurry concentration column reconstructed. The incorporation of these voids leads to a decrease in column efficiency and they are a main contributor to the increase in  $H_{min}$ .

3D images of the 10 and 40 mg/mL beds are shown in Figure 2-14 to further highlight these differences. From these images, one can clearly see not only an increase in void number but also larger voids in the higher slurry concentration packing. An alternative view is shown in Figure 2-15 and locates a majority of these voids at the wall. Examples of some of these larger voids from the 40 mg/mL packing are shown in Figure 2-16. These voids seem to be surrounded by particles that stabilize each other's position and block access to

this empty space. This packing structure has been seen in granular packings and is well known as bridges and arches [21-27].

The existence of these voids can be directly related to increase in eddy dispersion as discussed by Giddings [28]. These voids create large interstitial flow channels and locally increased velocities that greatly affect eddy dispersion on the transchannel and short range interchannel scales.

### **2.3.3 Columns Packed with 1.9 $\mu\text{m}$ BEH Material**

In an effort to confirm these findings, a second set of columns was packed. In this experiment 1.9  $\mu\text{m}$  BEH material was packed with slurry concentrations ranging from 5 to 200 mg/mL. Again an optimal slurry concentration was found but this time a concentration of 140 mg/mL yielded repeatable results and better performing columns. This is seen in Figure 2-17A. Most interestingly this plot shows a wide range of performance for very low slurry concentrations. However, as the slurry concentration is increased (as seen with the 80 and 140 mg/mL columns) the deviation in performance begins to diminish until the “optimal” concentration is found and repeatability becomes high.

In a similar fashion, the  $H$  vs.  $u_{av}$  plots are shown for the three columns explored with CLSM Figure 2-17B. Again the performance of the extreme slurry concentrations is significantly poorer than that of the 140 mg/mL column. In this experiment almost all columns perform with a reduced plate height below two which is indicative of generally well performing columns.

For CLSM analysis the average particle size needed to be found and the results of this study are plotted in Figure 2-18. Here the probability density vs. particle diameter is plotted, confirming the sizing as 1.9  $\mu\text{m}$ . For each of the three reconstructed columns, the same

distribution in particle sizes are seen and these distributions agree with the SEM based sizing.

The aim of this experiment is to repeat the previous findings with a different particle diameter but similar particle morphology. Size segregation was looked at, as this packing heterogeneity was incorporated in the preliminary study focused on 1.9  $\mu\text{m}$  particles [15]. Plotted in Figure 2-19A is the interparticle porosity as a function of radial position into the column. Although slightly high, the same trend is seen where bulk porosity is more quickly reached when one packs with higher slurry concentrations. Interestingly, the relatively low slurry concentration of 20 mg/mL shows a pronounced dip in porosity beginning approximately 10  $\mu\text{m}$  from the wall. This dip in porosity is suggestive of a change in mean particle size within this region. On closer inspection, plotting the relative mean particle size as a function of radial position (Figure 2-19B) shows that larger particles are concentrated at the column walls, with a small region between 5 and 10  $\mu\text{m}$  that seems to focus smaller particles. This finding is particularly interesting as it is slightly different than the earlier study (there smaller particles were at the wall) [15]. Unfortunately, only speculations existed to explain the previous findings and still we must speculate as to how these particles size segregate, and in this case the opposite manner. We do know that when packing at low slurry concentrations the bed is formed predominately in the center of the column due to the lift forces associated with the flow through the empty column blank. Perhaps then the particles have an opportunity to roll to the walls after impact. This could explain the size segregation at lower slurry concentrations. The inverse behavior seen at very low slurry concentrations (section 2.3.1) may be specific to those circumstances and were not observed for this significantly higher slurry concentration of 20 mg/mL (compared to 3 mg/mL). In comparison to the 1.3  $\mu\text{m}$  BEH material, where no size segregation was found, we expect

that the relation to the optimal slurry concentration may suppress this effect. In this situation, 20 is significantly less than the 140 mg/mL “optimal” slurry concentration while for the 1.3  $\mu\text{m}$  BEH, 20 mg/mL was the optimal slurry concentration. At this point, we can only postulate on this mechanism and its occurrence.

In order to explain the poor performance of the low slurry concentration packing of 1.9  $\mu\text{m}$  BEH particles, we turned to the IPD. The results of this experiment are presented in Figure 2-20. Here the IPD values are shown for each of the radial positions from the wall to  $15 d_p$  into the bed. These values are plotted in Figure 2-21 against the radial position in  $\mu\text{m}$  for clarity and comparison. It is obvious that all three columns reach the bulk porosity after  $\sim 16 \mu\text{m}$ . However, the low slurry concentration column presents a marked decrease in porosity in the region between 8 and 16  $\mu\text{m}$  from the wall. Again, a trend is seen for columns packed with lower slurry concentrations in that they tend not to reach bulk porosity as quickly as columns packed with high slurry concentrations. The IPD value for the 20 mg/mL column in this region is an order of magnitude different than those values for columns packed with high slurry concentrations. This IPD value corresponds well with the particle size segregation data and explains the poor performance of the lower slurry concentration column. However, just as before, these observations do not explain why the very high slurry concentration does not perform as well as the intermediate slurry concentration.

To explain the poor performance of the very high slurry concentration column we turned our attention to the analysis of voids. Figure 2-22 presents the void analysis in terms of total voids per 1000 particles and the cumulative number of voids (A and B respectively). The same trend as that shown with the 1.3  $\mu\text{m}$  BEH columns is seen. The figures present a steady increase in total number of packing voids as well as an increase in the size of the

packing voids. For this particle batch bins, were again selected to represent 10, 50 and 90 % of the PSD. These bins are overlaid on Figure 2-23. Visually these voids are plotted in the 3D rendering of the analyzed beds.

The experiment set out to confirm the presence of two counteracting packing heterogeneities that were seen with 1.3  $\mu\text{m}$  BEH particles. In this situation particle size segregation was additionally seen as in the preliminary results. Although this effect manifests at low slurry concentrations the nature of this manifestation is still unknown. Again, higher porosities at the wall when packed with lower slurry concentrations and large numbers of packing voids at high slurry concentrations explain the performance as one moves away from an “optimal” balancing slurry concentration.

## **2.4 Conclusions**

The studies presented above demonstrate the existence of an optimal slurry concentration for packing within certain experimental conditions. In this case the optimization suggested the best slurry concentration is  $\sim 20$  mg/mL for  $\sim 34$  cm x 75  $\mu\text{m}$  i.d. capillary columns packed with 1.3  $\mu\text{m}$  BEH particles and  $\sim 140$  mg/mL for 46 cm x 75  $\mu\text{m}$  i.d. capillary columns packed with 1.9  $\mu\text{m}$  BEH particles. Two counteracting effects were found to explain performance as one moves from the optimum slurry concentration. At low slurry concentrations the local porosity deviation in the wall region from the bulk porosity is higher. At high slurry concentrations there is an increase in the formation of voids and of large voids. Previous studies had pointed towards particle size segregation as a potential heterogeneity at lower slurry concentrations. However, this heterogeneity was not observed with 1.3  $\mu\text{m}$  BEH materials and inverted for 1.9  $\mu\text{m}$  BEH (that is larger particles at the wall instead of small).



From these results, the logical conclusion is to pack in such a way that takes advantage of the homogeneous porosity profiles provided by the high slurry concentrations but find a way to minimize the number of voids. One possibility is sonication during the packing of very high slurry concentrations. The results of these studies are presented in Chapter 3.

## 2.5 Tables

	<u>Slurry Concentration [mg/mL]</u>	<u>No. of defects</u>	<u>Defects [nL<sup>-1</sup>]</u>
1.7 µm BEH	3	46	$1.1 \times 10^3$
	30	70	$2.2 \times 10^3$
1.9 µm BEH	3	28	$3.2 \times 10^2$
	100	37	$3.9 \times 10^2$
1.9 µm Kinetex	3	2	$4.3 \times 10^1$
	30	4	$9.3 \times 10^1$

**Table 2-1.** Results of the analyses of packing defects from the preliminary of slurry concentration studies.

	<u>10 mg/mL</u>	<u>20 mg/mL</u>	<u>40 mg/mL</u>
IPD (a)	0.148	0.193 (c)	0.156
IPD (b)	0.027	0.042 (c)	0.0017

**Table2-2.** Values of the integral porosity deviation (IPD, Equation 2-1). (a) Calculated with the integration limits of  $r = 0 \text{ }\mu\text{m}$  to  $r = 10.5 \text{ }\mu\text{m}$  (b) Calculated with the integration limits from the first zero transition ( $\sim 1/3 d_p$ ) up to  $r = 10.5 \text{ }\mu\text{m}$  (c) Biased value due to an optical artifact in the image stack.

## 2.6 Figures

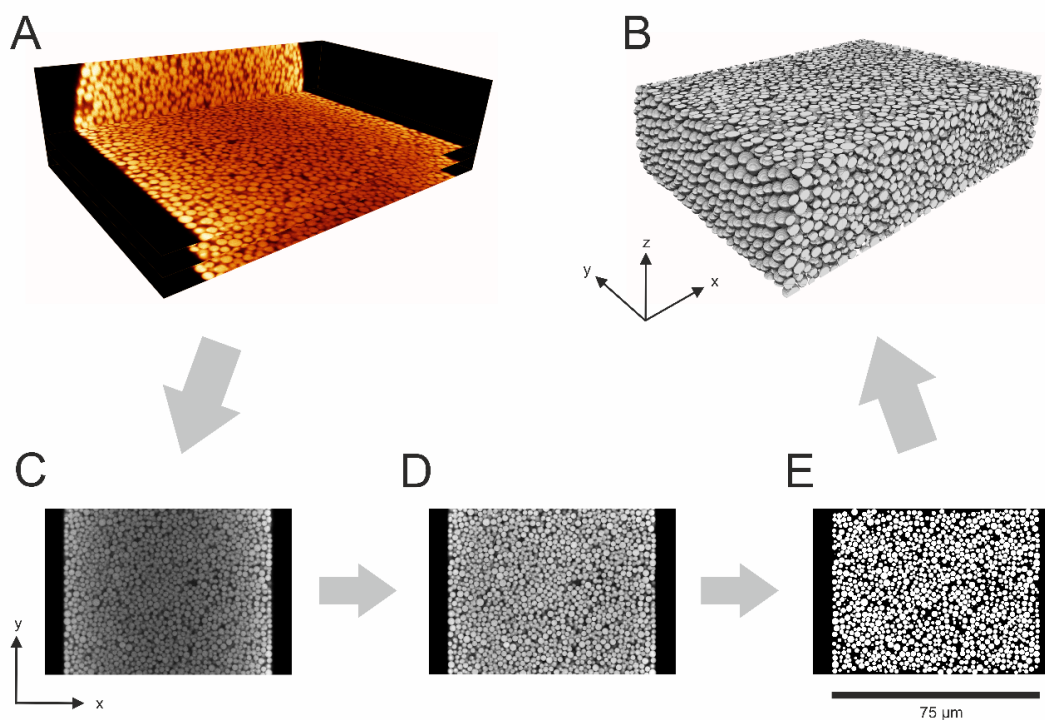


**Figure 2-1.** Representation of CLSM image acquisition and enhancement A) represents an orthoslice view of the raw CLSM images recorded from 75  $\mu\text{m}$  i.d. capillary columns. Here three slices are shown. B) Shows the final 3D rendering of the processed images. This image presents a model of the packed section of capillary bed. Figures 2-1 C, D, and E present the stepwise image results from raw data, C, to restored data, E. Figure 2-1, D shows an image within the process of enhancement and removal of noise (intensity variations, bleaching, and deconvolution to increase contrast).

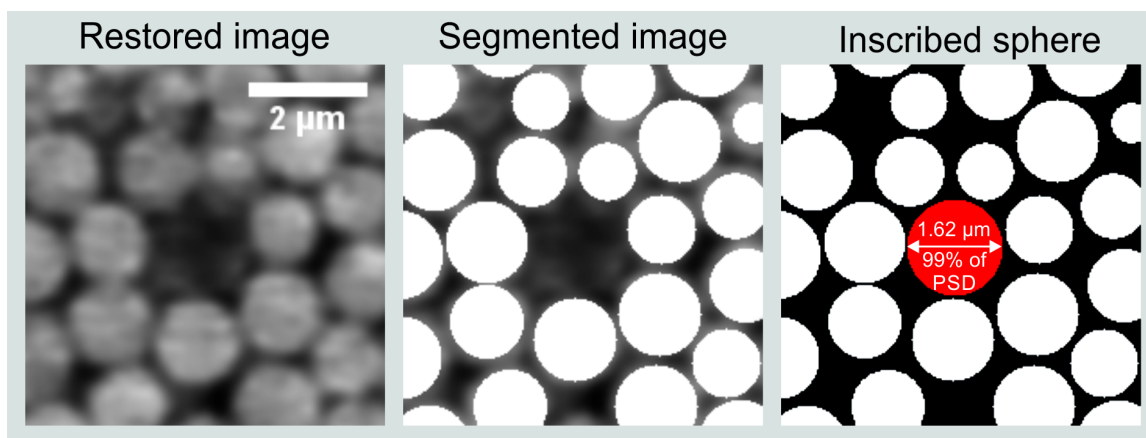


**Figure 2-2.** Example of how voids were determined. The restored image on the left panel was overlaid with the segmented image. Within this segmented image a sphere is inscribed that completely fills the void space. In this example, the column is packed with a 40 mg/mL slurry concentration of 1.3  $\mu\text{m}$  BEH particles. The inscribed sphere has a diameter of 1.62  $\mu\text{m}$  and could accommodate 99% of the 1.3  $\mu\text{m}$  BEH particle population.

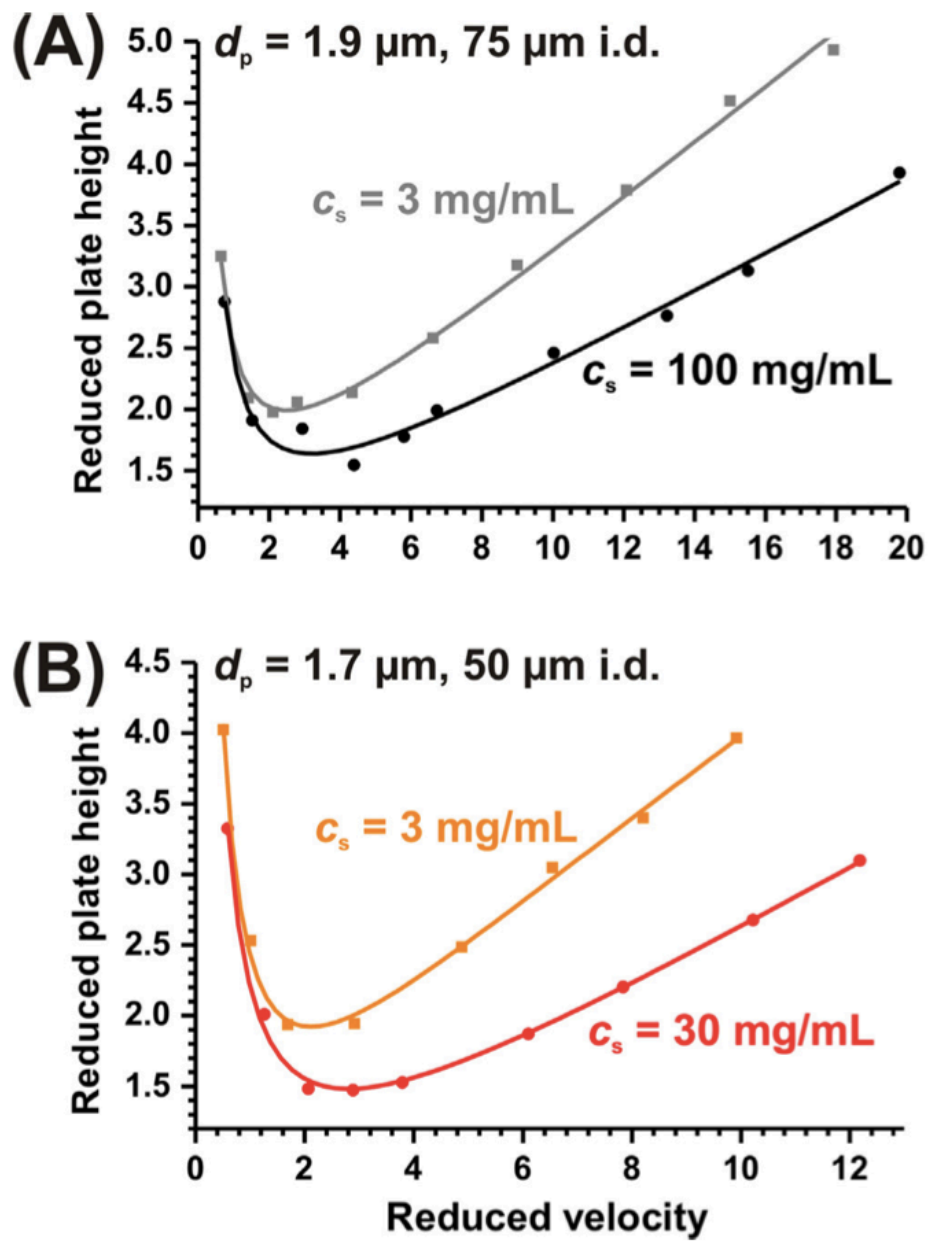


**Figure 2-3.** Reduced plate height curves for HQ for beds packed with low and high slurry concentrations of 1.9  $\mu\text{m}$  and 1.7  $\mu\text{m}$  BEH material.

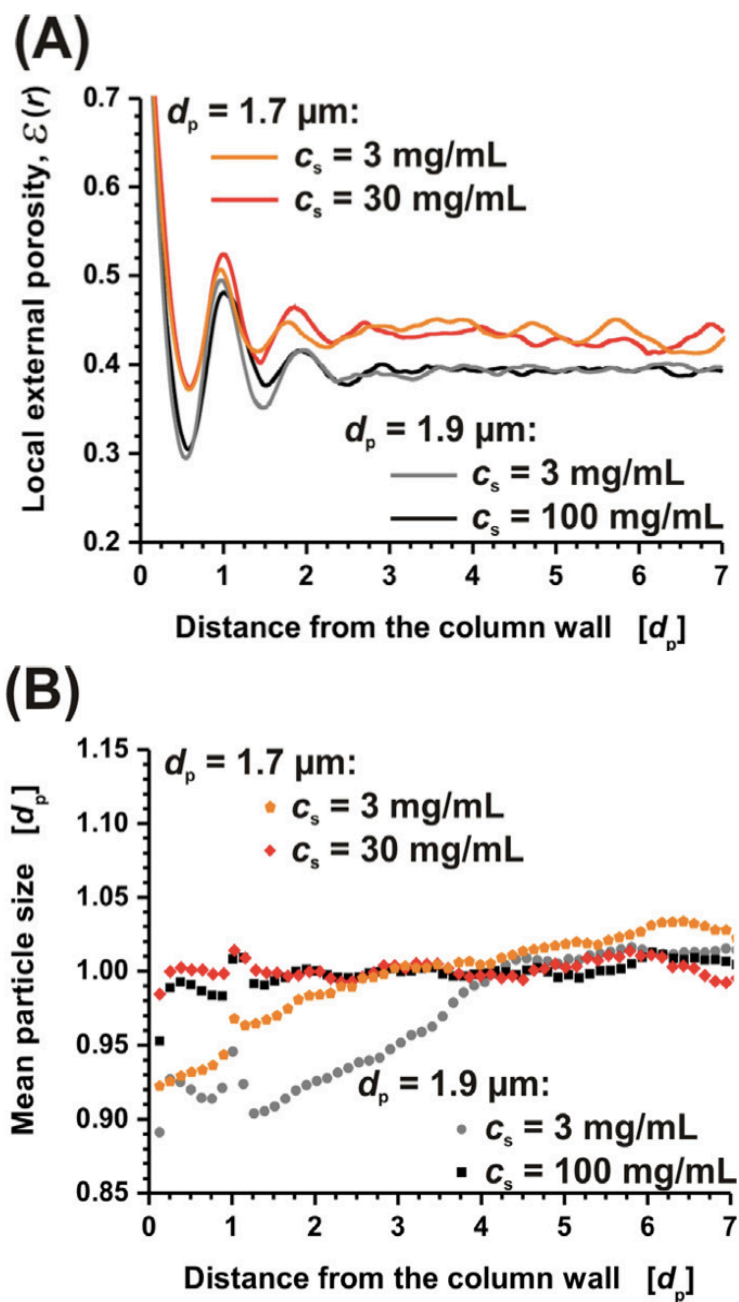


**Figure 2-4.** Plots for columns packed with 1.9 and 1.7  $\mu\text{m}$  BEH materials A) Radial porosity profiles in the wall region for the reconstructed sections of the capillary columns. B) Relative mean particle size as a function of position from the wall.

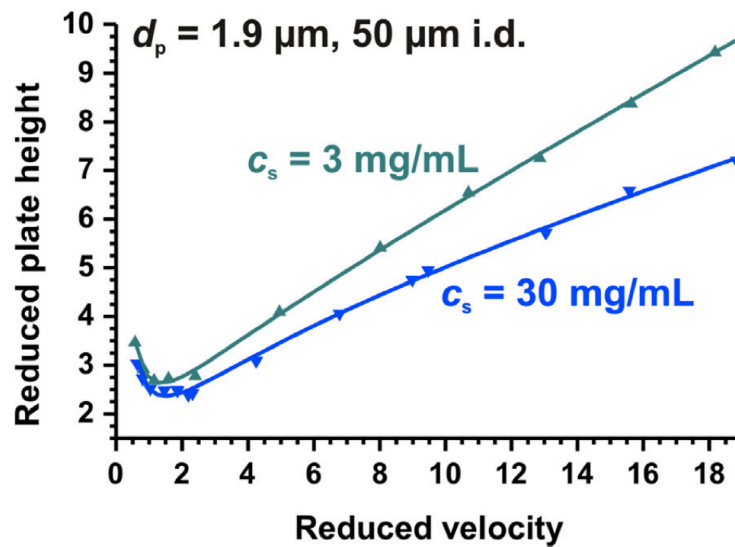


**Figure 2-5.** Reduced plate height curves for HQ. The reduced van Deemters are for columns packed with low and high slurry concentrations of 1.9  $\mu\text{m}$  Kinetex material.



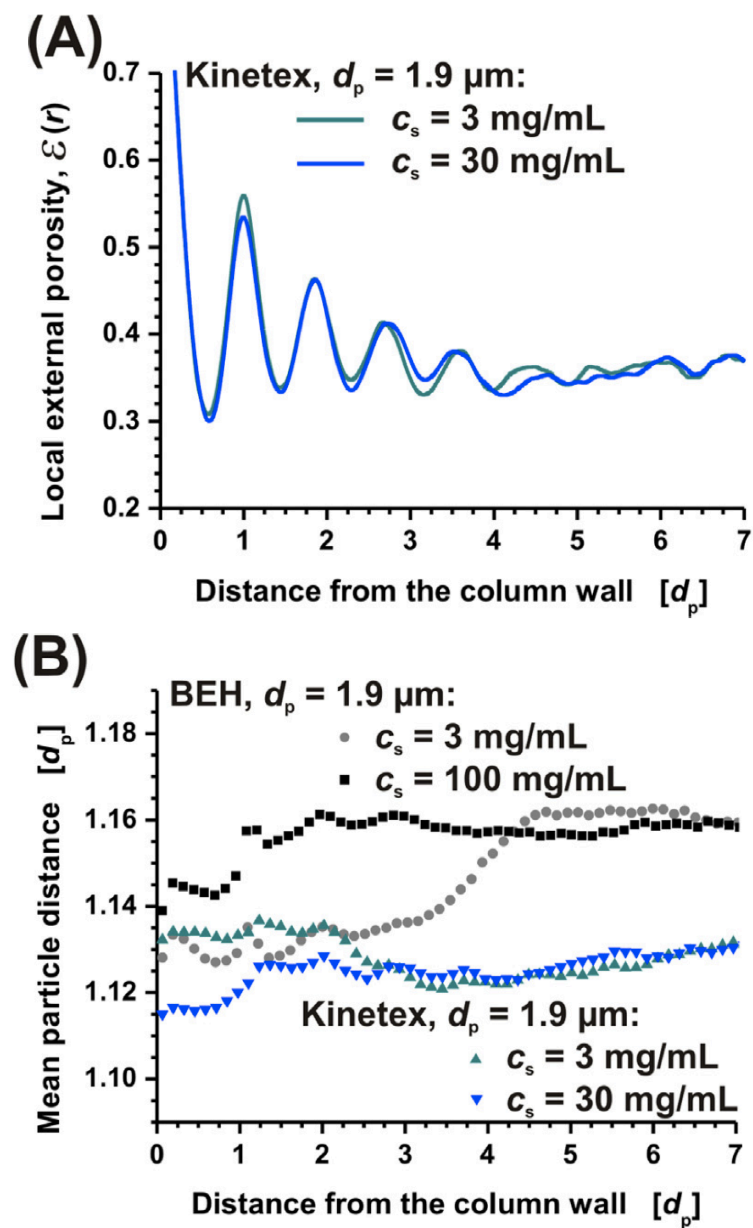


**Figure 2-6.** Plots for columns packed with 1.9  $\mu\text{m}$  Kinetex A) Radial porosity profiles in the wall region for the reconstructed sections of the capillary columns. B) Relative mean particle distance as a function of position from the wall with the results of the 1.9  $\mu\text{m}$  BEH columns overlaid.

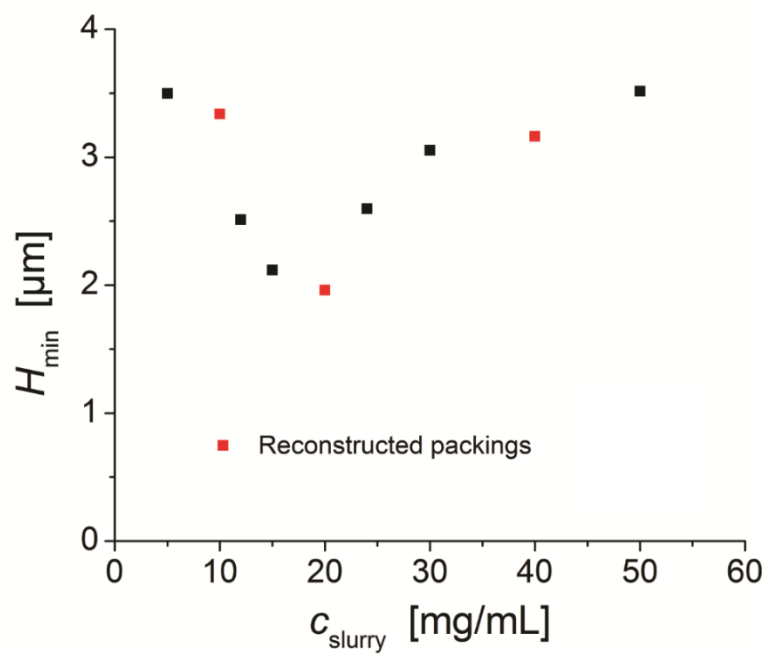


**Figure 2-7.** Minimum plate heights,  $H_{\text{min}}$ , for the entire set of columns (34 cm x 75 μm i.d.) packed with 1.3 μm BEH particles using HQ as the test analyte. The points in red represent the columns reconstructed with CLSM.

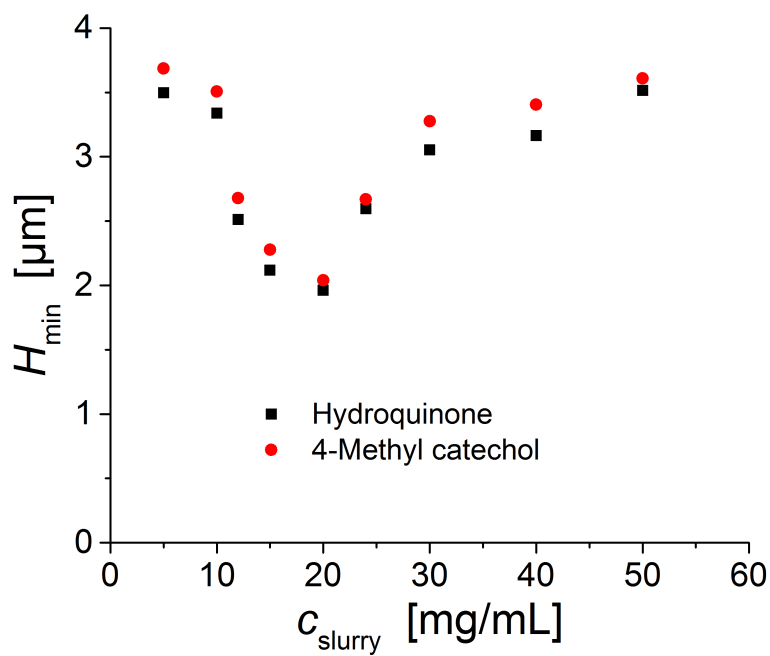


**Figure 2-8.** Minimum plate heights,  $H_{min}$ , for the entire set of columns packed with 1.3  $\mu\text{m}$  BEH particles. The results for the test analyte HQ are plotted in black and the more retained analyte 4-MC ( $k' = 0.6$ ) are plotted in black.

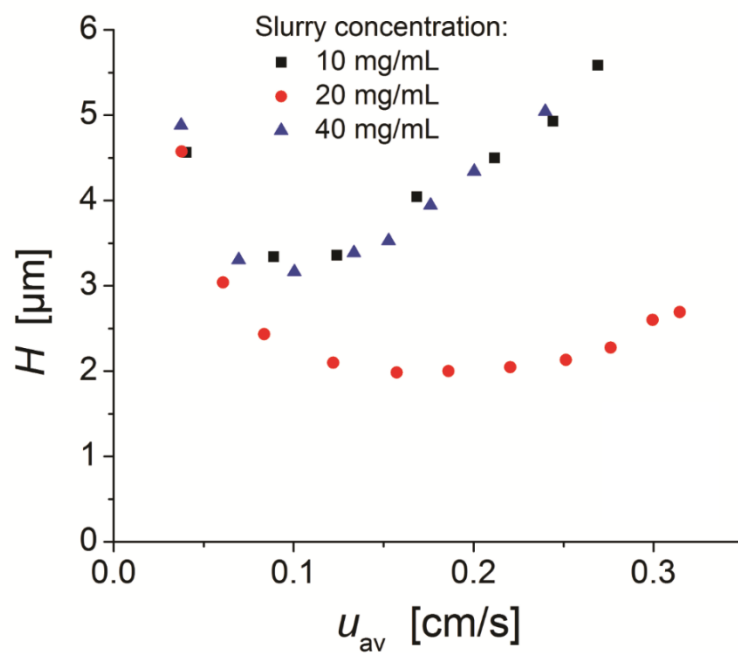


**Figure 2-9.** Plate height curves,  $H$ , vs. the average velocity,  $u_{av}$ , for the three reconstructed columns packed 1.3  $\mu\text{m}$  BEH particles. The curves are the results for HQ.

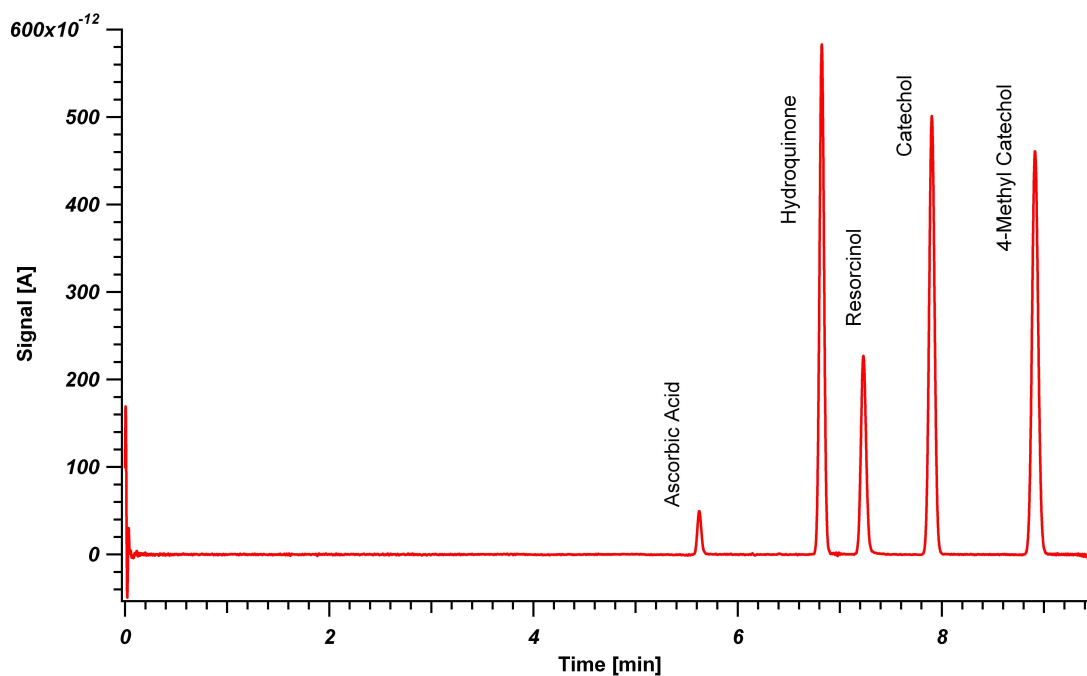


**Figure 2-10.** Example chromatogram for the column packed with a 40 mg/mL slurry of 1.3  $\mu\text{m}$  BEH.

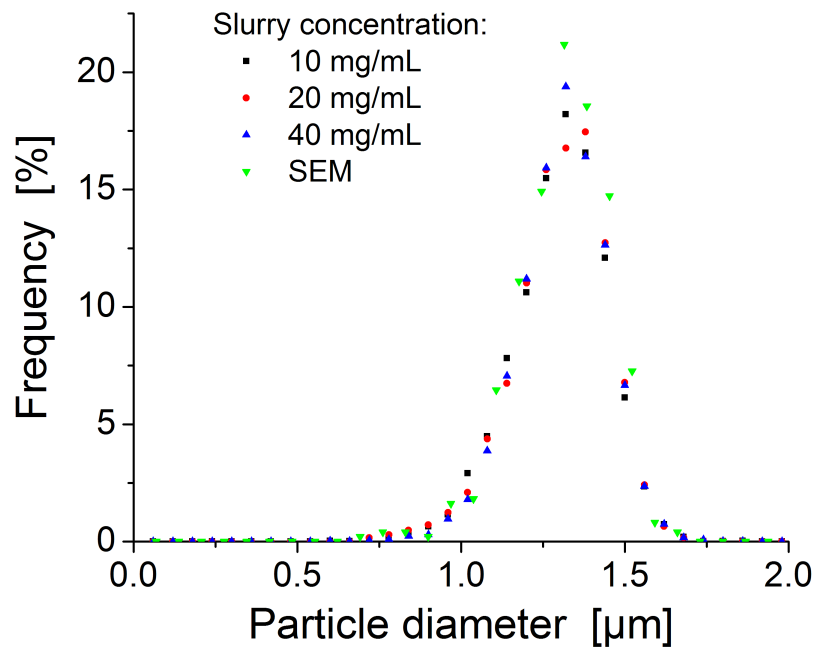


**Figure 2-11.** Particle size distribution (PSD) analysis for the 1.3 μm BEH particles. CLSM imaging based sizing is plotted in comparison to SEM based measurements.

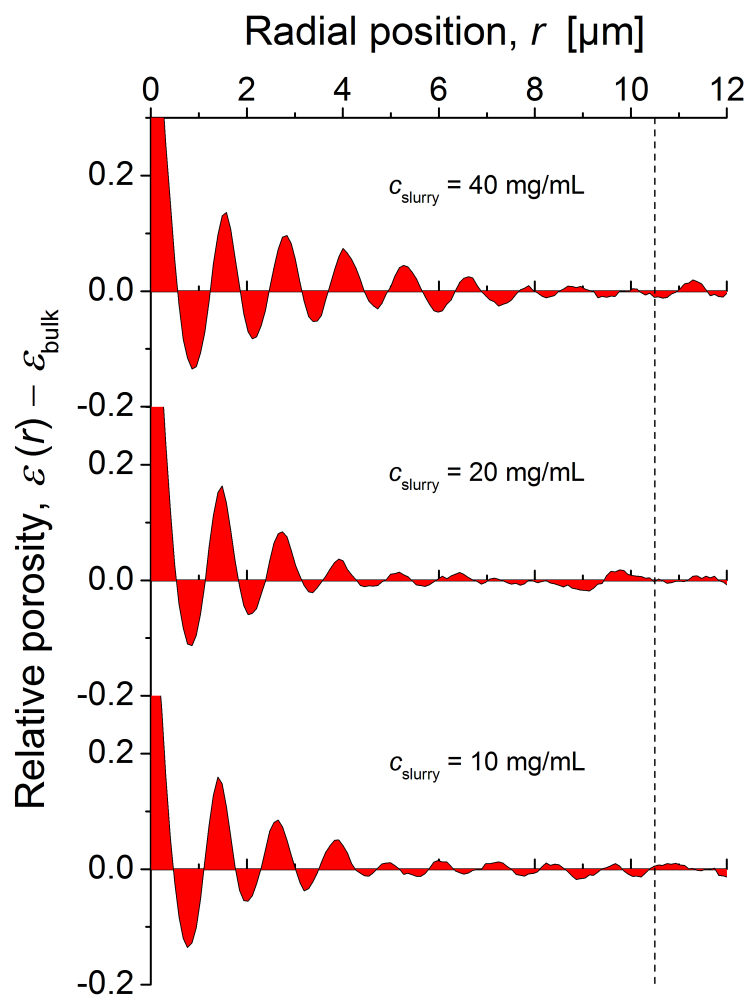


**Figure 2-12.** Radial distribution of relative porosity used to calculate the integral porosity deviation (IPDs) for the three analyzed  $1.3 \mu\text{m}$  BEH columns. The dashed line represents the limit of integration,  $10.5 \mu\text{m}$ .

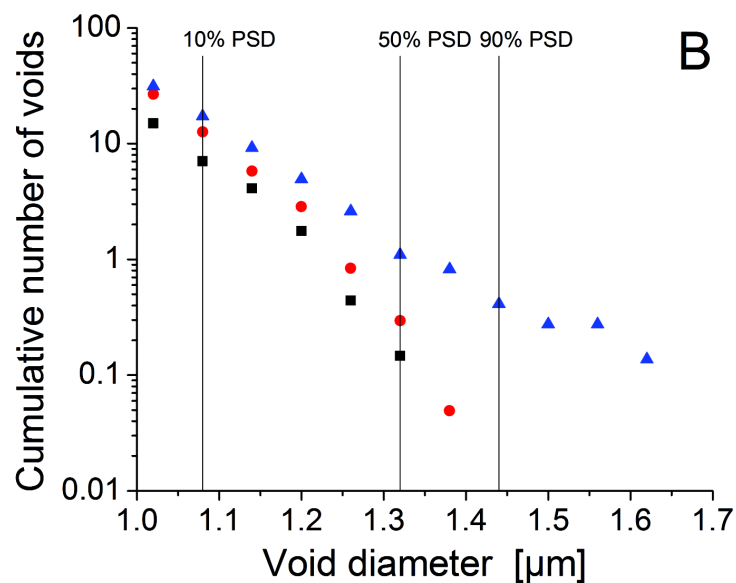
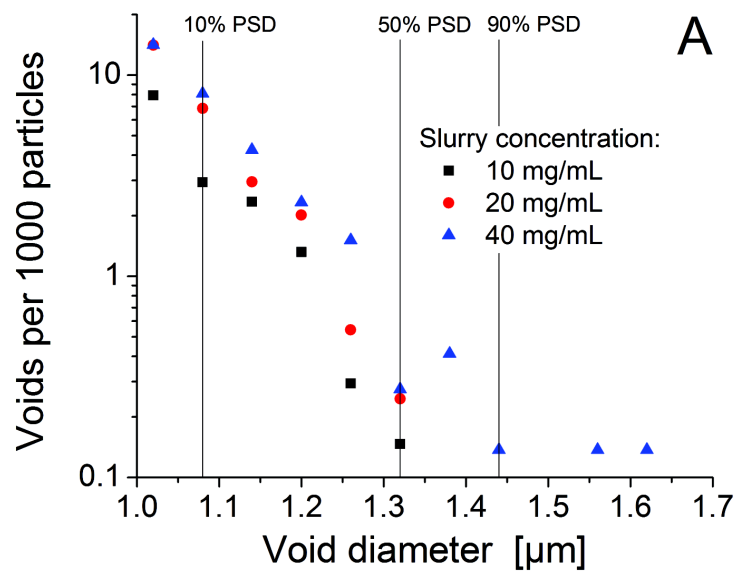


**Figure 2-13.** Number of voids for the three reconstructed 1.3  $\mu\text{m}$  BEH column bed sections per 1000 packed particles (A) Absolute and (B) Cumulative number of voids depending on their diameter.



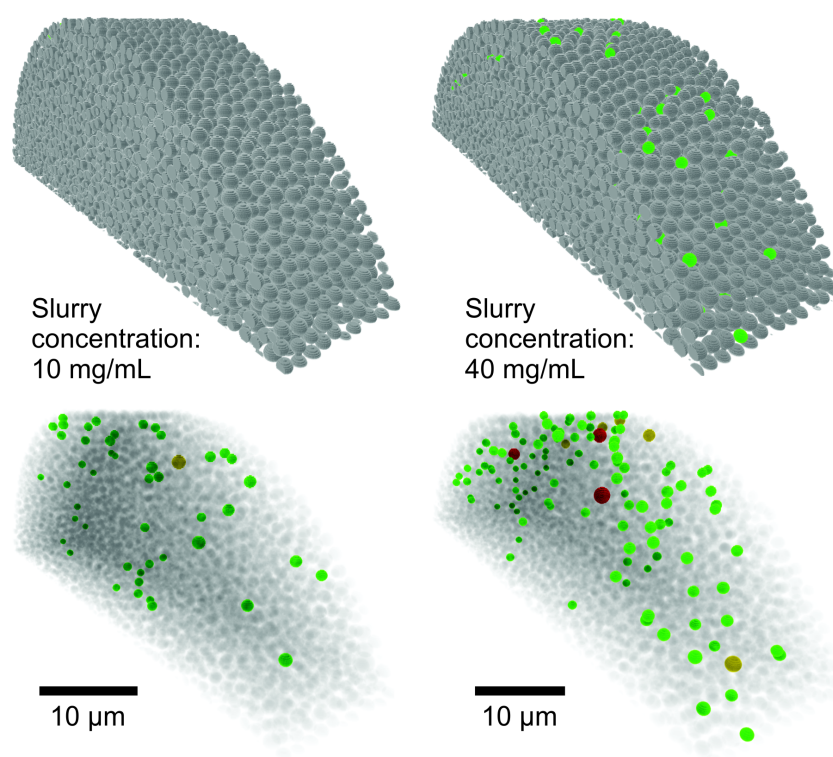


**Figure 2-14.** 3D visualization of larger voids in the CLSM-based reconstructions of the 1.3  $\mu$ m BEH columns. Green spheres represent voids that can accommodate 10-50% of the SEM based PSD, Yellow 50-90%, and red  $\geq 90\%$  of the PSD. The top panel shows the structures with optically opaque particles while the bottom panel presents transparent particles to highlight the larger voids in the packing.

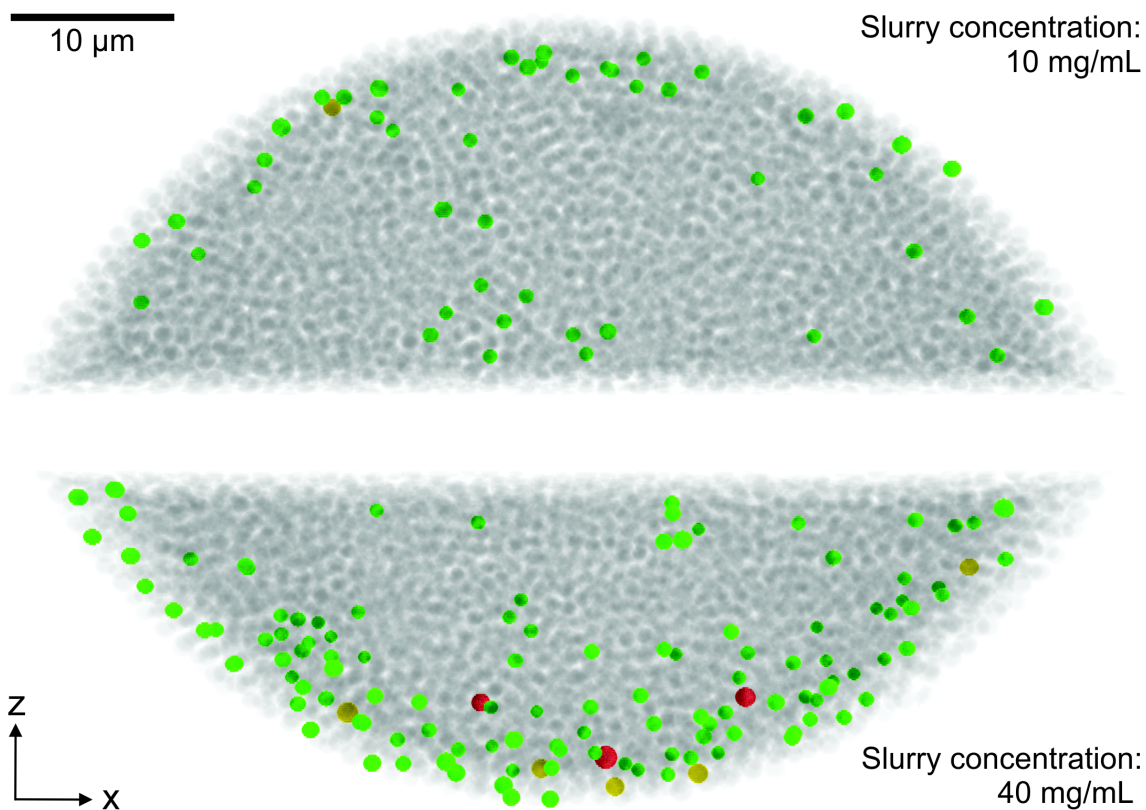


**Figure 2-15.** XZ-views of the reconstructions of the 10 and 40 mg/mL 1.3  $\mu\text{m}$  BEH columns including the larger voids in the CLSM-based reconstructions. Green spheres represent voids that can accommodate 10-50% of the SEM based PSD, yellow 50-90%, and red  $\geq 90\%$  of the PSD.

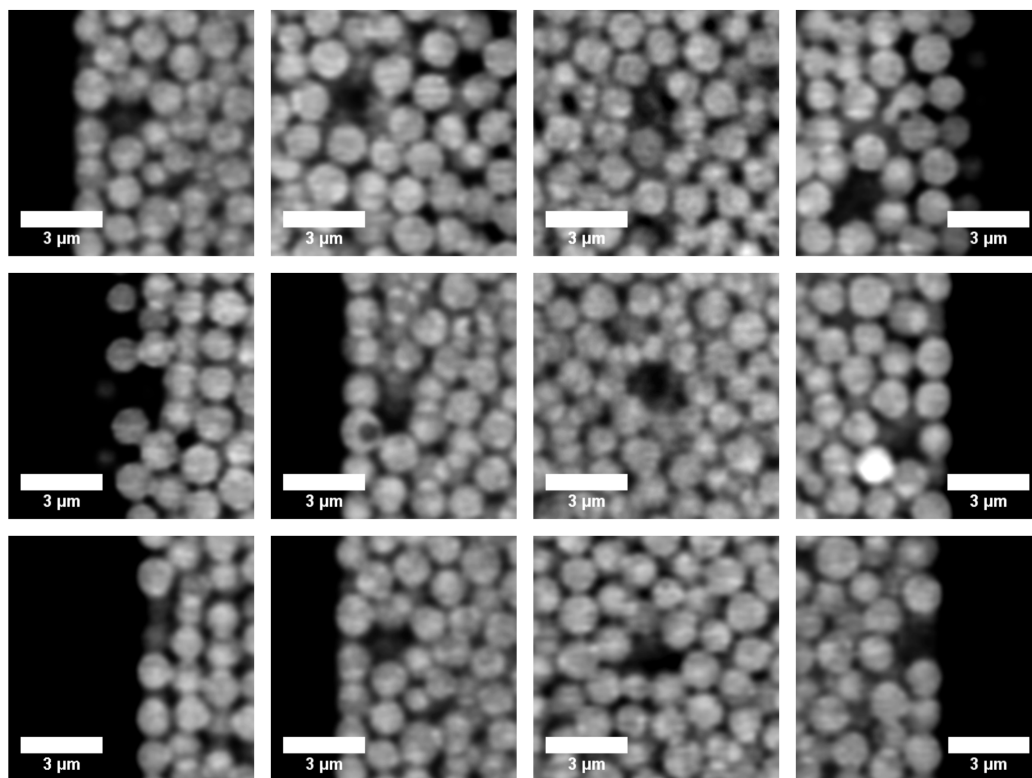


**Figure 2-16.** Examples of large voids identified during the bed reconstruction of the 1.3  $\mu\text{m}$  BEH column packed with a slurry concentration of 40 mg/mL.

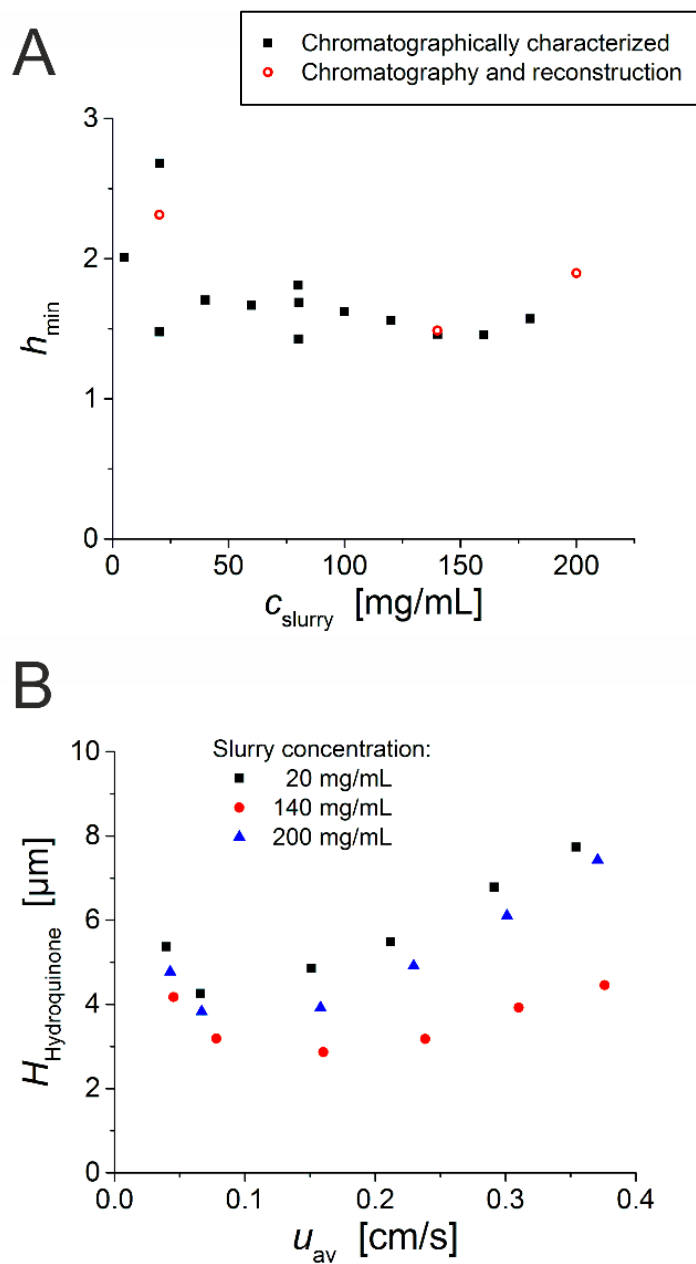


**Figure 2-17.** A) Minimum reduced plate heights,  $h_{min}$ , for the entire set of columns packed with 1.9  $\mu$ m BEH particles using HQ as the test analyte. The points in red represent the columns reconstructed with CLSM. B) Plate height curves,  $H_{min}$ , vs. the average velocity,  $u_{av}$ , for the three reconstructed columns packed with 1.9  $\mu$ m BEH particles. The curves are the results for HQ.

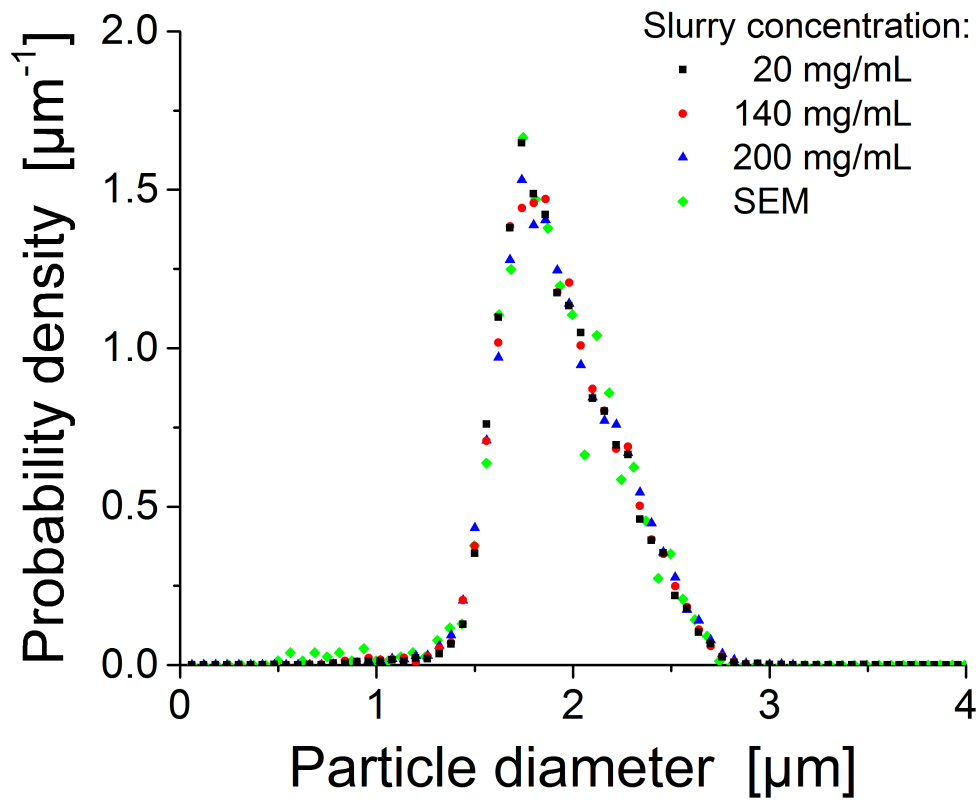


**Figure 2-18.** Particle size distribution (PSD) analysis for the 1.9 μm BEH particles. CLSM imaging based sizing is plotted in comparison to SEM based measurements.

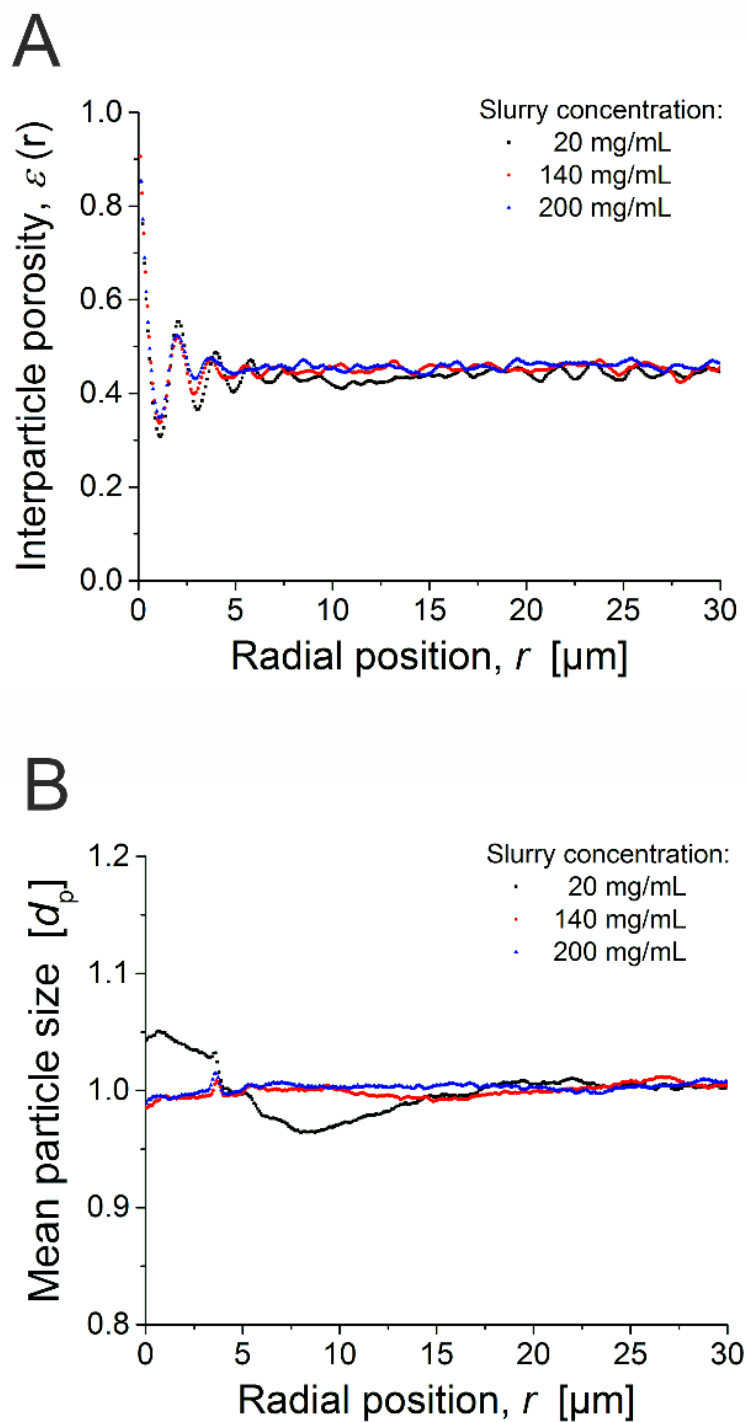


**Figure 2-19.** A) Radial porosity profiles for the analyzed 1.9  $\mu\text{m}$  BEH columns B) Plot of the mean relative particle size as a function of radial position.

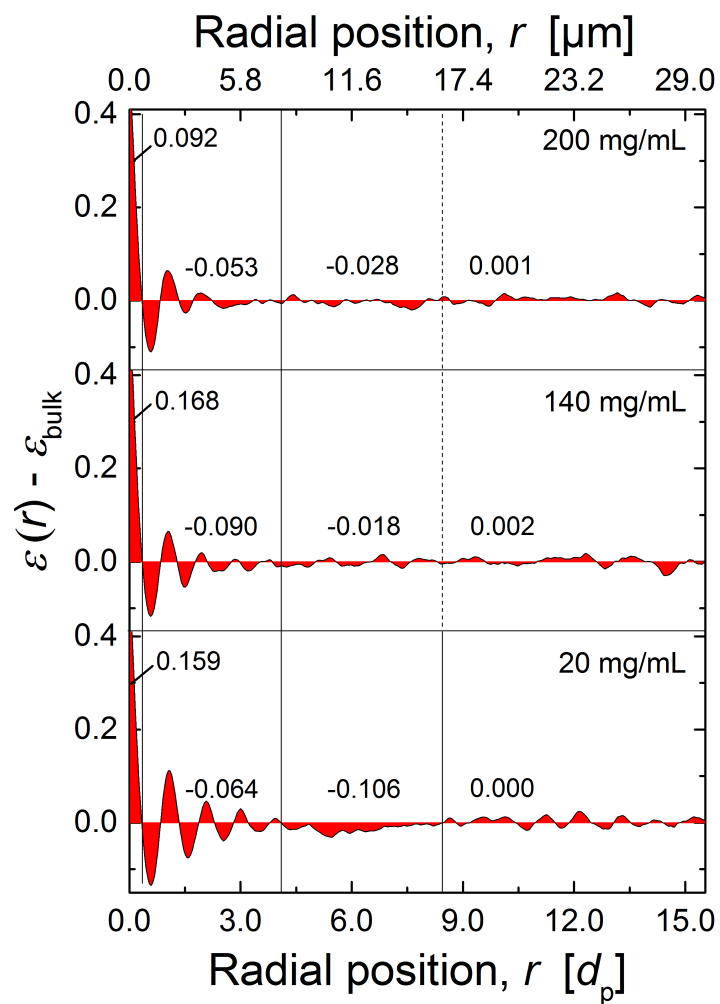


**Figure 2-20.** Radial distribution of relative porosity used to calculate the integral porosity deviation (IPDs) for the three analyzed 1.9  $\mu\text{m}$  BEH columns.

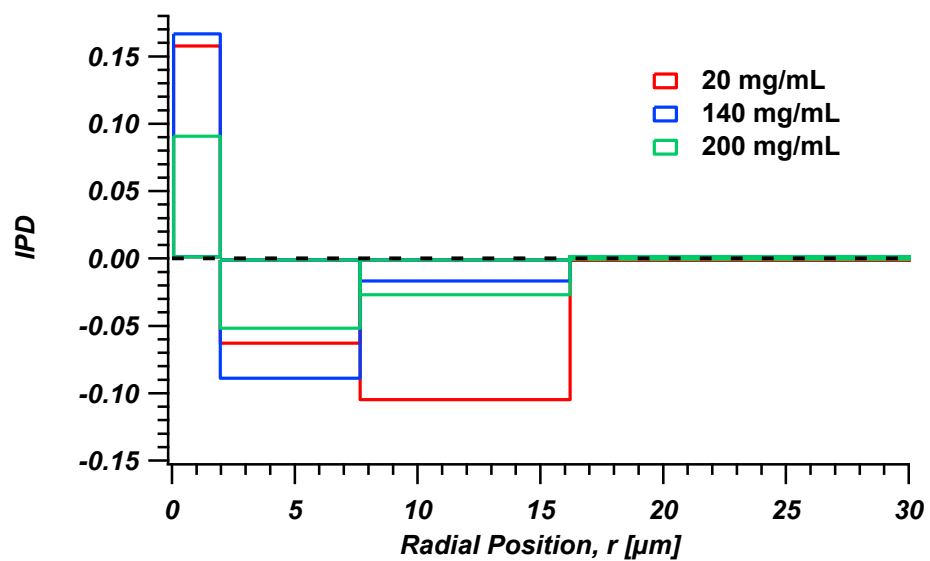


**Figure 2-21.** Plot of the IPD values extracted from Figure 2-20 as a function of distance from the column wall of the three 1.9  $\mu\text{m}$  BEH columns.



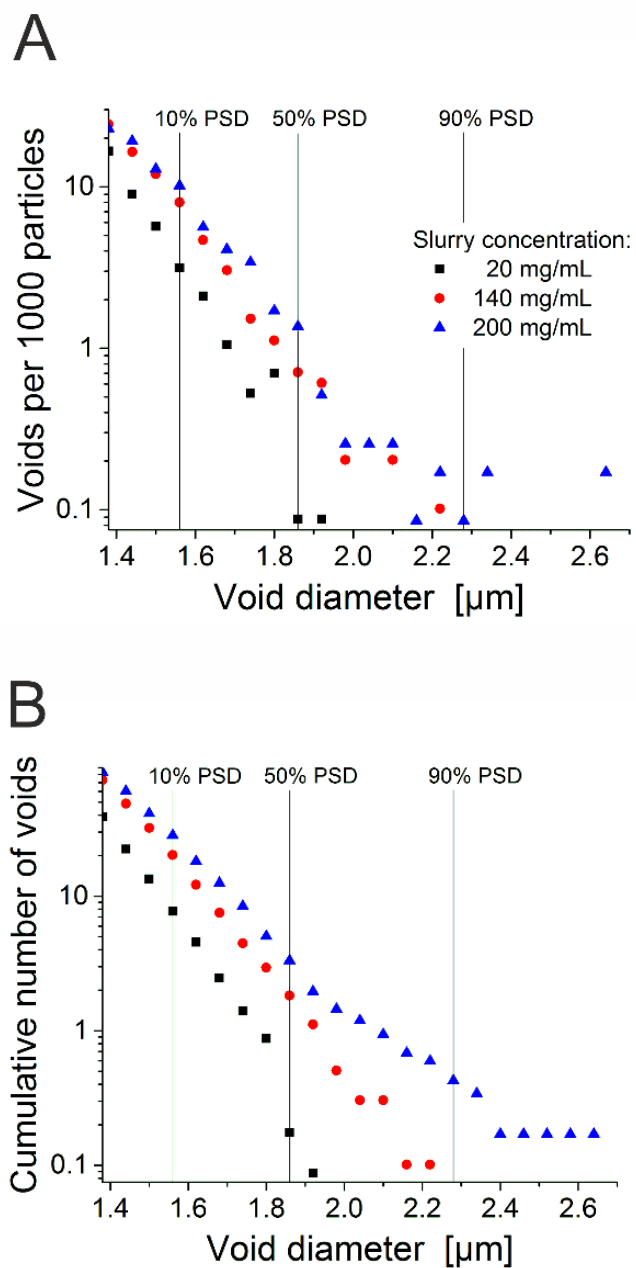


**Figure 2-22.** Number of voids for the three reconstructed  $1.9\ \mu\text{m}$  BEH column bed sections per 1000 packed particles (A) Absolute and (B) Cumulative number of voids depending on their diameter.

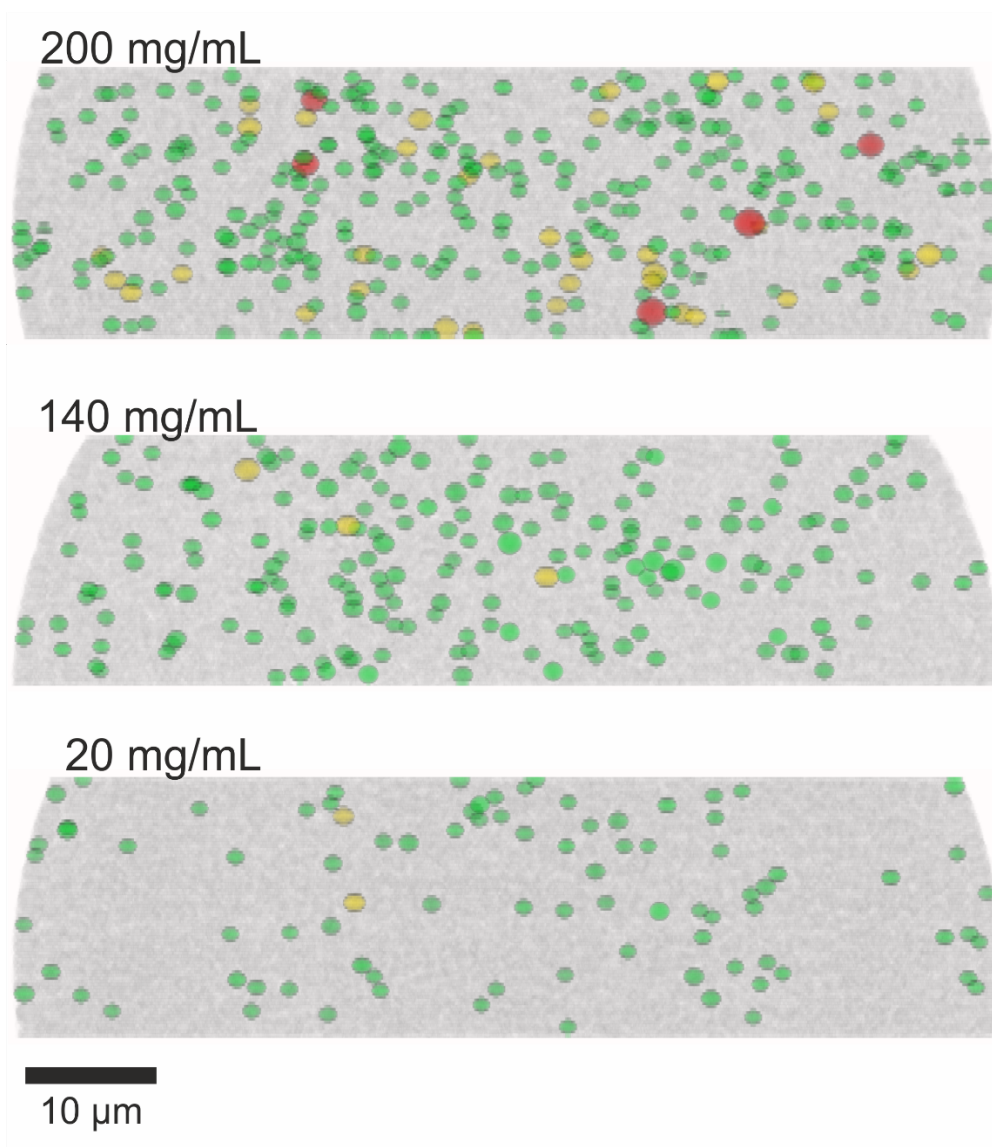


**Figure 2-23.** Visualization of larger voids in the CLSM-based reconstructions of the three 1.9 μm BEH columns. Green spheres represent voids that can accommodate 10-50% of the SEM based PSD, Yellow 50-90%, and red  $\geq 90\%$  of the PSD.

## 2.7 REFERENCES

- [1] J.W. Jorgenson, *Annu. Rev. Anal. Chem.* 3 (2010) 129–150.
- [2] F. Gritti, G. Guiochon, *Anal. Chem.* 85 (2013) 3017–3035.
- [3] J.P.C. Vissers, H.A. Claessens, J. Laven, C.A. Cramers, *Anal. Chem.* 67 (1995) 2103–2109.
- [4] J.P.C. Vissers, M.A. Hoebe, J. Laven, H.A. Claessens, C.A. Cramers, *J. Chromatogr. A* 883 (2000) 11–25.
- [5] P.D.A. Angus, C.W. Demarest, T. Catalano, J.F. Stobaugh, *J. Chromatogr. A* 887 (2000) 347–365.
- [6] J.J. Kirkland, J.J. DeStefano, *J. Chromatogr. A* 1126 (2006) 50–57.
- [7] L.E. Blue, J.W. Jorgenson, *J. Chromatogr. A* 1380 (2015) 71–80.
- [8] J.W. Treadway, K.D. Wyndham, J.W. Jorgenson, *J. Chromatogr. A* 1422 (2015) 345–349.
- [9] E.G. Franklin, Ph.D. Dissertation, The University of North Carolina at Chapel Hill, 2012.
- [10] S. Hsieh, J.W. Jorgenson, *Anal. Chem.* 68 (1996) 1212–1217.
- [11] J.S. Mellors, J.W. Jorgenson, *Anal. Chem.* 76 (2004) 5441–5450.
- [12] K.D. Patel, A.D. Jerkovich, J.C. Link, J.W. Jorgenson, *Anal. Chem.* 76 (2004) 5777–5786.
- [13] R.T. Kennedy, J.W. Jorgenson, *Anal. Chem.* 61 (1989) 1128–1135.
- [14] S. Bruns, J.P. Grinias, L.E. Blue, J.W. Jorgenson, U. Tallarek, *Anal. Chem.* 84 (2012) 4496–4503.
- [15] S. Bruns, E.G. Franklin, J.P. Grinias, J.M. Godinho, J.W. Jorgenson, U. Tallarek, *J. Chromatogr. A* 1318 (2013) 189–197.
- [16] S. Bruns, U. Tallarek, *J. Chromatogr. A* 1218 (2011) 1849–1860.
- [17] S. Khirevich, A. Hölzel, A. Seidel-Morgenstern, U. Tallarek, *J. Chromatogr. A* 1262 (2012) 77–91.
- [18] S. Bruns, D. Stoeckel, B.M. Smarsly, U. Tallarek, *J. Chromatogr. A* 1268 (2012) 53–

63.

- [19] S. Khirevich, A. Höltzel, D. Hlushkou, U. Tallarek, *Anal. Chem.* 79 (2007) 9340–9349.
- [20] A. Daneyko, S. Khirevich, A. Höltzel, A. Seidel-Morgenstern, U. Tallarek, *J. Chromatogr. A* 1218 (2011) 8231–8248.
- [21] L.A. Pugnaloni, G.C. Barker, *Physica A* 337 (2004) 428–442.
- [22] R. Arévalo, D. Maza, L.A. Pugnaloni, *Phys. Rev. E* 74 (2006) 021303.
- [23] G. Mallol, J.L. Amorós, M.J. Orts, D. Llorens, *Chem. Eng. Sci.* 63 (2008) 5447–5456.
- [24] A. Mehta, *Soft Matter* 6 (2010) 2875–2883.
- [25] A. Garcimartín, I. Zuriguel, L.A. Pugnaloni, A. Janda, *Phys. Rev. E* 82 (2010) 031306.
- [26] M.C. Jenkins, M.D. Haw, G.C. Barker, W.C.K. Poon, S.U. Egelhaaf, *Soft Matter* 7 (2011) 684–690.
- [27] C.M. Carlevaro, L.A. Pugnaloni, *Eur. Phys. J. E* 35 (2012) 44.
- [28] J.C. Giddings, Marcel Dekker Inc.: New York, NY, 1965.

## **Chapter 3. Implementation of High Slurry Concentration and Sonication to Pack High-Efficiency, Meter-Long Capillary Ultrahigh Pressure Liquid Chromatography Columns**

### **3.1. Introduction**

The benefits of sub-2  $\mu\text{m}$  chromatographic supports have largely focused separation technologies towards ultrahigh pressure liquid chromatography (UHPLC) [1]. Theoretically, sorbents on this scale provide higher separation efficiencies and shorter separation times. True benefit from these materials is dependent, however, on homogenous packing of the sorbent into a column. This is complicated by the smaller particle's requirement of significantly increased packing pressure and presents a major challenge in the creation of a uniform bed structure. As packing material continues in the direction of smaller particles, dispersion due to transcolumn heterogeneity becomes significantly more important. Transcolumn heterogeneity is estimated to account for up to 70% of the total dispersion in UHPLC columns [2].

Packing that results in a well performing column requires the formation of a homogenous bed structure across all scales, from transchannel to transcolumn, within the column [3]. Study of “optimal” packing conditions has lead to more detailed understanding of the physical process [4–14]. Unfortunately this process is dynamic and highly influenced by many interdependent parameters. The results of these studies have yielded many opinions on the “art” of column packing as opposed to the science. As discussed in detail in the previous chapter, collaboration between the Tallarek and Jorgenson groups has examined

certain packing parameters including the effects of particle properties, capillary column diameter and slurry concentration [15–17]. Most importantly, these studies have been informed by three-dimensional reconstructions via confocal laser scanning microscopy (CLSM) of the packing microstructure. These renderings have allowed for detailed expositions of morphological features corresponding to specific packing conditions, which are then related to explain the column's kinetic performance.

The results of the report on optimal slurry concentration for 1.3  $\mu\text{m}$  BEH particles [17] made suggestion at new ways to improve the overall packing quality of capillary columns and turned our focus to the implementation of very high slurry concentrations. Our previous results showed that as the slurry concentration increases, suppression of wall effects and transcolumn bed heterogeneities continues to grow. Masking this benefit at very high slurry concentrations is the inclusion of large numbers of voids in the packing. Thus, finding a way to reduce the total number of voids should allow for realization of more homogeneous and highly efficient columns.

## **3.2. Materials and Methods**

### **3.2.1. Chemicals, Materials and Methods**

Chemicals and materials and are outlined in Appendix 1. The preparation of capillary UHPLC columns has been described previously in detail [8–14]. Modifications made to this procedure are described here. Column blanks (160 cm x 75  $\mu\text{m}$  i.d.) were fritted using the Kasil method [18]. The extra 60 cm was needed to over pack slightly to allow for bed compression (~10 cm) as well as to reach from the packing vessel to the sonication bath (~50 cm). In order to prepare outlet frits, the ends of capillaries were depressed onto a glass microfiber filter (Reeve Angel, Clifton, NJ) wetted with 50/50 (v/v) potassium

silicate/formamide. The column blanks were then dried overnight at 50° C. Slurries were prepared by mixing a known mass of bridged-ethyl hybrid (BEH) particles in a known volume of acetone (to achieve 200 mg/mL) and suspended with a 10 min sonication cycle using a Cole Parmer Ultrasonic Cleaner 8891 (Vernon Hills, IL).

Prior to packing, the inlet to the column blank was fixed within a UHPLC fitting. The outlet was threaded through the top of a piece of shipping foam padding that was cut to fit snugly within the sonication bath's included basket. The portion of capillary blank to be packed (in this case ~108 cm) was pulled through the top of the foam entirely. This portion of the column blank was then coiled and taped to the bottom of the foam padding to keep it in place. To ensure the created outlet frit did not lose integrity due to sonication, it was threaded back through the shipping foam padding (from the bottom side, in which the majority of the capillary was taped) until the frit and 2 cm of outlet end of the column blank protruded from the top of the foam padding. This arrangement corresponded to the outlet of column blank being 2 cm above the water line in the sonication bath. The slurry was then placed into a packing reservoir and the inlet of the column blank was secured to the reservoir using the already affixed UHPLC fitting. The foam supporting the coiled capillary was placed into the sonication bath, ensuring that the desired final length (already coiled and secured to the bottom of the foam) remained submerged under water and that the 2 cm of the blanks outlet, including the installed frit, remained above the water line. Sonication during packing was conducted with an Elmasonic P 60 H (Elma Schmidbauer GmbH, Singen, Germany) sonication bath. The sonication bath was set to sweep mode at 80 kHz. Packing was initiated using acetone as a pushing solvent at 150 bar from a DSHF-300 Haskel pump (Burbank, CA). The packing pressure was increased to a maximum pressure of 2070 bar

when the 2 visible cm of bed had been packed. The maximum packing pressure was chosen to maintain consistency between these experiments and previously reported packing studies [15–17]. The column was allowed to pack until the formed bed was visible outside the packing foam, which meant the 108 cm of bed had been packed. The temperature of the bath was kept at 30° C by adding ice as necessary and measured using the sonication bath's temperature readout on the display. After the desired length was reached, the packing pressure was slowly released to atmospheric pressure. Columns were flushed as described in Appendix 1, and then clipped to a 100 cm bed length before an inlet frit was installed using the Kasil method.

Columns were analyzed over a range of mobile phase velocities to create plots of the plate height  $H$  vs. the average mobile phase velocity  $u_{av}$  for each analyte in the test mixture. Reduced plate height curves were created using the particles' Sauter diameter ( $d_p = 2.02$   $\mu\text{M}$ ) and  $D_M$ , the pressure-dependent diffusion coefficient of an analyte in the bulk mobile phase [20]. High frequency noise was removed from the chromatograms using a digital frequency filter and low frequency baseline drift was eliminated by background subtraction. Retention times and theoretical plate counts ( $N$ ) were determined using an iterative statistical moments algorithm written in Igor Pro 6.0 (Wavemetrics, Inc., Lake Oswego, OR) [11].

### **3.3. Results and Discussion**

Morphological heterogeneity between a column's wall region and bulk packing is often the main contributor to poor column performance [21–26]. Previous studies have indicated that the differences in these regions are dependent on slurry concentration [16, 17]. Detailed understanding of the packing microstructure, via CLSM analysis correlated to kinetic performance, has guided empirical packing studies to obtain well performing



columns. For example, our initial results suggest that there is a specific “intermediate” slurry concentration capable of balancing the antagonizing effects associated with a low or high slurry concentration for each particle diameter [16]. Further study of this proposition confirmed balancing of packing defects and demonstrated that increasing slurry concentration suppresses wall effects and reduces transcolumn bed heterogeneities through prevention of both locally high porosity and particle size segregation [17].

We further noticed that even though slurry concentrations higher than “optimal” continue to suppress wall effects, the columns perform poorly [17]. The benefits of high slurry concentrations eventually begin to diminish as the number and size of packing voids in the bed structure increases. Giddings suggested voids would impact eddy dispersion negatively and contribute significantly to chromatographic band broadening [3]. Voids increase velocity extremes and eddy dispersion on both transchannel and short-range interchannel scales. The detriment of incorporated voids was also illustrated with dispersion simulations that concluded the column’s overall performance is more dependent on reduction of large voids than obtaining high packing densities [27].

The conclusions to our most recent study propose that even higher efficiency UHPLC columns may result from formation of a homogenous bed structure across the entire column through the combination of high slurry concentration and sonication to prevent the formation of larger voids [17]. To date, sonication has been used in column packing, but only to limited effect and not in association with very high slurry concentrations [28–32].

Studied here are six capillaries packed at a very high slurry concentration. Previous studies of 100 mg/mL slurries yielded relatively well performing capillary columns with minimum reduced plate height ( $h_{min}$ ) values near 1.5 [10,16]. For this experiment a

concentration of 200 mg/mL was chosen to ensure excess to an intermediate slurry concentration, enhanced suppression of radial defects and a high number of large packing voids, wherein the cumulative effects of these voids would be expected to yield relatively poor chromatographic efficiency. Three of the capillaries within this study underwent sonication and three did not. For the sake of consistency, all six were placed in the same orientation within the sonication bath during packing, whether sonication was applied or not.

Plotted in Figure 3-1 is an example chromatogram showing the performance of one of the three columns packed with sonication. Figure 3-2 presents an enlargement of the hydroquinone peak, overlaid with a Gaussian fit and residuals. Iterative statistical moments ( $\pm 3\sigma$ ) were used for plate counts of all reported data. These plate counts are more conservative than those calculated by full width at half height and Gaussian fit methods. For example the hydroquinone peak would have plate counts of 558,000 using full width at half height and 556,000 using a Gaussian fit. Reduced  $h$  for these plate determination methods would be 0.88. Figure 3-3 plots the reduced van Deemter fits for hydroquinone for each of the six columns and Table 3-1 presents the reduced van Deemter terms. Most notably the six columns fall into two distinct groups, those that underwent the application of sonication and those that did not. The consistency of the columns that underwent sonication is very high. The actual measured efficiency for these columns approaches a reduced plate height of 1.05. Columns that were not exposed to sonication did not exhibit reproducible reduced parameters and showed poorer performance with measured reduced plate heights between 1.8 and 2.2.

Figure 3-4 plots  $u_{av}$  vs. pressure normalized for column length. The data naturally falls into two groups separated by column packing procedure. Higher average velocities for ascorbic acid are apparent for those columns prepared with sonication. Regarding the known

effects of high slurry concentrations, and their tendency to incorporate very wide void size distributions [17], we can interpret these results as similar to a packing prepared with a highly polydisperse particle size distribution (one significantly broader and more skewed than that of the packed BEH material: the utilized BEH material exhibits approximately 15% relative size distribution for the particle size distribution). Based on Figure 3-3 we know that the columns packed with sonication have a more homogenous bed structure due to the improved efficiency. This translates into substantially narrowed distribution of sizes for local interstitial fractions with respect to the columns that did not undergo sonication. This homogenization of the bed microstructure leads to higher observed velocity and permeability for the dead time marker through the column. Simulations yielded similar results in which a reduced width and tail in the interstitial volume distribution improved hydraulic permeability [33]. Packing columns with very high slurry concentration and sonication boosts separation efficiency while improving mobile phase permeability. That is a narrower width and more uniform distribution of interparticle volumes produces more uniform and less tortuous flow paths.

The performance of columns undergoing sonication far exceeds reports of other highly efficient capillary columns [10]. However, these results are not unexpected. First, the experimental setup has been optimized to limit extra-column band broadening as injection, detection and unpacked bed (frits) produce negligible extra-column band broadening. Second, it is known that reduced plate heights can approach values below 1.5 for very low aspect ratio capillaries (column-to-particle diameter ratios  $d_c/d_p < 20$ ) [9,15]. In this case  $d_c/d_p$  is 37.1, nearly twice that value. No theoretical basis exists for this limitation on minimum plate height. Transcolumn exchange of an analyte molecule on the 75  $\mu\text{m}$

dimension of the capillary diameter is fast and any exchange between different regions of local flow velocity is quickly terminated by transverse dispersion [34]. Third, from past CLSM studies we know that the integral porosity deviation approaches zero as slurry concentration increases (indicative of wall region in a bed that attains average packing density as the bulk region of that bed) [17]. The very high slurry concentrations utilized here should further suppress localized heterogeneities. Finally, simulations of plate height in computer-generated packing have yielded reduced plate heights below unity [24].

### **3.4. Conclusions**

The results presented here highlight the beneficial effects of two packing variables: very high slurry concentration and sonication. The remarkable performance of these columns, which far exceeds previous separation efficiencies seen in our lab and elsewhere for fully porous particles packed into capillary columns, leads us to believe that we have successfully mitigated the incorporation of packing voids while suppressing radial heterogeneity previously identified at a capillary column's wall. These columns approached reduced plate heights of 1.05 and a realized (instead of extrapolated as often reported) 470,000 plates/meter. Packed capillary columns with performance approaching reduced plate heights of 1 offer new frontiers into the use of UHPLC columns. When packed to a meter long and producing 500,000 theoretical plates, the opportunity for fast separations at high pressure with very high peak capacities could greatly improve one-dimensional separations of very complex samples.

### 3.5 Tables

	<u>Column</u>	<u>a</u>	<u>b</u>	<u>c</u>	<u>Best Fit</u> <u>Calculated</u> <i><u>h<sub>min</sub></u></i>
<b>Sonicated</b>	Circle	$0.36 \pm 0.10$	$1.39 \pm 0.05$	$0.11 \pm 0.02$	1.14
<b>(Red)</b>	Square	$0.47 \pm 0.18$	$1.52 \pm 0.11$	$0.14 \pm 0.04$	1.39
	Triangle	$-0.11 \pm 0.37$	$1.88 \pm 0.30$	$0.20 \pm 0.07$	1.12
<b>Not Sonicated</b>	Circle	$-0.19 \pm 0.29$	$1.71 \pm 0.16$	$0.83 \pm 0.07$	2.19
<b>(Black)</b>	Square	$0.46 \pm 0.35$	$1.56 \pm 0.25$	$0.34 \pm 0.08$	1.92
	Triangle	$0.61 \pm 0.14$	$1.42 \pm 0.12$	$0.47 \pm 0.03$	2.24

**Table 3-1.** Reduced van Deemter terms for all six columns characterized in this study.

### 3.6 Figures

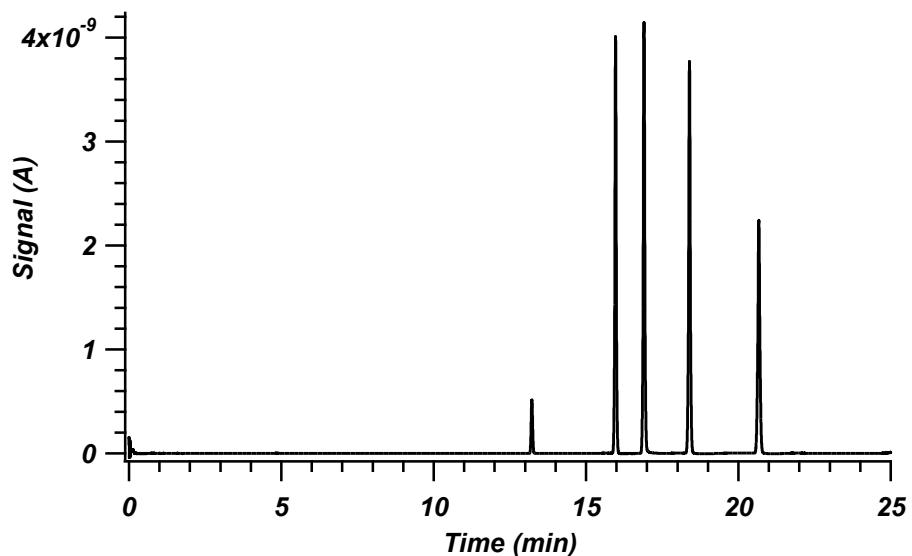


**Figure 3-1.** Example chromatogram for one of the three columns packed with sonication and run at 1630 bar. This column is represented by red triangles in Figures 3-3 and 3-4. Peaks from left to right are L-ascorbic acid, hydroquinone, resorcinol, catechol and 4-methyl catechol.

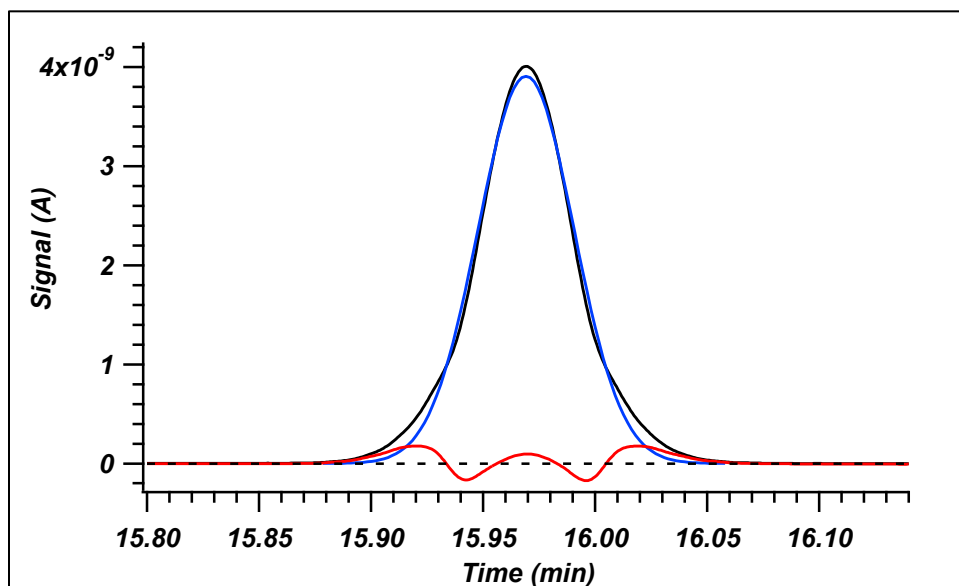


**Figure 3-2.** Example enlargement of the hydroquinone peak used for the reduced plate height curves in Figure 3-3. This peak is enlarged from Figure 3-1. The experimental data is plotted in black, the Gaussian fit in blue and the residuals are plotted in red. A black dashed line is overlaid at 0 signal for reference.

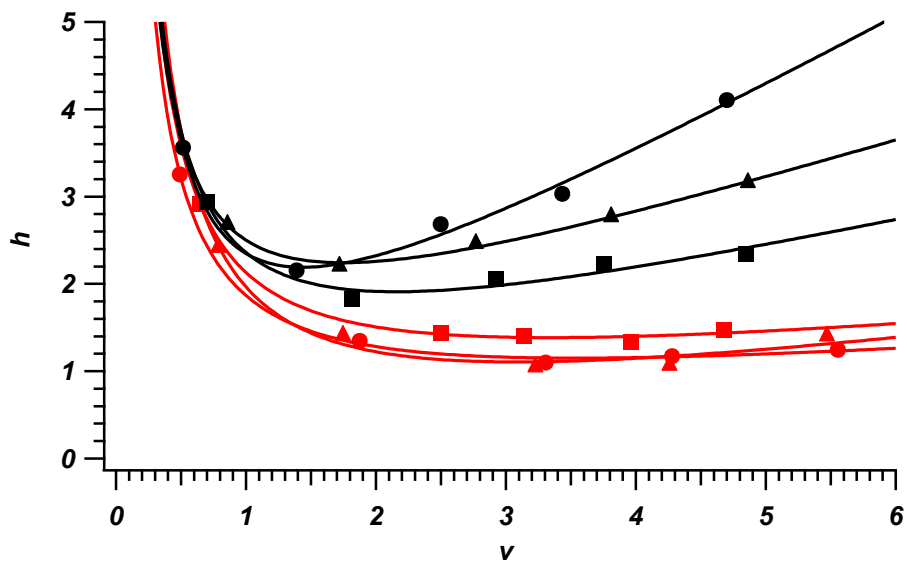


**Figure 3-3.** Plot of reduced van Deemter fits for hydroquinone on each of the 6, 1-meter long columns. Columns packed with sonication are presented in red while columns prepared without sonication are plotted in black. Marker shapes (circles, squares and triangles) distinguish each column within the parameters represented by color.



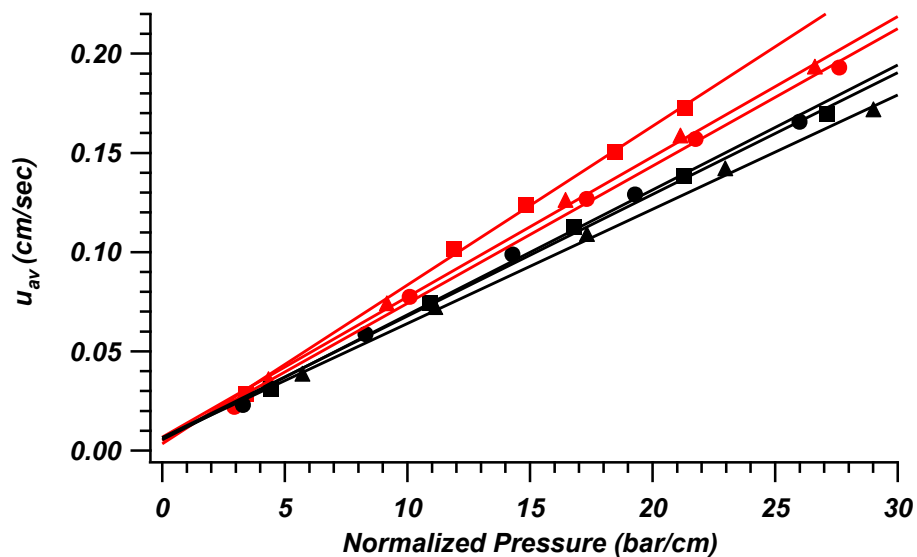


**Figure 3-4.** Plot of the linear velocity of the dead time marker, L-ascorbic acid, against pressure drop normalized for column length. Columns packed with sonication are presented in red while columns prepared without sonication are plotted in black. Marker shapes (circles, squares and triangles) distinguish each column within the parameters represented by color.

### 3.7 REFERENCES

- [1] J.W. Jorgenson, *Annu. Rev. Anal. Chem.* 3 (2010) 129–150.
- [2] F. Gritti, G. Guiochon, *Anal. Chem.* 85 (2013) 3017–3035.
- [3] J.C. Giddings, Marcel Dekker Inc.: New York, NY, 1965.
- [4] J.P.C. Vissers, H.A. Claessens, J. Laven, C.A. Cramers, *Anal. Chem.* 67 (1995) 2103–2109.
- [5] J.P.C. Vissers, M.A. Hoeben, J. Laven, H.A. Claessens, C.A. Cramers, *J. Chromatogr. A* 883 (2000) 11–25.
- [6] P.D.A. Angus, C.W. Demarest, T. Catalano, J.F. Stobaugh, *J. Chromatogr. A* 887 (2000) 347–365.
- [7] J.J. Kirkland, J.J. DeStefano, *J. Chromatogr. A* 1126 (2006) 50–57.
- [8] L.E. Blue, J.W. Jorgenson, *J. Chromatogr. A* 1380 (2015) 71–80.
- [9] J.W. Treadway, K.D. Wyndham, J.W. Jorgenson, *J. Chromatogr. A* 1422 (2015) 345–349.
- [10] E.G. Franklin, Ph.D. Dissertation, The University of North Carolina at Chapel Hill, 2012.
- [11] S. Hsieh, J.W. Jorgenson, *Anal. Chem.* 68 (1996) 1212–1217.
- [12] J.S. Mellors, J.W. Jorgenson, *Anal. Chem.* 76 (2004) 5441–5450.
- [13] K.D. Patel, A.D. Jerkovich, J.C. Link, J.W. Jorgenson, *Anal. Chem.* 76 (2004) 5777–5786.
- [14] R.T. Kennedy, J.W. Jorgenson, *Anal. Chem.* 61 (1989) 1128–1135.
- [15] S. Bruns, J.P. Grinias, L.E. Blue, J.W. Jorgenson, U. Tallarek, *Anal. Chem.* 84 (2012) 4496–4503.
- [16] S. Bruns, E.G. Franklin, J.P. Grinias, J.M. Godinho, J.W. Jorgenson, U. Tallarek, *J. Chromatogr. A* 1318 (2013) 189–197.
- [17] A.E. Reising, J.M. Godinho, K. Hormann, J.W. Jorgenson, U. Tallarek, *J. Chromatogr. A* 1436 (2016) 118–132.
- [18] A. Maiolica, D. Borsotti, J. Rappsilber, *Proteomics* 5 (2005) 3847–3850.

- [19] L.A. Knecht, E.J. Guthrie, J.W. Jorgenson, *Anal. Chem.* 56 (1984) 479–482.
- [20] T.J. Kaiser, J.W. Thompson, J.S. Mellors, J.W. Jorgenson, *Anal. Chem.* 81 (2009) 2860–2868.
- [21] F. Gritti, M. Martin, G. Guiochon, *Anal. Chem.* 81 (2009) 3365–3384.
- [22] G. Guiochon, T. Farkas, H. Guan-Sajonz, J.H. Koh, M. Sarker, B.J. Stanley, et al., *J. Chromatogr. A* 762 (1997) 83–88.
- [23] R.A. Shalliker, B.S. Broyles, G. Guiochon, *J. Chromatogr. A* 888 (2000) 1–12.
- [24] S. Khirevich, A. Höltzel, D. Hlushkou, U. Tallarek, *Anal. Chem.* 79 (2007) 9340–9349.
- [25] S. Khirevich, A. Höltzel, A. Seidel-Morgenstern, U. Tallarek, *J. Chromatogr. A* 1262 (2012) 77–91.
- [26] A. Daneyko, S. Khirevich, A. Höltzel, A. Seidel-Morgenstern, U. Tallarek, *J. Chromatogr. A* 1218 (2011) 8231–8248.
- [27] M.R. Schure, R.S. Maier, *J. Chromatogr. A* 1126 (2006) 58–69.
- [28] S. Roulin, R. Dmoch, R. Carney, K.D. Bartle, P. Myers, M.R. Euerby, C. Johnson, *J. Chromatogr. A* 887 (2000) 307–312.
- [29] P. Koivisto, R. Danielsson, K.E. Markides, *J. Microcolumn Sep.* 9 (1997) 97–103.
- [30] F. Capriotti, I. Leonardis, A. Cappiello, G. Famiglini, P. Palma, *Chromatographia* 76 (2013) 1079–1086.
- [31] S. Ehlert, K. Kraiczek, J.A. Mora, M. Dittmann, G.P. Rozing, U. Tallarek, *Anal. Chem.* 80 (2008) 5945–5950.
- [32] M.J. Wirth, S. Ranasinghe Kodithuwakkuge, C. Yerneni, R. Birdsall, WO2011127044 A2, Oct. 13, 2011.
- [33] D. Vidal, C. Ridgway, G. Pianet, J. Schoelkopf, R. Roy, F. Bertrand, *Comput. Chem. Eng.* 33 (2009) 256–266.
- [34] A. Daneyko, D. Hlushkou, S. Khirevich, U. Tallarek, *J. Chromatogr. A* 1257 (2012) 98–115.

## Chapter 4. Total Liquid Volume as a Function of Particle Size and Mobile Phase<sup>2</sup>

### 4.1 Introduction

The total liquid volume within a capillary column is often overlooked and not measured due to assumptions made for traditional dead time markers in isocratic modes or common modes of practice for gradient liquid chromatography (LC). However, this volume is a fundamental parameter to our understanding of column performance and operation. For example the calculation of a solute's retention factor,  $k'$ , relies on an accurate knowledge of the true dead time of the column.

Gradient elution under ultrahigh pressure liquid chromatography (UHPLC) conditions is another situation that benefits from accurate knowledge of a column's mobile phase volume. Most gradients are formed utilizing modest pressures in a constant flow mode. With the shift in focus towards implementation of long capillary columns (>25 cm) packed with small, sub-2  $\mu\text{m}$  sorbents, a modification of experimental design may be required. This is because gradients are currently not easily or accurately formed at ultrahigh pressures.

One route to run gradients at very high pressures is a constant pressure system. Here, a gradient is created and stored at low pressures and then played back at a very high pressure in a last in first out order. Gritti and Guichon [1] compared gradients delivered by constant pressure and constant flow and found that peak capacities were similar for both modes.

---

<sup>2</sup> Portions of this chapter have been previously published and permission for inclusion has been granted by the publisher:

1) A.E. Reising, J.M. Godinho, K. Horman, J.W. Jorgenson, U. Tallarek, J. Chromatogr. A 1436 (2016) 118–132.

Interestingly, peak capacity from the constant pressure mode showed a slight advantage, as the system always operates at the maximum pressure and flow rate, while constant flow mode is limited by the pressure associated with the maximum viscosity of the mobile phase in the column [2].

A constant pressure gradient system has been explored in our laboratory [3] and is described elsewhere. Fundamental to implementation of this methodology is the description of the gradient. Traditionally gradients are described in terms of time and thus the total liquid volume of a column is not a firm parameter needed for experimental design. For a constant pressure system, gradients are more appropriately reported in units of volume. In practice the gradient volume is directly calculated from the time it takes to load the gradient multiplied by the flow rate. The length of the gradient is programmed to produce a specific change in %B per measured column volume. Determination of the necessary gradient volume is based on the total liquid volume within the column. This highlights the importance of being able to accurately determine the total liquid volume, especially amongst different particle morphologies, and perhaps more importantly as smaller particle diameters are utilized.

#### **4.1.1 Introduction of Variables Referenced in the Following Discussion**

The volume of liquid within a column is a summation of different porous regions within a packed column blank. For clarity these regions will be described individually here.

The total spatial volume of a column blank,  $V_{blank}$ , is described in Equation 4-1 using the physical dimensions of the empty tube where *i. d.* is the internal diameter and *L* is the column length:

$$V_{blank} = \pi \left( \frac{i. d.}{2} \right)^2 \times L \quad \text{Equation 4-1}$$

The total porosity of a packed column (the total fraction not occupied by solids) that can be

filled with liquid is described by  $\varepsilon_T$ . This value can be presented as a percent liquid volume by multiplying by 100 %. This fraction is defined as the total volume of liquid in a column,  $V_L$ , divided by  $V_{blank}$ . This relationship is presented in Equation 4-2.

$$\varepsilon_T = \frac{V_L}{V_{blank}} \quad \text{Equation 4-2}$$

$\varepsilon_T$  can be subdivided into additional subcomponents. Let  $\varepsilon_{interparticle}$  (Equation 4-3) represent the fraction of volume between particles. Here  $V_{particles}$  represents the volume occupied by the physical particle and includes any of the particle's porosity.

$$\varepsilon_{interparticle} = 1 - \frac{V_{particles}}{V_{blank}} \quad \text{Equation 4-3}$$

$\varepsilon_{interparticle}$  is a measurement of average packing density of a sorbent and varies for each column. This value typically lies between the extremes of the random tight packing limit of 0.35 (estimated from computer simulations of frictionless hard spheres [4]) and the random loose packing limits suggested for frictional hard spheres [5-10]. It is most commonly assumed to be 0.4 for random packing of spheres.

Next allow  $\varepsilon_{intraparticle}$  to represent the total accessible volume within the particles (Equation 4-4). Here  $V_{pores}$  represents the volume occupied by the pores within a particle.  $\varepsilon_{intraparticle}$  is specific to a particle's morphology and for example, a nonporous packing material would exhibit an  $\varepsilon_{intraparticle}$  equal to 0. This value increases for different particle types; superficially porous and fully porous particles respectively.

$$\varepsilon_{intraparticle} = \frac{V_{pores}}{V_{particles}} \quad \text{Equation 4-4}$$

Summation of these two values,  $\varepsilon_{intraparticle}$  and  $\varepsilon_{interparticle}$ , equals  $\varepsilon_T$  (Equation

4-5).

$$\varepsilon_T = \varepsilon_{interparticle} + \varepsilon_{intraparticle} \quad \text{Equation 4-5}$$

The total porosity of the packed column, or the total fraction containing liquid ( $\varepsilon_T$ ) can be expressed as a physical volume, the total liquid volume within a packed column:  $V_o$  (Equation 4-6). Here the total volume within the empty column is multiplied by the fraction of column that could contain liquid.

$$V_o = V_{blank} \times \varepsilon_T \quad \text{Equation 4-6}$$

## 4.2 Methods for the Determination of the Total Liquid Volume in a Column

Although deceptively simple both experimentally and theoretically, an agreed upon method to measure the value of  $V_o$  has proven elusive [11]. Many methods have been developed to determine this value and no clear “best” method has been found. Methods of study include pycnometry, measurement of the elution time of unretained neutral markers, measurement of the elution time organic and inorganic salts, detection of minor baseline disturbances and the implementation of a homologous analyte series [11]. More complicated methods require modeling of results, such as inverse size exclusion chromatography, or elaborate experimental procedures to block pores [12]. Two of the more common methods will be discussed briefly here and will aid in the interpretation of the results in the following sections. Rimmer, Simmons and Dorsey presented further details in a review of these methods [11].

### 4.2.1 Unretained Neutral Marker

One of the most practical methods to determine total liquid volume in a packed column is to multiply the measured flow rate by the elution time of a neutral, unretained dead time marker. Most chromatography experiments make the assumption that typical dead time

markers such as ascorbic acid (AA), uracil or thiourea yield a total liquid volume or one where the marker completely explores the entire liquid fraction in a column. However, to be a true unretained neutral marker the species must be unable to distinguish between regions within a packed column to fully portray an exploration of all intra- and interstitial volumes. Unfortunately many “unretained” markers have slight retention and/or unfavorable interactions with enriched solvent layers at the particle surface. However, this method is fast, simple, nondestructive and likely already incorporated into most experimental designs.

To understand how a true dead time marker fully samples the entire liquid fraction, imagine a tube where two regions exist, one region that is not swept by solvent flow (a stagnant region such as the stagnant region within a pore of a chromatography bead) and a flowing mobile phase region such as the region between chromatography beads. Assuming the stagnant region is comprised of a liquid identical to that within a swept region (i.e. the partition coefficient,  $K$ , is equal to 1 for a given species between the two regions) the elution time will represent the entire liquid volume of the tube as by definition the species has equal access to both regions. This assumes that the stagnant region is identical in composition to the flowing region and the analyte cannot distinguish between the two regions. Unfortunately many unfavorable chemical interactions exist that prevent this idealized model.

#### **4.2.2 Pycnometry**

When utilizing pycnometry as a method to determine the total liquid fraction, the volume is calculated from the weight difference of the column filled with solvents of varying density. The method has the distinct advantage of representing the maximum possible void volume. This is especially true if the column is first dried entirely, massed and then compared to its mass after mobile phase equilibration. Unfortunately, it is difficult to test



repetitively and does not account for situations where wetting of the bonded phase by the solvent is an issue. Even more important practically is that capillary columns, such as those utilized in UHPLC, require the measurement of mass differences that become minimal; especially as column length and internal diameter are reduced. Another concern when drying the column is how to gently dry the bed to avoid rapid desolvation, which may affect the packing microstructures.

#### 4.2.3 Interpretation of Measurements

From these methods one can make a few inferences to the values of  $\varepsilon_{interparticle}$  if the physical morphology of the sorbent is known. Often the specific pore volume (SPV) for a given sorbent is expressed by the manufacturer (in units of volume per mass) and represents the volume of the particle that is empty or occupied by pores,  $V_{SPV}$ . From the SPV value, and the density of the sorbent's skeleton ( $\rho_{silica}$ ),  $\varepsilon_{intraparticle}$  can be calculated from equation 4-7.

$$\varepsilon_{intraparticle} = \frac{V_{SPV}}{V_{SPV} + \rho_{silica}^{-1}} \quad \text{Equation 4-7}$$

Expanded in Equation 4-8 is the fraction of the column containing the liquid volume,  $\varepsilon_t$ , expressed in terms of volume fractions or specific regional porosities.

$$\varepsilon_t = (1 - \varepsilon_{interparticle})\varepsilon_{intraparticle} + \varepsilon_{interparticle} \quad \text{Equation 4-8}$$

One important caveat is the true value of  $\varepsilon_{intraparticle}$  is often unknown as the reported SPV measurements are conducted prior to stationary phase bonding. Bonding of a specific ligand can account for a significant fraction of the total pore volume, especially if there is a population of micropores that are fully filled by the functionalization.

#### 4.3 Measurement of the Total Liquid Fraction for 1.3 $\mu\text{m}$ BEH Capillary Columns

#### 4.3.1 Materials and Methods

A complete listing of materials and generalized methods can be found in Appendix 1. Deviations from these procedures will be highlighted and explained within the respective section.

#### 4.3.2 Discussion of CLSM Results and Confirmation by Pycnometry

Interest and exploration into a column's total volume was spurred by the results of Chapter 2. As previously stated, the integral porosity deviation (IPD) describes the homogeneity of the packing porosity as a function of radial position from a capillary wall. Although an illuminating experimental result that highlights localized porosity, this measurement is normalized for the bulk packing porosity and does not account for any potential anomalies in this value.

Closer inspection of the resulting value for  $\epsilon_{interparticle}$  for the reconstructed sections, especially for the columns packed with 1.3  $\mu\text{m}$  BEH particles, is somewhat troubling. Plotted in Figure 4-1 are the radial porosity profiles for the three reconstructed columns previously discussed in Chapter 2. This plot displays the local porosity,  $\epsilon(r)$ , as interstitial void volume fraction as a function of radial positioning. Here,  $r = 0$ , represents the wall of the capillary column and the first, highly ordered, layer of particles in direct contact with the wall is indicated at the minimum at  $r \approx 0.5 d_p$ . This point represents the center of the particle within the first ordered layer and is apparent for all columns. As the distance increases, the oscillations dampen into random bulk behavior. Most importantly, all columns studied show very high bulk porosity,  $\epsilon_{bulk} = 0.47 - 0.50$ , far exceeding the random-close pack limit of 0.35 and even theoretical maxima loose packing limits for frictional spheres [4-10]. These porosities are particularly surprising, as one would expect

bed collapse, especially given UHPLC operating conditions. An important observation is the continued trend from previous work with larger BEH particles packed under similar conditions. Here  $\varepsilon_{bulk} = 0.44$  for  $d_p = 1.7 \mu m$  and  $\varepsilon_{bulk} = 0.39$  for  $d_p = 1.9 \mu m$  [13]. This is an expected trend even though final porosity is highly dependent on particle properties and packing methods [14,15]. Columns were visually inspected as much as 2 years after initial characterization and no visible signs of bed collapse (i.e. gaps in the packing) were observed. For example, an extruded section of the packing was dried, mounted onto a sample holder and exposed to a strong stream of nitrogen gas prior to SEM imaging. The resulting image, especially the anchored branch of packing, in Figure 4-2 highlights the stability and cohesion of the bed structure formed by the packing of the  $1.3 \mu m$  BEH particles.

The large and seemingly improbable bulk porosity values were confirmed by a few independent methods. The PSD of the columns reconstructed by confocal laser scanning microscopy (CLSM) correspond well with PSD of SEM values Figure 4-3. Using the total number of particles analyzed within each CLSM reconstruction in conjunction with the SEM-based PSD data, a possible volume occupied by particles was determined and divided by the total reconstructed column volume. The results were indistinguishable estimates of porosity compared to the actual reconstructions.

The columns were also assessed with pycnometry to confirm these larger porosities. An average mass difference of  $\Delta m = 1.070 \text{ mg}$  was determined between the dry  $24 \text{ mg/mL}$  column and the liquid filled column.  $V_L$  was calculated using the density of the filling liquid ( $\rho_{liquid} = 0.9070 \text{ g/mL}$ ) and Equation 4-9.

$$V_L = \frac{\Delta m}{\rho_{liquid}} \quad \text{Equation 4-9}$$

Equation 4-1 and the columns physical dimensions, column length ( $L = 33.6 \text{ cm}$ ) and the

internal radius of the column ( $r_c = 37.5 \mu m$ ), allowed for the determination of  $V_{blank} \cdot \varepsilon_T$  was then determined from Equation 4-2.

The SPV of the BEH particles ( $V_{SPV} = 0.70 \text{ cm}^3/g$  provided by Waters Corporation) and the density of the BEH skeleton ( $\rho_{silica} = 2.00 \text{ g/cm}^3$ ) were implemented in Equation 4-7 to calculate the value of  $\varepsilon_{intraparticle}$ . The calculated value for  $\varepsilon_{intraparticle}$  of 0.6 agrees well with previously reported BEH material [16]. Incorporation of these values into Equation 4-10 yields a value for  $\varepsilon_{interparticle}$  of 0.49.

$$\varepsilon_{interparticle} = \frac{\varepsilon_T - \varepsilon_{intraparticle}}{1 - \varepsilon_{intraparticle}} \quad \text{Equation 4-10}$$

The calculated external porosity,  $\varepsilon_{interparticle}$ , lies between the values of the 20 mg/mL column and 40 mg/mL column (0.48 and 0.50 respectively). The high porosities were thus experimentally confirmed. Moreover, confirmation by pycnometry yields the total possible liquid volume in the column exclusive of solvent effects. As the column was first dried and then wetted this result closely matches the CLSM imaging measurements.

#### 4.3.3 Anomalous Total Volume Percentages as Measured by an Unretained Marker

Although independently accounted for by both computation and pycnometry methods, the measurements should also be easily confirmed by measurements of our dead time marker, AA, and the measured flow rate. The ensuing discussion focuses on experiments conducted that yielded highly anomalous results and attempts to explain the measurement.

Confirmation of the AA elution time from the 24 mg/mL column run in 50:50 water:MeCN + 0.1% trifluoroacetic acid (TFA) is presented in Figure 4-4. Here the measured dead time for a test nearly 2 years after initial characterization fits well on the initial curve of dead time vs. pressure. Thus, the initially measured elution times for AA were used for

calculations. For these experiments, the flow rate was measured using Kimble 10  $\mu\text{L}$  (to contain) glass pipettes (Sigma Aldrich, St. Louis, MO). These measurements were conducted by slipping the column's outlet into the calibrated pipette. The position of the meniscus was then measured as a function of time, which was converted to a volume per unit time. A plot of measured flow rates for this column is shown in Figure 4-5. Using the line of best fit, a flow rate could be found for each recorded elution time and the total liquid volume for this column could be determined from multiplication of these two values. The resultant represents the total column liquid fraction explored by the marker. This measurement is plotted in Figure 4-6 as a function of pressure. The result should be nearly consistent across the pressure range and a correction was made for mobile phase compressibility, 71 ppm/bar (this value is approximate at 20  $^{\circ}\text{C}$  [17]) for 50:50 water:MeCN. The correction is overlaid in Figure 4-6 and significantly flattens the liquid fraction measurement as a function of pressure. The value for  $\varepsilon_T$  settles around 0.5, much lower than expected when measurements by pycnometry approach 80% and CLSM imaging suggests that the value of  $\varepsilon_{interparticle}$  should be around 0.49.

Experiments were conducted to test each variable in the calculation. First, the dead time marker was studied to make sure it was exploring the total column volume. Figure 4-7 plots overlays of various dead time markers and agreement between their elution times is presented. It was considered that a charge based exclusion could be the source of the error and so Donnan exclusion from the pores was explored, using sodium nitrate as a dead time marker, with and without a 150 mM concentration of NaCl in the mobile phase. The results of these experiments are presented in Figures 4-8 and 4-9. An insignificant change in relative retention time between sodium nitrate, an inorganic salt, and AA was observed, confirming

the use of AA as a dead time marker in 50:50 water:MeCN as appropriate (Note Figures 4-8 and 4-9 were run at different pressures explaining the shift in elution time). Second, the method to measure flow rate was studied. Figure 4-10, plots the measured flow rate under different experimental conditions. One method was microscope aided to more accurately track the position of the meniscus as a function of time. Another measurement technique incorporated a saturated atmosphere environment (the saturated atmosphere could avoid potential evaporation of the mobile phase stored in the pipette). The saturated atmosphere measurement was conducted by pushing the glass 10  $\mu$ L pipette through a rubber stopper that plugged a vial filled with identical mobile phase. As seen in Figure 4-10, all slopes overlay suggesting the original flow rate measurement was accurate. A further experiment to make sure the pipettes themselves were not to blame involved connecting the column outlet to a small section of 75  $\mu$ m i.d. pulled capillary that was functionalized in n-butyltrimethylchlorosilane (Gelest, Morrisville, PA) and measuring the formation of a liquid bubble through a calibrated microscope. The bubble was formed in a glass cell filled with mineral oil (Fisher Scientific, St. Louis, MO). The tip was functionalized with n-butyltrimethylchlorosilane to prevent the eluent from adhering to the pulled, and bare, fused silica tip. Modeling the bubble as a sphere, relatively good correlation in measure flow rate with a pipette can be seen (Figure 4-11) for 50:50 water:MeCN. Better correlation was achieved as the mobile phase was increased in water concentration to 80% as seen in Figure 4-12. This mitigated loss in bubble volume due to MeCN partition into the mineral oil. One can see that the slopes are nearly identical, suggesting that the flow rate measurements were not the source of the anomalous measurements. The results of these experiments led us to the conclusion that neither of the individual measurement methods under these conditions caused

the low total liquid volumes.

#### **4.4 Total Column Liquid Volume as a Function of Mobile Phase, Particle Size and Bonding**

To further delve into this anomaly, a series of experiments were conducted to assess the interdependence on mobile phase composition, particle size and bonded phase on total volume determination from a dead time and flow rate measurement.

##### **4.4.1 Modifications to Materials and Methods**

Methods for column packing and measurement were slightly altered for these experiments. Columns packed with C18 functionalized material were slurried to 30 mg/mL in tetrahydrofuran (THF). Hydrophilic interaction chromatography (HILIC) material was slurried at 30 mg/mL in acetone. In all cases, acetone was used as the pushing solvent and columns were packed at a maximum pressure of 24 kpsi. Due to very low operating pressures (<6 kpsi) no bed consolidation steps were performed.

A nanoACQUITY instrument (Waters Corporation) with a prototype on-column UV detection scheme was used for detection. Uracil and toluene were used as dead time markers and were detected at 243 and 216 nm respectively. Flow rates were confirmed (using 10  $\mu$ L pipettes used in the previously discussed flow rate measurements) and fell within the manufacturer's 2% variance. Inlets of the columns were fritted using the Kasil method as described in Appendix 1. The outlets were pushed into a union filled with glass microfiber to create an outlet frit. A small window was created at the detection point with a razor blade. Injections were made with a 10 nL 4 port injector (Valco, TX) and capillary columns were directly connected to the injector. 100% THF mobile phases were implemented with a 1 m x 180  $\mu$ m capillary storage loop connected to a 6 port injector (Valco, TX). 85% MeCN was used as a pushing solvent in this case to closely match the viscosity of THF. Total extra

column band broadening was minimized due to on-column detection and direct injection onto the capillary column.

Four particle types were studied: 1.7, 1.36, 0.96  $\mu\text{m}$  C18 functionalized BEH, and bare 1.7  $\mu\text{m}$  BEH, HILIC material. In all cases, packing of the columns was smooth and performed as expected. The particles used in these experiments were not measured with SEM imaging so manufacturer's reported sizes (based on Coulter counter measurements) are used for identification. The reader should note that BEH material sized by Coulter counter methods is typically sized 0.2  $\mu\text{m}$  less than SEM image based sizing. This is due to slight conductivity of the porous particles.

#### **4.4.2 Effects of Mobile Phase Percentage, Particle Size, and Bonding**

To assess the implications of a mixed mobile phase, the percentage of MeCN was increased from 50 to 100% for each of the three C18 bonded sorbents. The data for total column volume percentage is summarized in Table 4-1. When the %MeCN increases from 50 to 100%, the total volume probed by uracil increases to a maximum value just under 60% for all particle diameters. The lowest liquid volume percentage within the column is reported for mobile phase compositions around 50 to 60% MeCN. This increase is indicative of the uracil's inability to fully probe into the pores of the material, as the interparticle bed structure remains consistent within each capillary column. This can be explained by uracil's ability as a dead time marker to distinguish between the absorbed and enriched MeCN layers at the surface of the particle's skeleton where the C18 interfaces with the liquid phase. It is clear that mixed mobile phases are not appropriate for true dead time measurements as a dynamic layer of enriched organic solvent is located at the surface of the particles and has a variable thickness related to the mobile phase composition.



Toluene was used as an alternative dead time marker for its expected ability to better access the absorbed MeCN layer and bonded C18. Table 4-2 shows the results for toluene as a dead time marker in 100% MeCN. Initially promising, the results are indicative of reasonable values for the total liquid volume within the column, around 70%. However, closer inspection shows no difference in total liquid volume for the 1.36 and 0.96  $\mu\text{m}$  BEH materials. In fact, both results suggest identical values for  $\varepsilon_{interparticle}$  as the BEH materials should both exhibit identical values for  $\varepsilon_{intraparticle}$ . From previous CLSM data and the general trend of less densely packed beds as a function of decreasing particle size, an alternative answer exists. Consistency in total surface area and bonding is very high for all BEH material. Thus, if toluene is slightly retained in 100% MeCN we would expect very similar values of total probed liquid volume, similar to what is seen here. To confirm this finding, a mobile phase of 100% THF was used and the results are listed in Table 4-3.

In 100% THF, the total column volumes approach 62% for columns packed with 1.36  $\mu\text{m}$  BEH sorbent and just over 70% for columns packed with 0.96  $\mu\text{m}$  BEH sorbents. As these values differ greatly, it is clear that this system is no longer dependent on any form of retention. Again, because these batches only differ in particle size, the bonding and surface area are identical and any difference in total liquid volume is solely based on packing density. Furthermore, these values highlight and confirm the trends of packing density as a function of particle diameter discussed previously. Using Equation 4-4, one can confirm that smaller particles, approaching 1  $\mu\text{m}$  in diameter, have a tendency to pack less densely. These values are outlined in Table 4-4.

Incorporation of values similar to those found through CLSM confirm the experimental results. These calculations account for the nearly 10% difference in total liquid

volume, and implementation of identical values for  $\epsilon_{intraparticle}$  in the calculations accounts for the identical morphology of the BEH material. Although the value used in these calculations for SPV are smaller than that reported by the manufacturer, it is not unreasonable. Again, this is because one must account for the volume taken up by the C18 functionalization. The SPV is measured prior to bonding and is not an accurate portrayal after functionalization. Differing from the pycnometry experiment, the column is never dry and devoid of all solvating mobile phase. This experiment explains the anomaly in the previous studies (mixed mobile phases cause an enriched layer that is distinguishable by many dead time markers) and highlights 100% THF and a toluene dead time marker as an appropriate experimental condition for total volume determination.

A final confirmation of this result is seen with the HILIC material. This material is a bare organic hybrid and not functionalized. The material is measured as 1.7  $\mu\text{m}$  (1.9  $\mu\text{m}$  by SEM). The results of experiments with this material are presented in Table 4-5.

The total liquid volume in this situation is measured at ~72% for both mobile phases, 100% MeCN and 100% THF with toluene as a dead time marker. Interestingly a similar effect in an enrichment of a stagnant layer of liquid is seen. In this case a layer of water is absorbed to the silica surface and reduces, as the percent organic is increased systematically. Interpretation of these results provides a clear example of reasonability for the methodology and confirmation of the manufacturer's measured SPV. Using 0.4 as  $\epsilon_{interparticle}$  (based CLSM images of similarly sized particles and traditional values for random packed spheres), and the manufacturer's reported SPV of 0.7, one finds very good agreement between measured values (Table 4-5) and expected values (Table 4-6). The relatively minor percent difference between 72 and 76% could be explained by previously unexplored packing density

of bare material.

#### **4.5 Conclusions**

The experiments presented here highlight the dramatic impact of an enriched MeCN phase that develops in reversed phase chromatography. The layer's thickness is a function of %MeCN and inhibits certain dead time markers from complete exploration of the pores. The model system described earlier (Section 4.2.1) is thus too simple for mixed solvent systems. Instead a minimum of three layers must be used to describe the composition of liquid as function of position inside a pore. For example, considering 50:50 water:MeCN as a mobile phase, the model system must be modified to describe a transition from true mobile phase, to an enriched MeCN layer, to the C18 bonding and finally to the silica support skeleton. In all, to determine the true column volume with a dead time and measured flow rate one must use a single component mobile phase system with an appropriate marker. Further exploration of this effect could lead to more detailed understanding of packing density as a function of particle size and the absorbed thickness of the organic layer on C18 functionalized particles or the absorbed layer of water on HILIC particles.

#### 4.6 Tables

<u>% MeCN</u>	<u>% Liquid Volume</u>	<u>% Liquid Volume</u>	<u>% Liquid Volume</u>
	<u>1.7 <math>\mu\text{m}</math></u>	<u>1.36 <math>\mu\text{m}</math></u>	<u>0.96 <math>\mu\text{m}</math></u>
50	53.6	52.9	55.1
60	52.9	55.2	55.0
70	53.4	55.8	54.8
80	53.9	56.3	55.7
90	54.3	57.6	56.4
100	56.4	59.1	57.9

**Table 4-1.** The total liquid volume percentage as a function of %MeCN while using uracil as a dead time marker. The dimensions and flow rates for these columns were as follows: 1.7  $\mu\text{m}$  C18 BEH (9.95 cm x 75  $\mu\text{m}$  i.d., 0.38  $\mu\text{L}/\text{min}$ ), 1.36  $\mu\text{m}$  C18 BEH (a 9.8 cm x 75  $\mu\text{m}$  i.d., 0.15  $\mu\text{L}/\text{min}$ ), 0.96  $\mu\text{m}$  C18 BEH (8 cm x 75  $\mu\text{m}$  i.d., 0.15  $\mu\text{L}/\text{min}$ ).

<u>d<sub>p</sub> (μm)</u>	<u>L (cm)</u>	<u>i.d. (μm)</u>	<u>% Liquid Volume</u>
1.36	9.8	75	73.0
0.96	8	75	71.3

**Table 4-2.** Dimensions of the columns and results of the total liquid fraction in a 100% MeCN mobile phase with toluene used as a dead time marker.

<u>d<sub>p</sub> (μm)</u>	<u>L (cm)</u>	<u>i.d. (μm)</u>	<u>t<sub>m</sub> Marker</u>	<u>% Liquid Volume</u>
1.36	9.9	75	Toluene	61.8
0.96	8	75	Toluene	73.8
0.96	7.25	75	Toluene	71.9

**Table 4-3.** Dimensions of the columns and results of total liquid fraction in a 100% THF mobile phases with toluene used as the dead time marker.

	<u>1.36 <math>\mu\text{m}</math> C18 BEH</u>	<u>.96 <math>\mu\text{m}</math> C18 BEH</u>
$\varepsilon_{\text{interparticle}}$	0.44	0.48
$1 - \varepsilon_{\text{interparticle}}$	0.56	0.52
$\varepsilon_{\text{intraparticle}}$	0.40	0.40
$(1 - \varepsilon_{\text{interparticle}}) \varepsilon_{\text{intraparticle}}$	0.22	0.21
$\varepsilon_{\text{interparticle}} + (1 - \varepsilon_{\text{interparticle}}) \varepsilon_{\text{intraparticle}}$	0.66	0.73

**Table 4-4.** Presentation of porosity fractions calculated from an assumption of  $\varepsilon_{\text{interparticle}}$  from previous CLSM studies.

<u>% MeCN</u>	<u>% THF</u>	<u>% Liquid Volume</u>
85	0	68.4
95	0	70.6
100	0	72.0
0	100	71.5

**Table 4-5.** Total liquid volume of a column expressed as a percentage for a 9.5 cm x 75  $\mu\text{m}$  i.d. column packed with 1.7  $\mu\text{m}$  HILIC material. In all cases toluene was used as the dead time marker and the flow rate was 0.38  $\mu\text{L}/\text{min}$ .



	<u>1.7 <math>\mu\text{m}</math> HILIC</u>
$\epsilon_{\text{interparticle}}$	0.40
$1 - \epsilon_{\text{interparticle}}$	0.6
$\epsilon_{\text{intraparticle}}$	0.6
$(1 - \epsilon_{\text{interparticle}}) \epsilon_{\text{intraparticle}}$	0.36
$\epsilon_{\text{interparticle}} + (1 - \epsilon_{\text{interparticle}}) \epsilon_{\text{intraparticle}}$	0.76

**Table 4-6.** Presentation of porosity fractions calculated from an assumption of  $\epsilon_{\text{interparticle}}$  from previous CLSM studies and a report of a manufacturer's value for  $\epsilon_{\text{intraparticle}}$ .

## 4.7 Figures

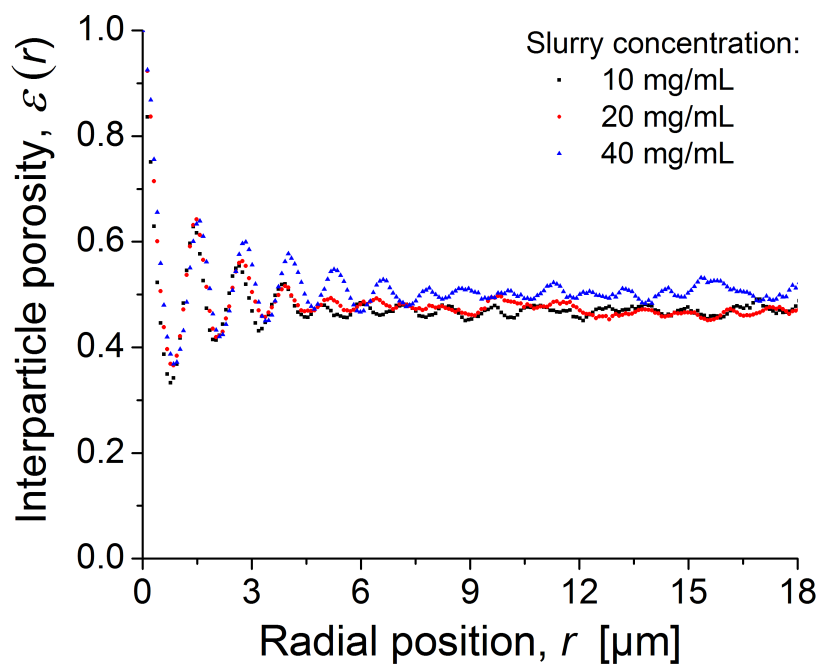


**Figure 4-1.** Radial porosity profiles for columns packed with 1.3  $\mu\text{m}$  BEH particles at three slurry concentrations. The interstitial void volume fraction as a function of position is plotted from the wall of the capillary column to 18  $\mu\text{m}$  into the capillary column.

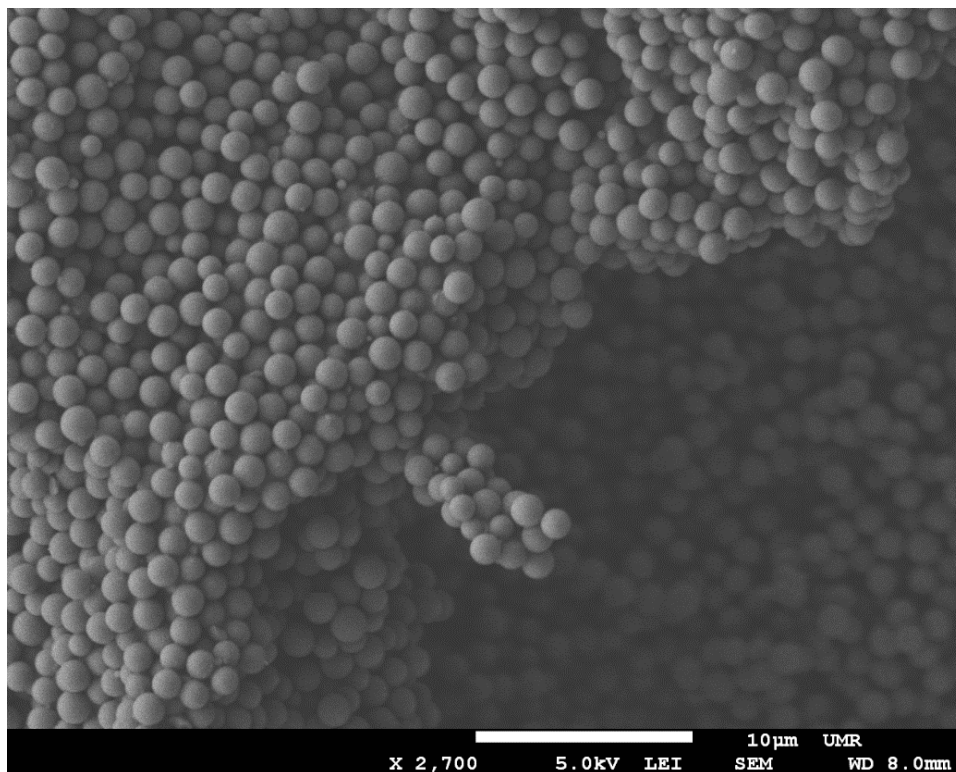


**Figure 4-2.** SEM image of an extruded section of the bed for a 15 mg/mL packing of 1.3  $\mu\text{m}$  BEH particles. The extruded portion of the packed bed was dried, mounted and exposed to a strong nitrogen stream. A rigid bed structure is firmly anchored and indicative of particle cohesion.

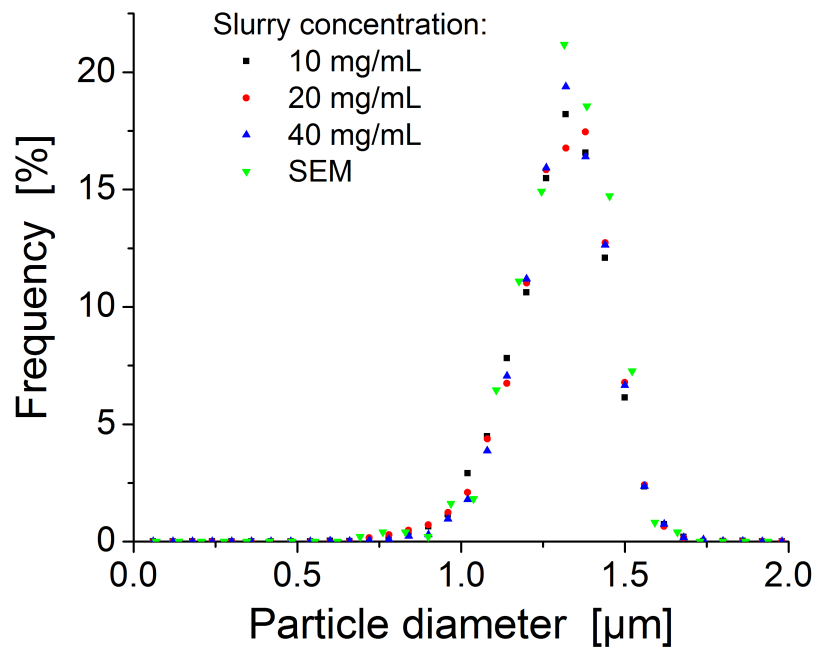


**Figure 4-3.** Particle size distribution for the 1.3  $\mu\text{m}$  BEH particles as measured by CLSM images and SEM images.

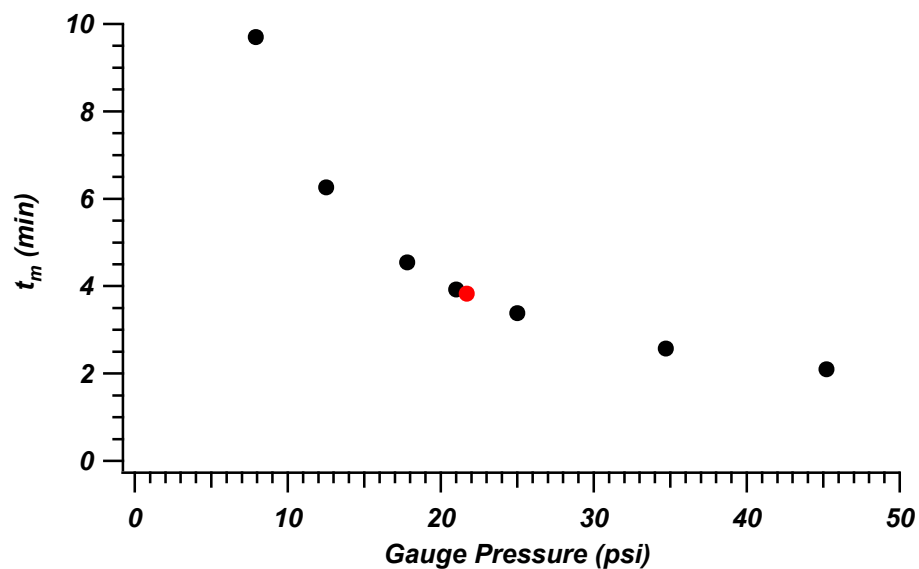


**Figure 4-4.** Plot of  $t_m$  vs. the gauge pressure (actual applied pressure is multiplied by 1038) for 24 mg/mL, 33.6 cm x 75  $\mu\text{m}$  column packed with 1.3  $\mu\text{m}$  BEH particles used for pycnometry. Points plotted in black were from the original column characterization. The red point is from the column stability confirmation approximately two years later.

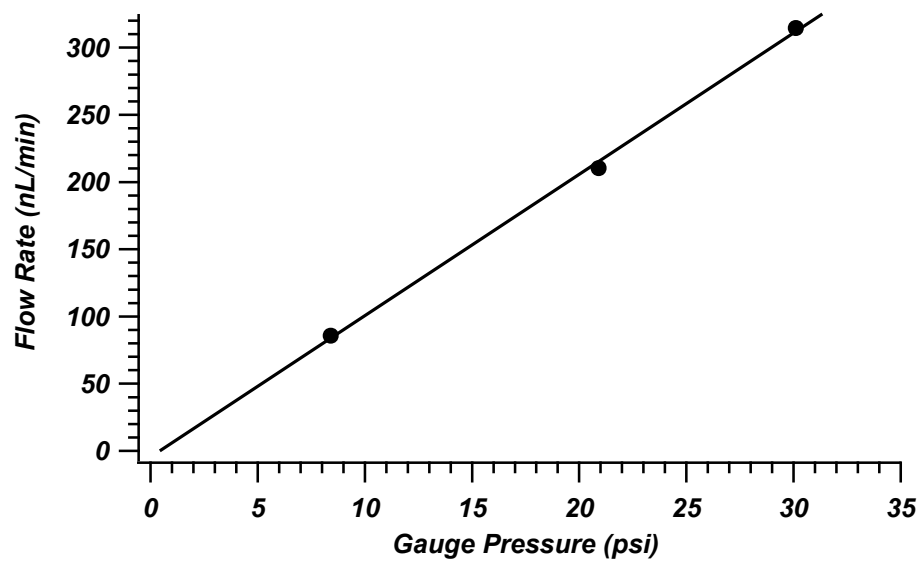


**Figure 4-5.** Plot of flow rate vs. the gauge pressure (actual applied pressure is multiplied by 1038) for 24 mg/mL, 33.6 cm x 75  $\mu\text{m}$  column packed with 1.3  $\mu\text{m}$  BEH particles used for pycnometry.

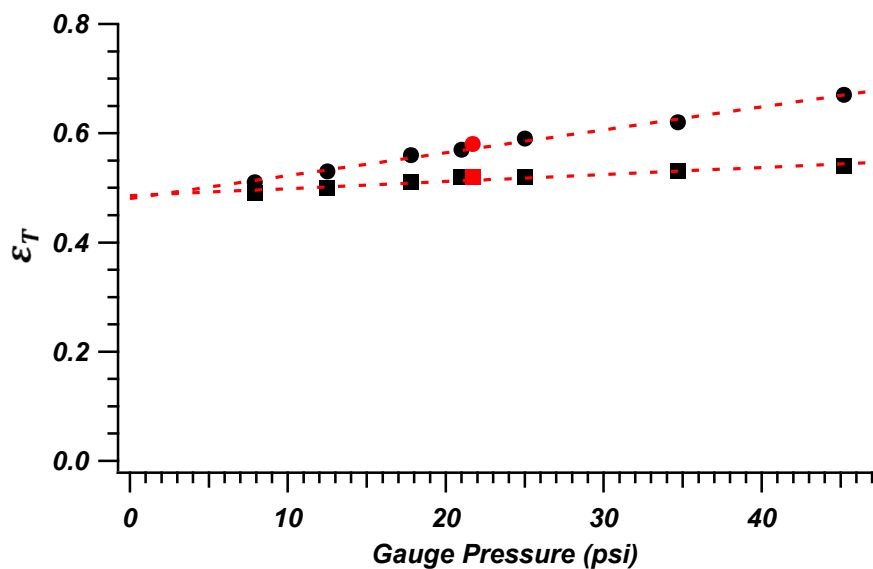


**Figure 4-6.** Plot of  $\epsilon_T$  vs. the gauge pressure (actual applied pressure is multiplied by 1038) for 24 mg/mL, 33.6 cm x 75  $\mu\text{m}$  column packed with 1.3  $\mu\text{m}$  BEH particles used for pycnometry. Points plotted with circles are the direct resultant of experimental measurements. Points plotted in squares represent a 71 ppm/bar pressure correction for mobile phase compressibility. Points plotted in red represent the result of experiments conducted approximately 2 years after initial characterization. Dashed red lines are lines of best fit. Notably, at low pressure both intercept at nearly the same  $\epsilon_T$ .

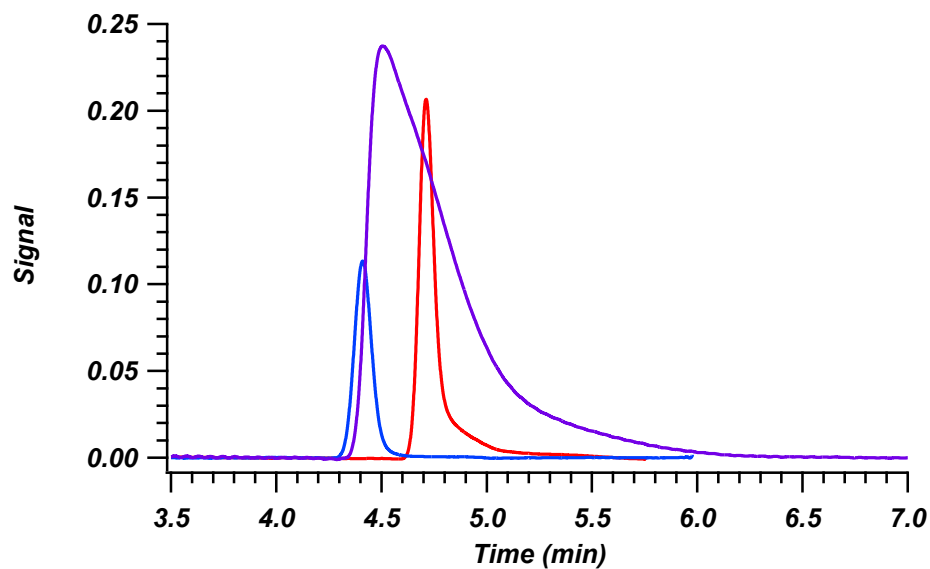


**Figure 4-7.** Plot of three different dead time markers: ascorbic acid (blue), thiourea (red), sodium nitrate (purple). All samples were run in 50:50 water:MeCN for 24 mg/mL, 33.6 cm x 75  $\mu$ m column packed with 1.3  $\mu$ m BEH particles later used for pycnometry. Detection was conducted by UV absorbance at 230 nm with a 75  $\mu$ m capillary butt connected to the end of the capillary column.



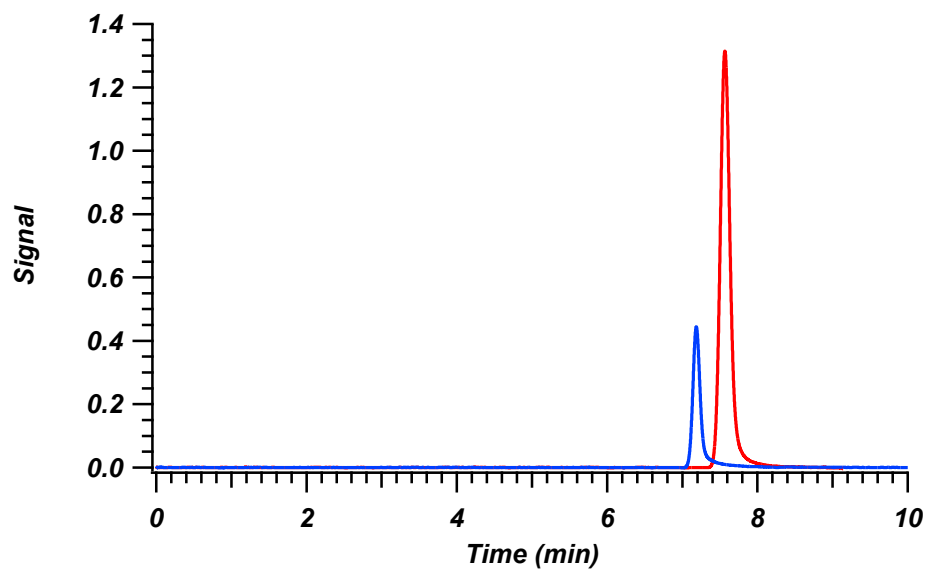


**Figure 4-8.** Chromatogram for the 24 mg/mL, 33.6 cm x 75  $\mu\text{m}$  column packed with 1.3  $\mu\text{m}$  BEH particles used for pycnometry. The mobile phase used is 80:20 water:MeCN + 0.1% TFA and run at 21 kpsi. Ascorbic acid is plotted in red and sodium nitrate is plotted in blue. Detection was conducted at 230 nm with a 75  $\mu\text{m}$  i.d. capillary butt connected to the capillary column.

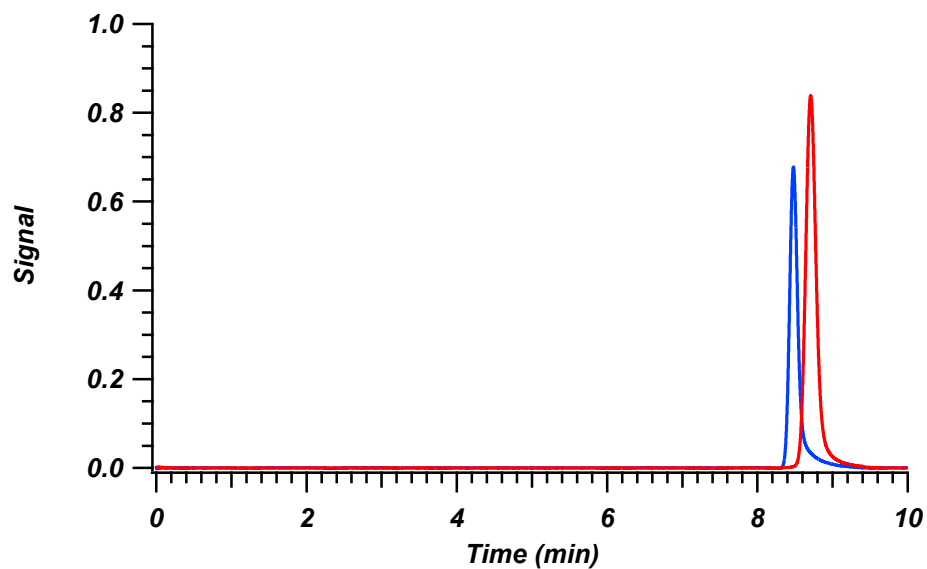


**Figure 4-9.** Chromatogram for the 24 mg/mL, 33.6 cm x 75  $\mu$ m column packed with 1.3  $\mu$ m BEH particles used for pycnometry. The mobile phase used is 150 mM NaCl in 80:20 water:MeCN + 0.1% TFA and run at 15 kpsi. Ascorbic acid is plotted in red and sodium nitrate is plotted in blue. Detection was conducted at 230 nm with a 75  $\mu$ m i.d. capillary butt connected to the capillary column.

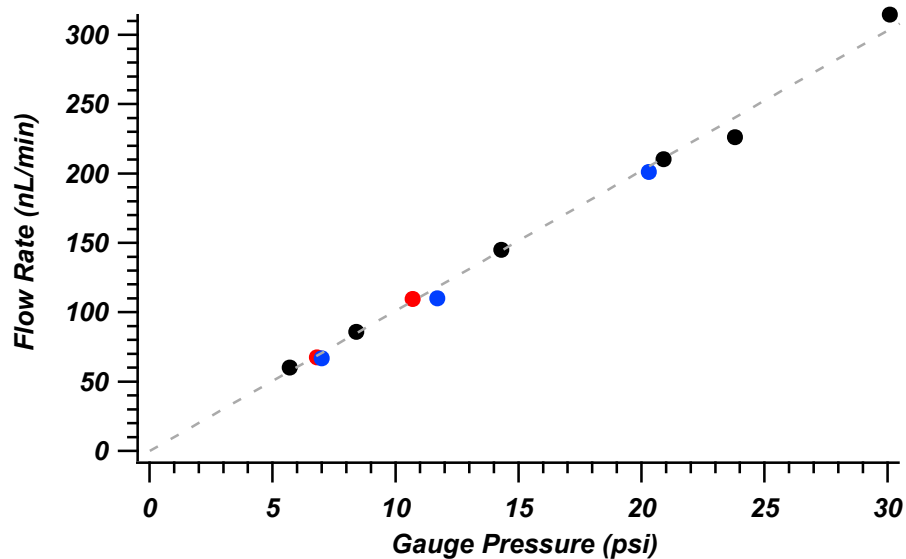


**Figure 4-10.** Plot of flow rate vs. the gauge pressure (actual applied pressure is multiplied by 1038) for 24 mg/mL, 33.6 cm x 75  $\mu\text{m}$  column packed with 1.3  $\mu\text{m}$  BEH particles used for pycnometry. Colors of points represent the following methods: black- normal unaided measurements, red- microscope aided measurements, blue- saturated atmosphere aided measurements. The gray dashed line is the line of best fit for the normal, unaided measurements.

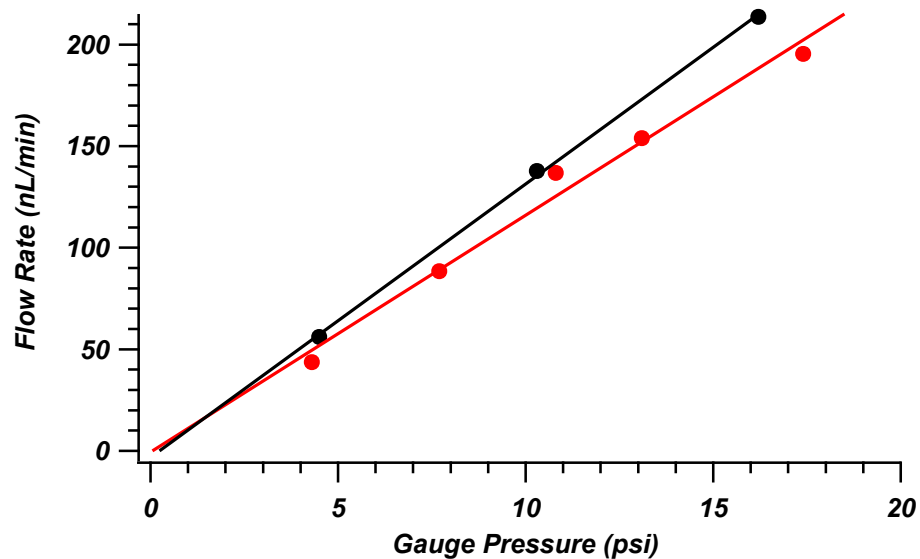


**Figure 4-11.** Plot of flow rate vs. the gauge pressure (actual applied pressure is multiplied by 1038) for 24 mg/mL, 33.6 cm x 75  $\mu\text{m}$  column packed with 1.3  $\mu\text{m}$  BEH particles used for pycnometry. Flow rate measurements were conducted by the “bubble method” in 50:50 water:MeCN and presented in red, while flow rate measurements made with a 10  $\mu\text{L}$  capillary are presented in black.

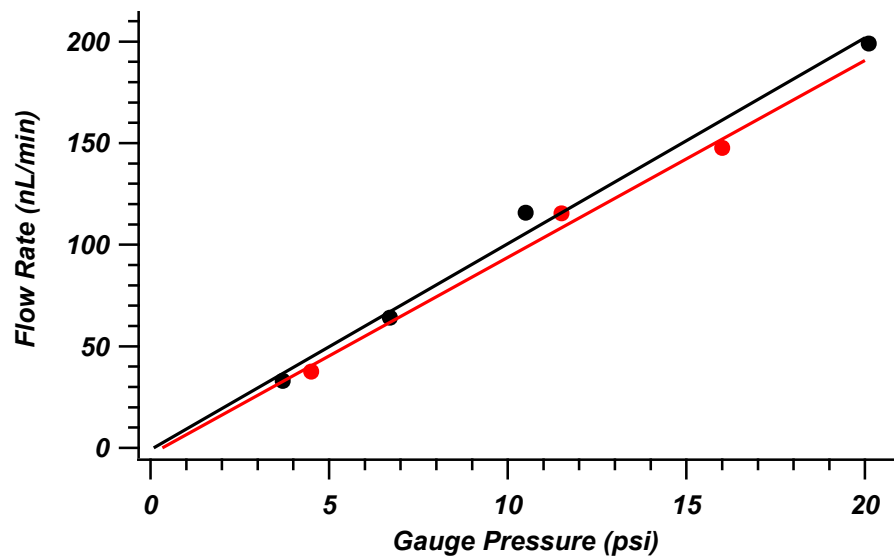


**Figure 4-12.** Plot of flow rate vs. the gauge pressure (actual applied pressure is multiplied by 1038) for 24 mg/mL, 33.6 cm x 75  $\mu\text{m}$  column packed with 1.3  $\mu\text{m}$  BEH particles later used for pycnometry. Flow rate measurements were conducted by the “bubble method” in 80:20 water:MeCN.

## 4.8 REFERENCES

- [1] F. Gritti, G. Guiochon, *J. Chromatogr. A* 1253 (2012) 71–82.
- [2] F. Gritti, J.J. Stankovich, G. Guiochon, *J. Chromatogr. A* 1263 (2012) 51–60.
- [3] K.M. Fague, Ph.D. Dissertation, The University of North Carolina at Chapel Hill, 2014.
- [4] V. Baranau, U. Tallarek, *Soft Matter* 10 (2014) 3826–3841.
- [5] G.Y. Onoda, E.G. Liniger, *Phys. Rev. Lett.* 64 (1990) 2727–2730.
- [6] Z.P. Zhang, L.F. Liu, Y.D. Yuan, A.B. Yu, *Powder Technol.* 116 (2001) 23–32.
- [7] C. Song, P. Wang, H.A. Makse, *Nature* 453 (2008) 629–632.
- [8] M. Jerkins, M. Schröter, H.L. Swinney, T.J. Senden, M. Saadatfar, T. Aste, *Phys. Rev. Lett.* 101 (2008) 018301.
- [9] G.R. Farrell, K.M. Martini, N. Menon, *Soft Matter* 6 (2010) 2925–2930.
- [10] L.E. Silbert, *Soft Matter* 6 (2010) 2918–2924.
- [11] C.A. Rimmer, C.R. Simmons, J.G. Dorsey, *J. Chromatogr. A* 965 (2002) 219–232.
- [12] D. Cabooter, F. Lynenb, P. Sandrab, G. Desmet, *J. Chromatogr. A* 1157 (2007) 131–141.
- [13] S. Bruns, E.G. Franklin, J.P. Grinias, J.M. Godinho, J.W. Jorgenson, U. Tallarek, *J. Chromatogr. A* 1318 (2013) 189–197.
- [14] R.Y. Yang, R.P. Zou, A.B. Yu, *Phys. Rev. E* 62 (2000) 3900–3908.
- [15] A.B. Yu, C.L. Feng, R.P. Zou, R.Y. Yang, *Powder Technol.* 130 (2003) 70–76.
- [16] K.D. Wyndham, J.E. O’Gara, T.H. Walter, K.H. Glose, N.L. Lawrence, B.A. Alden, et al., *Anal. Chem.* 75 (2003) 6781–6788.
- [17] W.M. Haynes, CRC Press: Boca Raton, FL, 2015.

## **Chapter 5. Impact of Column Length and Methods to Analyze Localized Axial Heterogeneity Amongst Subsections of Packed Capillary Columns**

### **5.1 Introduction**

There are two main options to increase the efficiency, or the number of theoretical plates ( $N$ ), of a liquid chromatography column. One can increase the column's length ( $L$ ) and/or, one may work to decrease the height equivalent to the theoretical plate (HETP) (Equation 1-8). Previous chapters have focused on the latter. Briefly, Chapter 2 discusses insights made into the column packing process that relate the packed bed's microstructure to the resulting HETP. The use of localized reconstructions and analyses of specific regions of the packed capillary column, via confocal laser scanning microscopy (CLSM), have shown how certain structures can greatly affect performance and why certain columns perform well [1-3]. These results have helped guide packing protocols to maximize the resulting efficiency of a column through a reduction of the HETP (Chapter 3). Unfortunately, the technique is only capable of a myopic view and results are based on single analysis points located in the middle of the capillary column. This is done in order to analyze a region "representative" of both the inlet and outlet of the column as the reconstruction and data workup time is highly intensive. This necessitates somewhat limited conclusions as to the entirety of the packing microstructures along the column's length. Although the results of this restricted view may be reasonably representative of average packing microstructures in short columns, it is likely hard pressed to represent all regions present in very long columns (those >50 cm).

The slurry packing process is highly dynamic and dependent on the interplay of many

variables. Although experiments to study and isolate these variables have been conducted, the compounding effect of  $L$  should not be underestimated [4]. For example, as  $L$  increases, the rate of flow into the column decreases as the bed builds. If modeled by the equation for flow rate in a packed bed, (Equation 1-22), one can quickly see that the increasing  $L$  of the packed bed will diminish the rate of material flow into the column. The decreasing rate of packing affects the energy associated with the incoming particles and the force in which they impact the already formed bed. It is likely that a decrease in impact force or even the time between impacts may allow for particle rearrangement or shifting prior to being locked into place within the final structure. Perhaps more important is the relation between the dynamic concentration of the slurry and the overall time needed to pack longer columns. Increased packing time may allow for a slurry ageing process that induces particle aggregation and rapid settling in the slurry reservoir [5]. This process could significantly dilute or concentrate the local slurry and depends on the positioning of the inlet of the column blank within the reservoir. Even more fundamentally, the total amount of material needed to pack longer columns may be significant enough to dilute the initial slurry concentration over the course of packing.

The following discussion underscores some of the effects of column length on packed capillary columns and presents methods to study axial heterogeneities. Here, an example meter long column, packed with an “optimized” slurry concentration, is examined and sectioned for detailed analysis. Additionally, a theoretical interpretation of localized performance in longer columns and its application to a methodology to assess column performance non-destructively over the column’s  $L$  will be discussed.

## **5.2 Materials and Methods**



The materials and methods used for column packing are discussed in Appendix 1. Deviations from these methods will be listed in appropriate sections. Materials, methods and design of different spectroscopic approaches will be listed within appropriate sections.

### **5.3 Axial Heterogeneities for “Optimized” Slurry Concentrations**

Chapter 2 highlights the results of slurry concentration optimization for the packing of reproducible and efficient capillary columns. Within these studies,  $L$  is held constant to isolate the effects of slurry concentration. In doing so, an optimum concentration that balances counteracting packing defects was found. With the HETP optimized within the set of experimental parameters, it logically follows to modify the  $L$  of the packed columns to maximize  $N$ .

Based on the optimization experiments for the 1.3  $\mu\text{m}$  bridged-ethyl hybrid (BEH) material, a slurry concentration of 20 mg/mL should yield high performing columns (Chapter 2). This concentration was chosen to pack a 1-meter long capillary column. Figure 5-1 presents the reduced van Deemter for this 100 cm x 75  $\mu\text{m}$  i.d. column in black. The resulting performance of this column is significantly worse than all columns used in the slurry concentration exploration experiments (Chapter 2). The minimum reduced plate height,  $h_{\text{min}}$ , for this long column is  $\sim 3$  while the reduced plate height for column packed with a 20 mg/mL slurry in the optimizing experiments was  $\sim 1.5$ .

To further explore this stark difference in performance, the column was split into three sections. Each resulting subsection was approximately 30 cm in length and individually characterized. The performance for each of these three subsections is overlaid in Figure 5-1. It is immediately evident that the original slurry optimization study holds true for the first packed section (that is the outlet section of the intact 1 meter long column). This, first packed

subsection (whose performance is plotted in red in Figure 5-1), produces nearly identical performance to the 34 cm column packed at 20 mg/mL in the original concentration optimization. Here the outlet section has a  $h_{\min}$  of  $\sim 1.6$ . For clarity this first packed subsection is plotted with the 20 mg/mL column from the slurry optimization studies (Figure 5-2). This result is unsurprising as the lengths are comparable and the slurry concentration optimization experiment was centered on this slurry concentration range.

The reason for the very poor performance of the 1- meter long column is due to the last packed, middle (blue) and inlet (green), sections (these two sections are also overlaid in Figure 5-1). The poor performances of these two subsections greatly mitigate the results of the concentration optimization study and demonstrate the importance of axial heterogeneities and the study thereof. Most importantly they highlight the importance of column  $L$  in the packing process and the necessity of its study as a column-packing variable.

The following sections develop a theoretical model of performance as a function of intact column subsections and its application to a method to conduct on-column detection. Two methods are explored, and one method is suggested as feasible for future studies of the effects on column  $L$ .

#### **5.4 Theory of Additive Plates**

The results of section 5.3 underscore the importance of each section in the packed capillary and how important packing additional length is to the overall column performance. Poor performing sections can easily mask relatively well performing subsections. Unfortunately, studying these effects by cutting of the capillary into subsections is time consuming (due to increased analysis time), possibly disturbs the packed bed and ruins the original long column. Thus, non-invasive detection methods to study different axial regions

were explored.

In order to interpret on-column detection methods, a model using additive plates must be implemented. Theoretically, one can interpret small “component” sections of a packed capillary as a series of smaller packed capillaries, each connected in such a way that no external band broadening needs to be accounted for. In this case each section has its own inherent performance, which can be added to another section’s performance assuming a proper weighting for the summed column length.

Let  $H_L$  represent the HETP for the entire column length (as measured at the outlet of a given column), and  $\bar{H}$  equal the weighted average of each individual HETP subsection,  $H_i$ . Each value of  $H_i$  is associated with each individual subsection length,  $l_i$ , of the total column length,  $L$ . Presented in Equation 5-1, an effective on-column detection method will yield agreement between  $\bar{H}$  and the  $H_L$ .

$$H_L = \bar{H} = \frac{\sum_{i=1}^n H_i l_i}{\sum_{i=1}^n l_i} \quad \text{Equation 5-1}$$

One can also apply this method to compare sections between different columns of varying particle diameter. Dividing all of the unreduced HETP parameters by the particle diameter puts Equation 5-1 into terms of reduced plate height (Equation 5-2) and allows for a universal method to compare subsections packed with different column parameters.

$$h_L = \bar{h} = \frac{\sum_{i=1}^n h_i l_i}{\sum_{i=1}^n l_i} \quad \text{Equation 5-2}$$

## 5.5 On-Column Detection

The additive nature of the HETP can be used to determine the regional performance of intact columns in a nondestructive manner assuming performance measurements can be made along the column. To do this, one needs to implement a method for on-column

detection. Fused silica capillaries, such as those implemented here, are coated with polyimide for ruggedness and flexibility. Although robust, it does limit the methods one can pursue to conduct on-column measurements. The coating is transparent in the near infrared region [6,7], and the fused silica is optically transparent (assuming the coating is removed). Alternative methods for on-column detection include conductivity. However these measurements are very sensitive to environmental disturbances [8].

Presented here are two approaches for on-column detection; near infrared fluorescence detection (NIRF), and on-column UV detection. Although both methods are theoretically appropriate, inherent issues in the chromatography prevent NIRF from being practical.

### **5.5.1 NIRF as a Method for On-Column Detection**

#### **5.5.1.1 Materials and Methods**

Materials and methods for creation of capillary columns and high pressure running equipment can be found in Appendix 1. Deviations from these methods, specific to the NIRF experiments, will be described here.

Figure 5-3 presents the design of the NIRF detector. The housing was machined from brass and the inside surfaces were spray painted black to prevent reflections. The aperture to slide the capillary in front of the laser was lined with PEEK tubing to prevent damage while positioning. Incorporated parts are labeled in the diagram and are described here. Lenses and filters were purchased from Edmund optics (Barrington, NJ). Two plano-convex lenses, 15 mm diameter x 15 mm focal length were used to collimate and focus the fluorescence emission onto the detector. Placed between these lenses was an 832-center wavelength, 25 mm diameter, 37 nm bandwidth, optical density 6, fluorescence filter. A 780 nm center

wavelength, 10 nm full width at half max, 25 mm diameter bandpass interference filter was used to eliminate any stray incident laser light. The detector was a Si photodiode with a spectral range of 320 to 1100 nm and peak sensitivity at 960 nm (Hamamatsu, Hamamatsu City, Japan). A 780 nm laser was sourced from StockerYale (now ProPhotonix, Salem, NH).

Before each use, a capillary column filled with the sample was positioned inside the detector. The laser's position was then adjusted to achieve maximum signal intensity. The analyte used for these experiments was IR 125 (Exciton, Dayton, OH) (Figure 5-4). The mobile phase used was 50:50 water:MeCN with a 50 mM pH 7.10 phosphate buffer.

#### **5.5.1.2 Results and Discussion**

To assess NIRF as a method to characterize subsections of long capillary columns, a 101 cm x 75  $\mu$ m long capillary was packed with 1.9  $\mu$ m BEH particles. This column was then run and IR 125 was detected at 11 points down the length of the column. The results are presented in Figure 5-5. The first peak occurs at approximately 21 minutes and corresponds to a length of 17 cm from the inlet. Each subsequent peak is the result of detection further down the column's length. Noise spikes are seen between each peak and are due to the movement of the capillary through the NIRF detector to the next region of detection.

Although initially promising, closer inspection of the results reveals an important flaw in the experiment. Figure 5-6 presents the physical detection position for each peak in Figure 5-5, as a function of elapsed experiment time. The slope of this line is equal to the analyte's velocity. It becomes immediately evident that the analyte accelerates as it travels down the column due to pressure-induced retention: that is increased retention at elevated pressures and thus a retention mechanism dependent on the pressure gradient across the column. The non-linearity in the velocity plot prevents the data from the NIRF method from

being interpretable. Plate heights cannot be compared as the analyte band is physically broadening due to fundamental chromatographic theory (for example longitudinal diffusion alone) but the detected peaks appear to narrow or at least broaden minimally due to increasing band velocity and less time spent in the region of detection. Another concern with this experiment is the photobleaching occurring of the fluorophore.

Unfortunately, there is a limited selection of NIRF molecules and most have very similar, large molecular structures, and are expected to exhibit the same pressure induced retention. Thus, NIRF was abandoned as a method of on-column detection.

### **5.5.2 On-Column UV Detection: Method and Proof of Concept**

#### **5.5.2.1 Materials and Methods**

Materials and methods for creation of capillary columns and high pressure running equipment can be found in Appendix 1. Deviations from these methods, specific to on-column UV detection experiments, will be described here.

On-column UV detection was conducted using a Linear UV/Vis 200 detector (Thermo Scientific, Waltham, MA) at 220 nm. The column was slid through the detection cell by physically moving the detector on a platform fit with casters. Windows were made along the length of the capillary column with application of fuming sulfuric acid dripped on the capillary to gently remove the polyimide coating. HQ was used as the test analyte and the mobile phase was 50:50 water:MeCN + 0.1% TFA.

#### **5.5.2.2 Results and Discussion**

To avoid the pressure induced retention of large NIRF molecules an approach using UV detection was developed. This approach focused on the detection of HQ. HQ is weakly retained with a retention factor of approximately 0.2 in 50:50 water:MeCN on C18 modified

BEH particles and thus reflects the kinetic column efficiency.

Suitability of this analyte was determined by measuring HQ's velocity down the length of a column and the results are presented in Figure 5-7. As seen in the highly linear velocity plot, HQ does not exhibit the same chromatographic issues as IR 125 and can be used to characterize the subsections of columns.

To prove the suitability of this experimental procedure a 106.4 cm x 75  $\mu$ m i.d. column, packed with 1.9  $\mu$ m BEH, was first characterized for efficiency electrochemically and yielded a  $h_L$  of 4.06. Next, the column was characterized at 5 points along its length at an identical running pressure. Equation 5-2 was applied to the data and the resultant  $\bar{h}$  was 4.26. The results of  $h_i$  for each subsection are presented in Figure 5-8 as a function of detection window (as measured from the column inlet). Values of  $h_L$  and  $\bar{h}$  are slightly different, likely due to the last approximately 5 cm of column not characterized by on-column detection but incorporated in the electrochemical detection scheme. Even so, the nearly identical values suggest suitability of this method to measure performance along subsections. In this example, the  $h_i$  along the column  $L$  trends in a similar manner to that seen in the previously discussed column that was physically split and electrochemically characterized (Section 5.3). Again, the first packed sections yield the best performance, while the last packed sections reduce the overall performance. Interestingly, the inlet section shows improved performance over the middle sections and may be due to the bed compression steps as this portion of capillary experiences 50 kpsi during flushing and was not disturbed by column splitting as in the previous example.

To further prove the effectiveness of this method, measurements were made at velocity extremes. In the c-term region (high reduced velocities,  $v$ ) column performance due

to packing microstructure is explored, as the bed microstructure affects the c-term contribution, which is the main component of band broadening at high  $v$ . Alternatively, in the b-term region (low  $v$ ) each subsection should yield nearly equivalent values of  $h_i$  as band broadening is most influenced by the consistent process of longitudinal diffusion.

Figure 5-9 and 10 present the results of an 80 cm x 75  $\mu\text{m}$  column packed with 1.9  $\mu\text{m}$  BEH particles run at reduced velocity extremes, 3.88 and 0.76, that respectively represent performance in the C and B-term dominate regions. As expected, change in performance as a function of axial position is seen in Figure 5-9 (c-term dominates) and the same trend in performance (that is worst performance at the inlet and best at the outlet) is seen. Figure 5-10 (b-term dominates) presents nearly identical performance for each position along the length, indicative of band broadening occurring due to the constant process of longitudinal diffusion. For each of these measurements good agreement is seen between  $h_L$  and  $\bar{h}$ :  $h_L = 5.29$  and  $\bar{h} = 5.11$  for the c-term dominated plot and  $h_L = 3.83$  and  $\bar{h} = 3.76$  for the b-term dominated plot. Again good correspondence between measurements at the end of the capillary column and those based on the weighted averages of each section highlight the suitability of the on-column detection method.

## 5.6 Conclusions

The results presented herein highlight the importance of  $L$  as an experimental packing variable. An example long column utilizing an “optimal” slurry concentration was shown to produce an overall poor performing column. However, once sectioned, the outlet of this long column yielded very high performance (nearly identical to that expected based on the previous study exploring slurry concentration as a packing variable). To assess the packing quality as a function of axial position a theoretical model is presented that weights the effects



of the column's individual subsections, each with its own intrinsic performance. This model was applied to an on-column UV detection scheme that can trace inherent column performance as a function of axial position. As the field of chromatography continues towards the use more efficient columns, the effects of  $L$  on the packing process cannot be underestimated. The methods presented here can help guide the methodology used to pack columns as one can detect the differences in performance across the column and relate them back to packing method. With these experimental methods one can determine which packing conditions produce not only the most efficient long capillary column but also the most axially homogenous one.

## 5.7 Figures

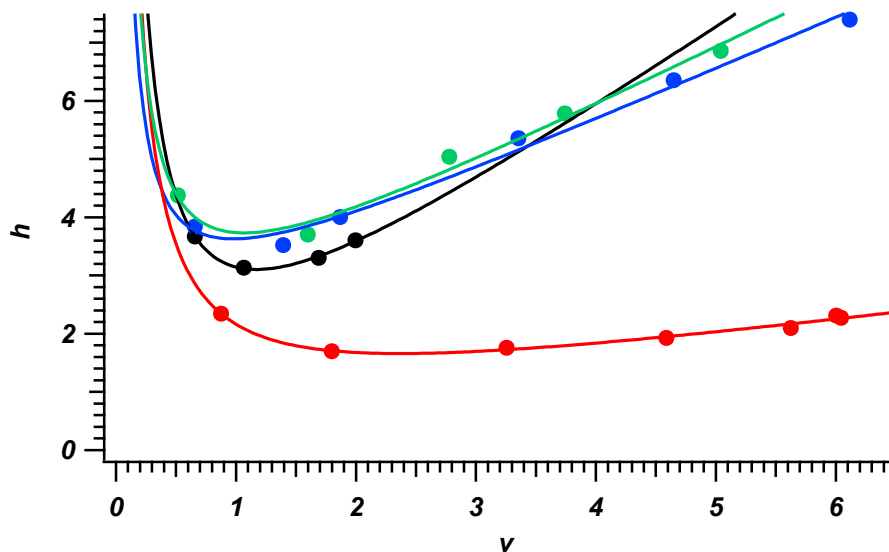


**Figure 5-1.** Plotted in black is the performance of a 100 cm x 75  $\mu\text{m}$  i.d. column packed with 1.3  $\mu\text{m}$  BEH material in a slurry with a concentration of 20 mg/mL. This column was subsequently sectioned into three subsections representing the inlet (25 cm and plotted in green), middle (32.5 cm and plotted in blue), and outlet (31 cm and plotted in red) of the original 100 cm column.

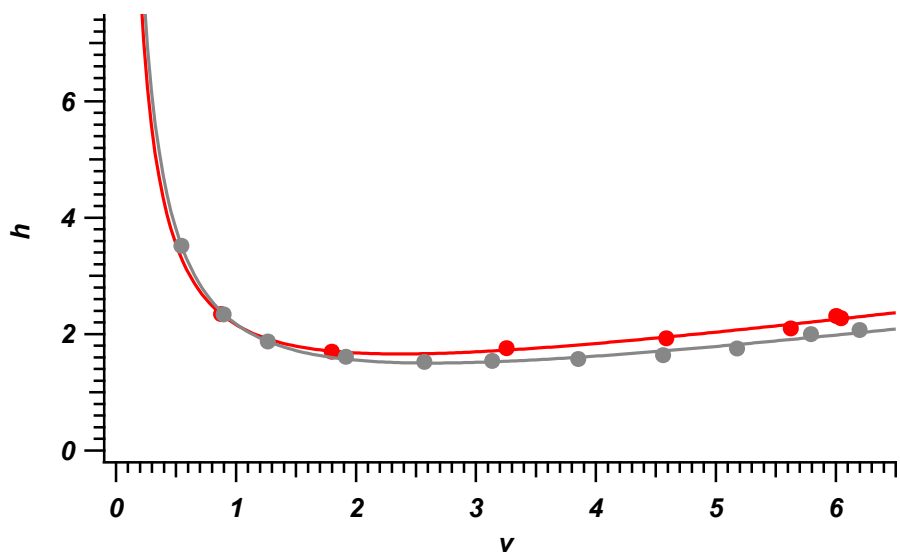


**Figure 5-2.** Overlay of the reduced van Deemter plots for the outlet subsection (31 cm long column and plotted in red in Figure 5-1, red) of the original 100 cm long column and the 34 cm long column used in the slurry optimization experiments in Chapter 2 (gray). Both columns were packed with 20 mg/mL slurries of 1.3  $\mu\text{m}$  BEH particles.

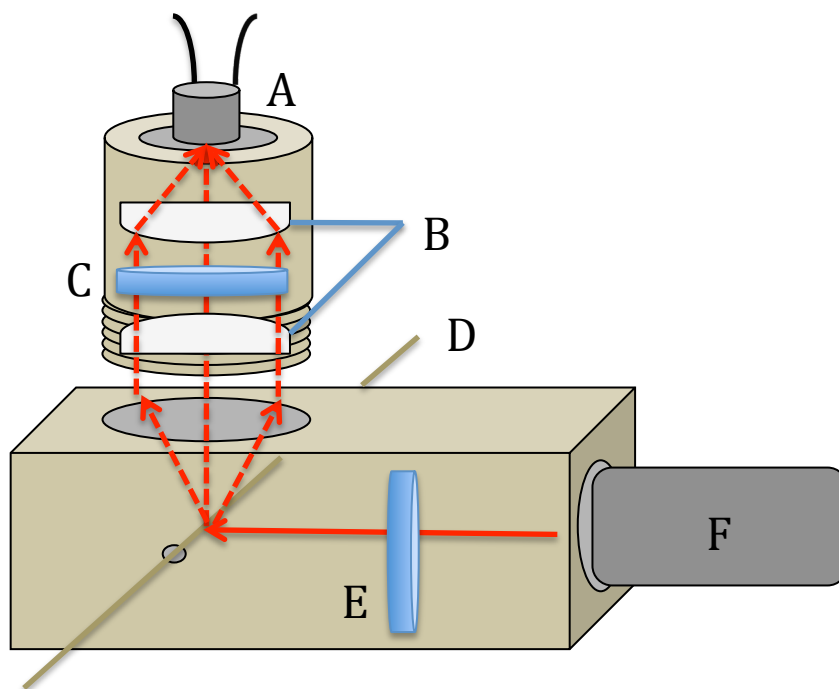


**Figure 5-3.** Diagram of the NIRF instrument. The housing is shown in tan and the components are as follows: A) Si photodiode with a spectral range of 320 to 1100 nm and peak sensitivity at 960 nm, B) plano-convex lenses, 15 mm diameter x 15 mm focal length, C) 832-center wavelength, 25 mm diameter, 37 nm bandwidth, optical density 6, fluorescence filter, D) capillary column positioning during detection, E) 780 nm center wavelength, 10 nm full width at half max, 25 mm diameter bandpass interference filter, F) 780 nm laser.

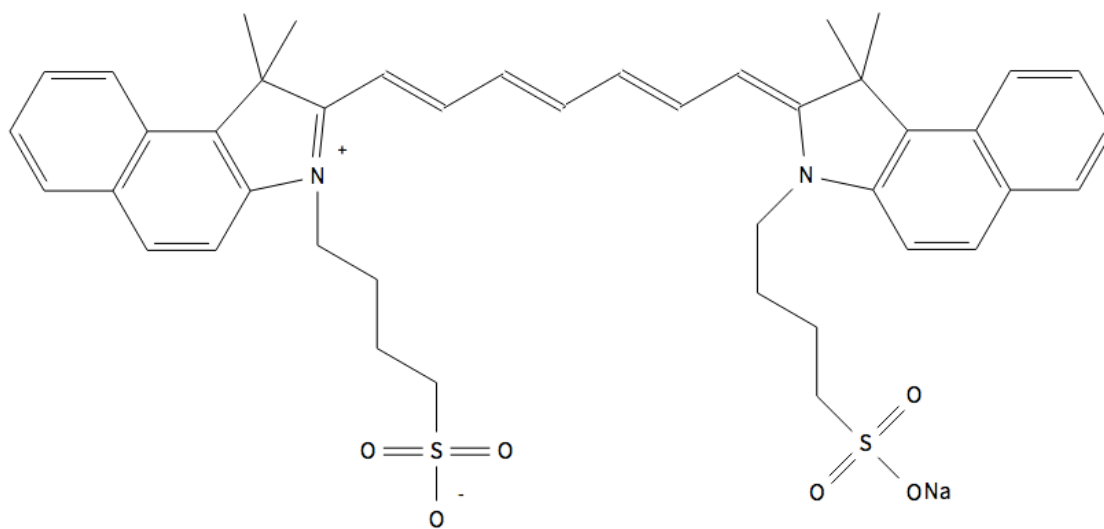


**Figure 5-4.** Structure of IR 125.

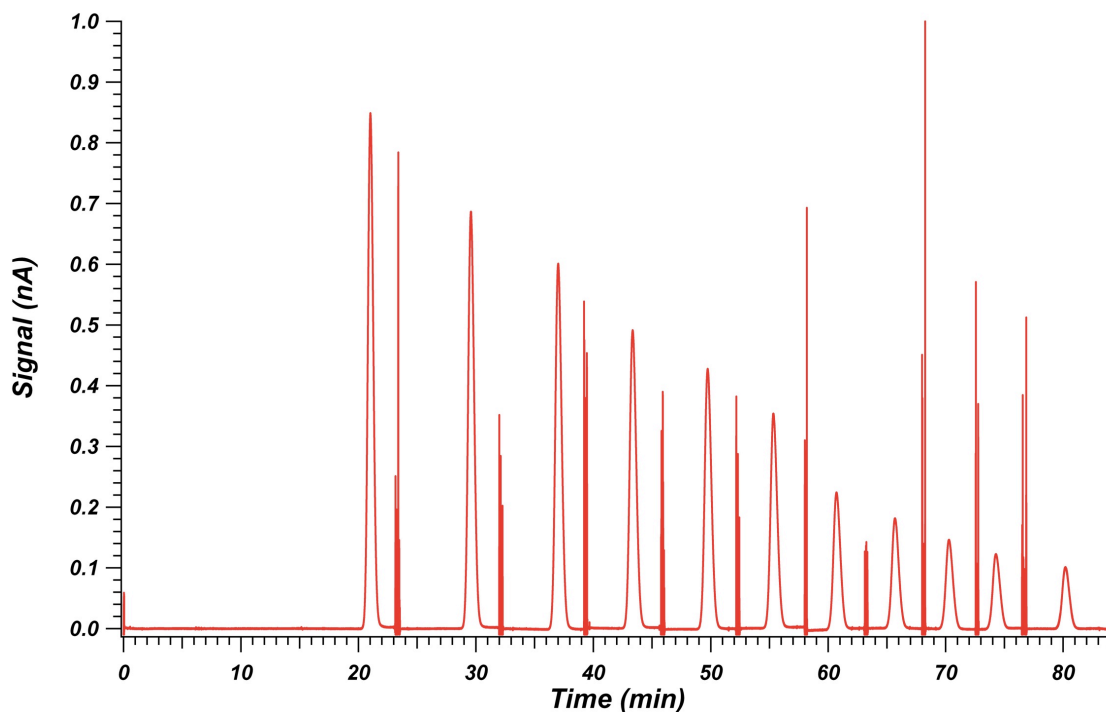


**Figure 5-5.** Example of an NIRF on-column detection experiment on a 101 cm x 75  $\mu\text{m}$  long capillary was packed with 1.9  $\mu\text{m}$  BEH particles. The first eluted peak occurs at approximately 21 minutes and corresponds to a length of 17 cm from the inlet. Each subsequent peak is the result of detection further down the column's length. Noise spikes are seen between each peak and are due to the movement of the capillary through the NIRF detector.

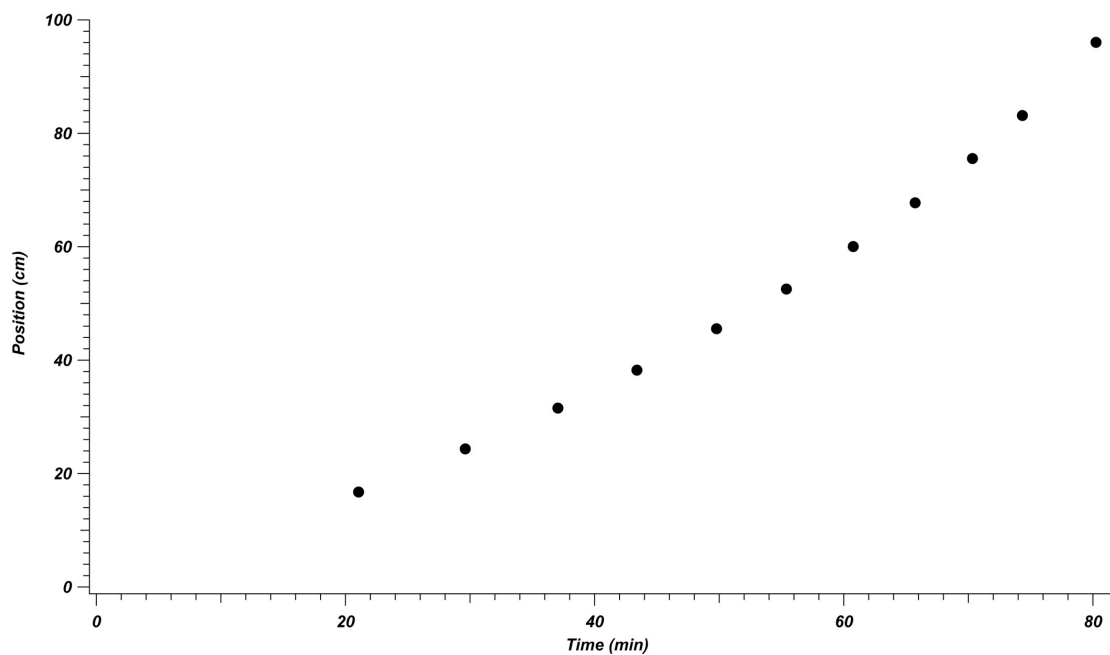


**Figure 5-6.** Plot of axial position of the on-column detection measurement for the IR125 peak vs. the time elapsed in the experiment. Data is extracted from Figure 5-5. The plot displays deviation from linearity and increasing band velocity.

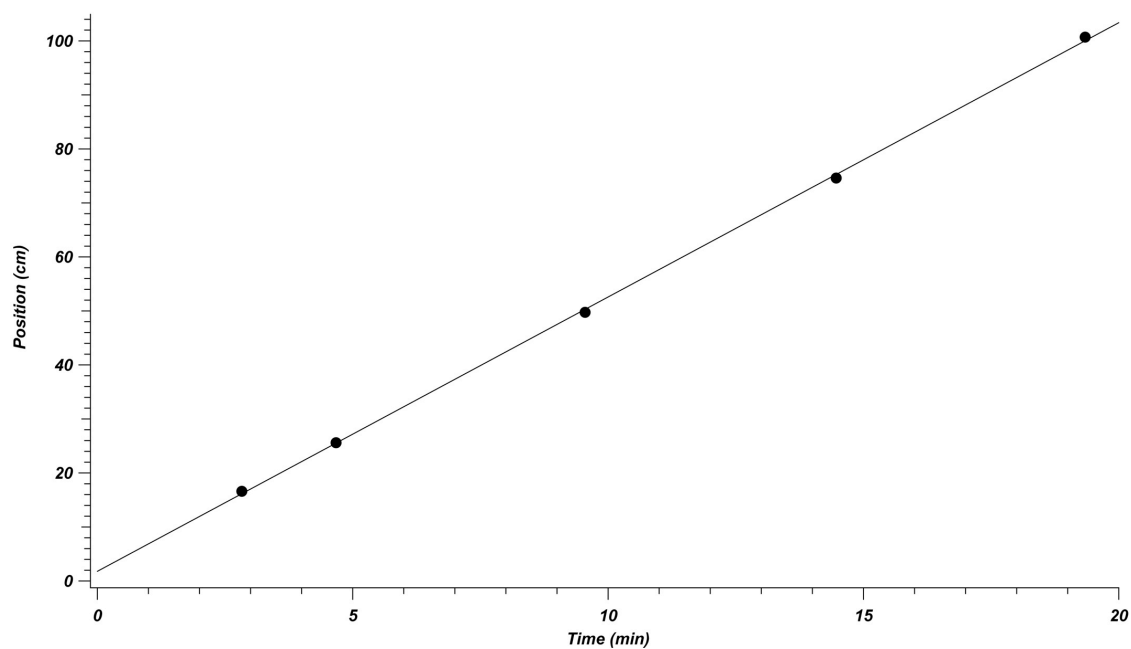


**Figure 5-7.** Plot of velocity of HQ (detection position vs. elapsed experimental time).

Linearity is seen, indicating a constant velocity of the analyte across the length of column for a 106.4 cm x 75  $\mu\text{m}$  column packed with 1.9  $\mu\text{m}$  BEH.



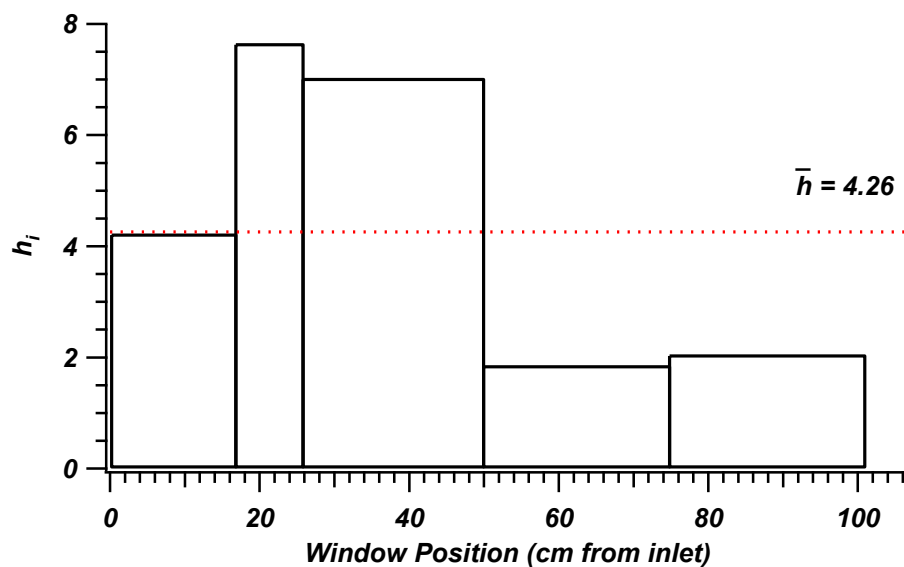


**Figure 5-8.** Plot of  $h_i$  as a function of window position in cm from the column's inlet for an on-column UV detection experiment on a 106.4 cm x 75  $\mu\text{m}$  column packed with 1.9  $\mu\text{m}$  BEH particles. Here  $\bar{h}$  is 4.26 (dashed red line) and  $h_L$  is 4.06 as measured by electrochemical detection.

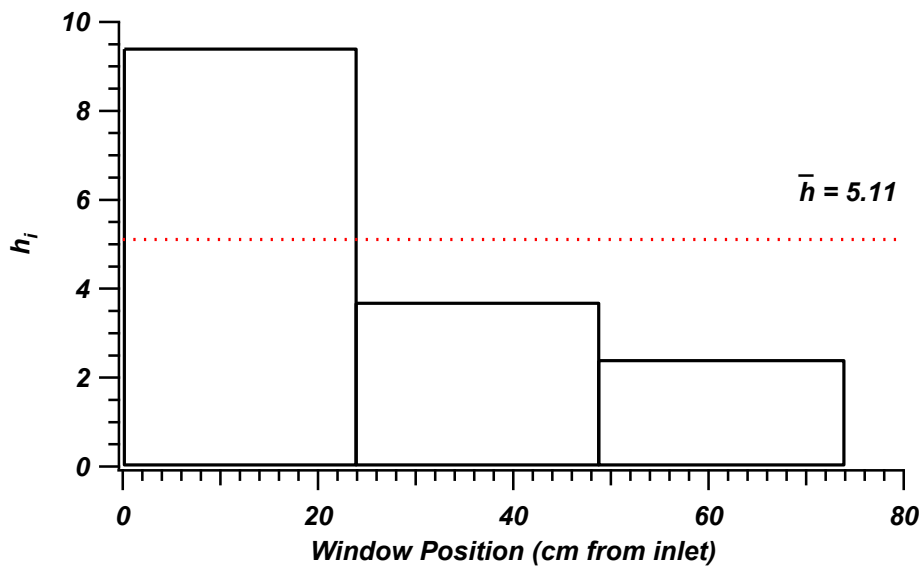


**Figure 5-9.** Plot of  $h_i$  as a function of window position in cm from the column's inlet for an on-column UV detection experiment for an 80 cm x 75  $\mu\text{m}$  column packed with 1.9  $\mu\text{m}$  BEH particles. Here  $\nu = 3.88$ , and  $h_L = 5.29$  while  $\bar{h} = 5.11$  (dashed red line). This experiment represents performance in the c-term dominated region.

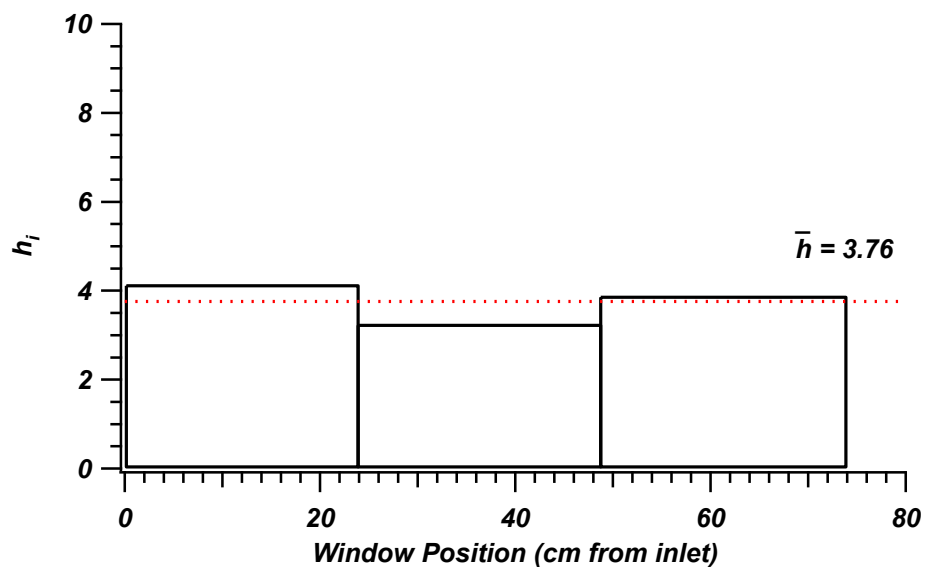


**Figure 5-10.** Plot of  $h_i$  as a function of window position in cm from the column's inlet for an on-column UV detection experiment for an 80 cm x 75  $\mu\text{m}$  column packed with 1.9  $\mu\text{m}$  BEH particles. Here  $\nu = 0.76$ , and  $h_L = 3.83$  while  $\bar{h} = 3.76$  (dashed red line). This experiment represents performance in the b-term dominated region.

## 5.8 REFERENCES

- [1] S. Bruns, J.P. Grinias, L.E. Blue, J.W. Jorgenson, U. Tallarek, *Anal. Chem.* 84 (2012) 4496–4503.
- [2] S. Bruns, E.G. Franklin, J.P. Grinias, J.M. Godinho, J.W. Jorgenson, U. Tallarek, *J. Chromatogr. A* 1318 (2013) 189–197.
- [3] A.E. Reising, J.M. Godinho, K. Hormann, J.W. Jorgenson, U. Tallarek, *J. Chromatogr. A* 1436 (2016) 118–132.
- [4] E.G. Franklin, Ph.D. Dissertation, The University of North Carolina at Chapel Hill, 2012.
- [5] J.W. Treadway, K.D. Wyndham, J.W. Jorgenson, *J. Chromatogr. A* 1422 (2015) 345–349.
- [6] D. Stickle, Ph.D. Dissertation, The University of North Carolina at Chapel Hill, 2005.
- [7] S. McWhorter, S.A. Soper, *Electrophoresis* 70 (2000) 1267–1280.
- [8] A.J. Zemann, E. Schnell, G.K. Bonn. *Anal. Chem.* 70 (1998) 563.

## Chapter 6. Hydrodynamic Chromatography as a Preparative Technique for Silica Supports Used in UHPLC<sup>3</sup>

### 6.1 Introduction

#### 6.1.1 Theory of Hydrodynamic Chromatography

Reviewed in detail by Striegel and Brewer, hydrodynamic chromatography (HDC) is a technique employed for the separation of particles based on their size [1]. The separation mechanism is dependent on the inability of larger particles to sample the slower regimes of a parabolic flow profile while smaller particles can fully sample all flow regimes. This results in a shorter residence time on-column for larger particles and thus a separation based on size.

The elution time of a particle of a given size is predictable and based on a ratio between the particle's radius and the capillary radius [1,2]. The ratio between the radius of the particle's size,  $r_p$ , and the radius of the capillary,  $r_c$ , is given by  $\lambda_{HDC}$  and presented in Equation 6-1.

$$\lambda_{Hdc} = \frac{r_p}{r_c} \quad \text{Equation 6-1}$$

Allow  $\tau_{HDC}$ , in Equation 6-2, to represent a ratio between the elution times of a particle,  $t_p$ , and small molecule dead-time marker,  $t_m$ .

$$\tau_{HDC} = \frac{t_p}{t_m} \quad \text{Equation 6-2}$$

---

<sup>3</sup> Portions of this chapter have been previously published and permission for inclusion has been granted by the publisher:

1) J.P. Grinias<sup>1</sup>, J.M. Godinho<sup>1</sup>, D.L. Lunn, J.W. Jorgenson. J. Chromatogr. A. 1370 (2014) 270–273.

Equation 6-3 presents the reduction of the model system to a single particle flowing down a capillary within a parabolic flow profile. Here the localized velocity,  $u_r$ , is presented as a function of the liquid velocity,  $u$ , at a position,  $r$ , along the capillary radius,  $r_c$ :

$$u_r = 2u \left[ 1 - \left( \frac{r}{r_c} \right)^2 \right] \quad \text{Equation 6-3}$$

The average velocity,  $u_p$ , for a particle that cannot fully probe the entirety of the parabolic flow profile due to its radius is presented in Equation 6-4 and the integral is solved in Equation 6-5:

$$u_p = \frac{2}{(r_c - r_p)^2} \int_0^{r_c - r_p} u_r \cdot r dr \quad \text{Equation 6-4}$$

$$u_p = u(1 + 2\lambda_{HDC} - \lambda_{HDC}^2) \quad \text{Equation 6-5}$$

The dead time marker and the particle of interest travel the same distance so  $\tau_{HDC}$  is equivalent to the ratio of velocities ( $u/u_p$ ). This is presented in Equation 6-6:

$$\tau_{HDC} = \frac{t_p}{t_m} = \frac{1}{1 + 2\lambda_{Hdc} - C_{HDC}\lambda_{HDC}^2} \quad \text{Equation 6-6}$$

The term  $C_{HDC}$  corrects for rotation and permeability effects that may exist for a particle and is equal to 4.89 for impenetrable, hard spheres.

HDC has a useful dynamic range of  $0.02 < \lambda_{Hdc} < 0.3$ . For a particle with diameter of 0.5-1.5  $\mu\text{m}$ , capillaries with 8  $\mu\text{m}$  radius should be used. Single capillaries, however, drastically limit throughput. In practice, packed columns are used. To mimic a series of parallel capillaries with a given radius  $r_{c,HDC}$ , columns can be packed with particles with a diameter  $d_{p,HDC}$ . This model is presented in Equation 6-7.

$$r_{c,HDC} = \frac{d_{p,HDC}}{3} \cdot \frac{\varepsilon_{interparticle}}{(1 - \varepsilon_{interparticle})} \approx \frac{2}{9} d_{p,HDC} \quad \text{Equation 6-7}$$

Assuming a packed bed with an interparticle porosity ( $\varepsilon_{interparticle}$ ) of 0.4, the HDC column should be packed with particles of  $\sim 36 \mu\text{m}$  in diameter for suitable refinement of sub-2  $\mu\text{m}$  particles.

### 6.1.2 HDC as a Preparative Technique

HDC was first experimentally demonstrated by Small to separate polystyrene latex beads [3]. Although mechanistically able to perform size refinement, the method's usefulness as a preparative technique remains largely unexplored. A preparative technique was reported previously by the Jorgenson lab to decrease the relative size distribution of a sub-2  $\mu\text{m}$  reversed phase packing material [4]. This report required an empirical column conditioning method that implemented four different mobile phases to condition the column so the particles could be suspended, singly, in acetone. The technique had the draw back of shifting retention times as the column's conditioning began to degrade. HDC on a preparative scale requires multiple injections to produce a reasonable yield of refined material. Thus, the demonstrated method was deemed not practical. Furthermore, developing a technique amenable for bare silica supports would allow for generalized batch refinement and ultimate customizability in terms of bonded phases.

## 6.2 Materials and Methods

### 6.2.1 Preparation of a HDC Column for Preparative Scale Size Refinement

32-38  $\mu\text{m}$  glass beads (GP0035, Whitehouse Scientific Ltd., Chester, UK) were rinsed in water while a magnetic stir bar was swirled to remove fine metal fragments remaining as byproducts of the sieving process during manufacture. The particles were then refluxed in a ten percent by volume solution of hydrochloric acid in water for four hours for cleaning.

Notably, a yellow tinge was removed and the particles turned bright white. After reflux, the particles were rinsed in water and dried. The dry particles were then dry packed into a 25 cm x 25 mm inner diameter glass chromatography column (Kinesis USA, Malta, NY). The packing process utilized a funnel and a PTFE tube (7/16" i.d., 1/2" o.d., McMaster-Carr, Atlanta, GA) that was continuously raised as the bed was formed to maintain a particle drop point approximately 1 cm above the formed bed. The bed was consolidated during packing by tapping the side of the column with a plastic rod. After every 2 cm of bed formed, the column was tapped vertically to further consolidate the bed. A 10  $\mu$ m Stainless steel mesh frit (TWP, Inc., Berkely CA) inserted into the adjustable endfitting (Kinesis USA, Malta, NY) was used at the column inlet while a non-adjustable fitting was used for the outlet. This outlet fitting (Kinesis USA, Malta, NY) used an identical 10  $\mu$ m stainless steel mesh frit. However, this frit was secured in place with a silicone sealant (DAP Products, Baltimore, MD) at the frit's edge. A Waters 600 quaternary HPLC pump (Waters Corp. Milford, MA) delivered flow through the column. Bed consolidation was conducted by directly connecting the column inlet with a 0.0625" i.d. PTFE tubing to the pump for a delivery of deionized water (Nanopure ultrapure water system Barnstead International, Dubue, IA) at 2 mL/min. After complete filling of the column (visible through the columns clear glass walls) the flow rate was increased to 4 mL/min. The adjustable endfitting was then tightened to meet the consolidated bed to decrease dead volume. The column's final length was 22 cm.

### **6.2.2 Implementation of the HDC Column**

The HPLC pump was then connected to a six-port VICI electronic injector (Valco Instruments, Co., Inc.) with a 1 mL sample loop. The inlet of the column was connected to the injector with a 30 cm x 0.254 mm i.d. PEEK tube while the outlet was connected to a 60



cm x 600  $\mu\text{m}$  o.d. 300  $\mu\text{m}$  i.d. fused-silica capillary (Polymicro Technologies, Phoenix, AZ). A section of the polyimide coating was removed to create a detection window and UV absorbance detection, turbidity, was conducted with a Linear UV/Vis 200 detector (Thermo Scientific, Waltham, Ma) at 216 nm. Deionized water was tested as a mobile phase, but 1 mM ammonium hydroxide (ACS grade, Fischer Scientific, Hampton, NH) was determined more appropriate. A flow rate of 3 mL/min ensured the system pressure did not exceed the 150 psi rating of the glass column. Prior to daily operation the system was flushed for 60 min, approximately 4 column volumes, to bring the pH of the mobile phase measured at the outlet to  $\sim 10$ . After use, the column was flushed with deionized water for 60 min before shut down to reduce the pH and prevent column degradation.

### **6.2.3 HDC Column Characterization and Analysis of Silica Particles**

Non-porous silica (NPS) size standards (Fiber Optic Center, Inc. New Bedford, MA) of 0.5  $\mu\text{m}$  and 1.5  $\mu\text{m}$  were slurried in mobile phase. Urea (ACS grade, Sigma Aldrich, St. Louis, MO) was added as a dead time marker. Particle recovery was determined with 10 mg/mL slurries of each size standard made from predetermined particle amounts. 1 mL samples of which were injected and collected until the slurry was fully used. Collected material was then washed with deionized water, centrifuged, dried and weighed.

Characterization with bridged-ethyl hybrid (BEH) particles of  $\sim 1.0 \mu\text{m}$  diameter (Waters Corp. Milford, MA) were slurried at 10 mg/mL in mobile phase. The eluting particle peak was split into two fractions at the peak maximum, 12.4 min after injection. Particle size distributions (PSD) were determined using scanning electron microscopy (SEM) with a Hitachi S-4700 cold cathode field emission SEM equipped with a Through the Lens detector (Tokyo, Japan). Images were processed with Image J to measure particle size and statistical

analysis was conducted in Microsoft Excel. Igor Pro 6.0 (Wavemetrics, Inc., Lake Oswego, OR) was used for graphical representation and plate count. Theoretical plates were calculated from the base width of Gaussian peak fits.

## **6.3 Results and Discussion**

### **6.3.1 Determination of Mobile Phase Suitability by Separation of Size Standards**

Essential to efficient HDC is the continuous isolation of all particles traversing the packed HDC column. As described in the derivation above, smaller particles are able to sample more of the flow paths within the column and thus separate from larger particles. Thus, any agglomeration or adhesion forces between particles would prove greatly detrimental to the preparative purification.

Previous reports had worked to separate already bonded silica particles with n-octyldecyl (C18) functionality [4]. It was our goal however, to separate particles prior to the bonding process with a generalized HDC methodology that could be implemented for all silica beads independent of internal morphology (non-porous, fully porous, etc.). With this approach, bulk material could be processed and refined prior to appropriate bonding according to the application at hand.

With C18 surface modification, acetone was chosen as the solvent for its generally low inclination towards aggregation in the limit of very low slurry concentrations. However, previous reports of preparative scale HDC required significant column conditioning to avoid interactions between the packed column's idealized capillary channels and the material being refined.

The approach reported here instead wanted to make use of the natural repulsions between silanols on the surface of the glass beads in the HDC column and the silanols on the

silica particles' surfaces. Attempts were made to use deionized water as the mobile phase, which should allow for adequate repulsion. Figure 6-1 presents a HDC separation of NPS with water injections and mobile phase. Here, plate counts were 750 and 1110 for 0.5  $\mu\text{m}$  and 1.5  $\mu\text{m}$  NPS standards respectively. It was postulated however, that a slightly basic pH would help enrich the overall surface charge and increase repulsion. In Figure 6-2, increased separation performance is seen for the 0.5 and 1.5  $\mu\text{m}$  NPS standards ( $N \sim 1780$  and 1700 respectively) and so 1 mM ammonium hydroxide was chosen as the mobile phase moving forward.

### **6.3.2 HDC Column and Packing Quality**

To characterize the quality of the packed column, the performance of a small dead time marker, urea, was assessed. Previous reports of the 17 cm x 25 mm i.d. produced a plate count of approximately 3000 and a reduced plate height of  $\sim 1.6$ . For the column reported here, 22 cm x 25 mm i.d. urea produced approximately 2600 plates and a reduced plate height of 2.5. Theoretically, HDC's efficiency is dominated by convective mixing and which suggests a value of 1.4 [1]. Further pursuit of this method could greatly benefit by refinement in column packing, which may be key for advancement of the technique.

Although the peak associated with urea is an important measure of efficiency, more insight into the column's usefulness as a preparative method is gained by the relative drop in performance of a size standard in comparison to the small molecule marker. This is because broad particle peaks will represent a wider size distribution upon elution, especially as a sample with an inherent particle size distribution is refined. Compared to the efficiency drop of the previously reported acetone methodology, the efficiency of a 0.5  $\mu\text{m}$  NPS standard for this column only drops by  $\sim 30\%$  as opposed to  $\sim 40\%$ . The lower previously reported

separation efficiency is likely due to particle aggregation in the mobile phase. Figure 6-3 presents an example separation of 1.5 and 0.5  $\mu\text{m}$  NPS standards overlaid on individual injections of 0.5 and 1.5  $\mu\text{m}$  NPS standards. Notably a clear indication of two separate underlay peaks exists in the separation of size standards and is indicative of well dispersed particles.

### **6.3.3 Particle Recovery for NPS Standards**

The ability of the technique to act as a preparative method for particle size refinement is dependent on the throughput and recovery of the material refined in the column. To test this, known masses of 0.5 and 1.5  $\mu\text{m}$  NPS particles were slurried individually in mobile phase at a concentration of 10 mg/mL. Repeated injections were made and the entire eluted peak was collected for each injection. Collected samples were then washed and dried for particle recovery measurements. Here, 86% of the 0.5  $\mu\text{m}$  NPS standards and 74% of the 1.5  $\mu\text{m}$  standards were recovered. General recovery of larger particles is lower and likely due to trapping of the particles within the column frits. Some yield reduction is also likely due to the washing procedures but should not affect direct comparison of the two size standards as both were processed identically. Detailed results of these experiments are presented in Table 6-1.

### **6.3.4 Size Refinement and Recovery of 1.0 $\mu\text{m}$ BEH Particles by HDC**

NPS size standards have a low relative size distribution (RSD) (<10%) and are suitable for method development. Alternatively, actual samples, such as sub 2-  $\mu\text{m}$  porous particles, typically have a much wider PSD that can be reduced with HDC and fractionation of the eluted particle peak. Characterization of the HDC column as a preparative refinement system was done by refining 0.9  $\mu\text{m}$  BEH particles. Injections were made repeatedly at a 10 mg/mL slurry concentration and the 1<sup>st</sup> and 2<sup>nd</sup> half of the eluted peak (in time) were

collected separately. Using the ammonium hydroxide mobile phase allowed for very reproducible separations, which allowed the cut off time for the front and back half of the peak to be maintained at 12.4 minutes after the injection. Results of this experiment are presented in Figure 6-4 (A,B,C). Here, histograms present the size distribution of the raw material (A), the 1<sup>st</sup> half of the peak (B), and the 2<sup>nd</sup> half (C). The raw material had a relative size distribution of 24%. The 1<sup>st</sup> half was reduced to 16% and the tailing portion dropped to 19%. The refinement of the particle batch is clear and fine particles, that can greatly increase the final packed analytical columns' flow resistance, can be removed with this fractionation and HDC technique.

Material recovery was again assessed and the results are presented in Table 6-1. The recovery of the injected BEH material was 88% with 36% in the first fraction and 52% in the second. The total time required for the recovery of the 31 mg of larger BEH material that eluted in first fraction was less than 2 hours. This is achieved by staggering injections as the material elutes in a narrow window.

### **6.3.5 Refinement of Ultrasonic Spray Pyrolysis Particles**

A novel material synthesized by ultrasonic spray pyrolysis (USP) yields particles with a wide range of physical morphologies and sizes [5]. An example SEM image highlighting the diversity is shown in Figure 6-5. It was noticed, through SEM imaging and data work up, that the larger material typically had a macroporous microstructure (of possible interest as a novel chromatographic support [6]) and thus, HDC was selected to refine and increase the population of this material within a collected fraction.

Feasibility of HDC for refinement of the USP material was assessed and is displayed in Figure 6-6. Here the overlay of the elution of the raw USP material is presented with 0.5

an 1.5  $\mu\text{m}$  size standards. It is clear that the eluting peak falls within the range of fractionation available based on the HDC column's packing material. The refinement of material implemented a repeated injections scheme (Figure 6-7) as the elution time of the material and robustness of the single mobile phase method allows for discreet elution windows and staggering injections. For the fractionation of the USP materials the fractions were cut at the apex of the eluting peak, 12 minutes after each injection. Example images of the resulting refinement are presented in Figure 6-8a and b where a clear difference in sample diversity is seen. The data for the resulting fractions is divided into the three particle morphologies; macroporous, hybrid and microporous as described by the example particle types shown in Figure 6-5 and presented graphically in Figure 6-9. Notably, the populations of particle type for a single eluted and fractioned peak are nearly identical to the populations for the summation of 10 repeated injections, demonstrating the repeatability of the method. Moreover, refinement is seen as the fraction of population representing the larger macroporous material increasing while the microporous material decreases. Table 6-2 presents the relative particle diameters for each of the fractions with respect to morphology. Compared to the raw material, the diameters after HDC for one injection is almost identical. This means the method conserves the size distribution but, when taken in conjunction with Figure 6-9, enriches the target material. After 10 injections and fractionation, the particle diameters on average are slightly lower for the macroporous material (possibly due to the columns inherent trapping of larger materials). In all, proof of concept for this HDC preparative technique is shown. Particles are refined based on size, and a target population with a specific morphology is enriched due to fractionation.

#### **6.4 Conclusions**

Presented here is a report of improvements and implementation towards preparative HDC. The method effectively reduces the PSD of sub-2  $\mu\text{m}$  fully porous particles, and novel USP particles that exhibit not only a range in sizes but also structural features. Proof of concept was shown for water as a mobile phase and enhancement in separation efficiency was seen when the inherent surface charge is amplified with an ammonium hydroxide mobile phase. Particle elution times when using the single mobile phase procedure presented are highly reproducible and allow for repeated injections and increased throughput per unit time. The applicability and universal nature of this method for the refinement of bare silica allows for applicability to any type of silica chromatographic support prior to bonding.

## 6.5 Tables

<u>Particle Type and Size</u>	<u>Mass Injected (mg)</u>	<u>Mass Recovered (mg)</u>	<u>Yield</u>
0.5 $\mu\text{m}$ NPS	35.4	30.4	86%
1.5 $\mu\text{m}$ NPS	39.0	28.8	74%
0.9 $\mu\text{m}$ BEH Fraction 1	N/A	31.2	36%
0.9 $\mu\text{m}$ BEH Fraction 2	N/A	51.9	52%
0.9 $\mu\text{m}$ BEH Total	87.4	76.6	88%

**Table 6-1.** Presentation of the mass injected, mass recovered and the overall percent yield for NPS standards used to characterize the column and porous BEH material.



	<u>Macroporous</u>	<u>Hybrid</u>	<u>Microporous</u>	<u>Number Sized</u>
1 injection 1 <sup>st</sup> half	1.45 $\mu\text{m}$	1.27 $\mu\text{m}$	1.01 $\mu\text{m}$	151
1 injection 2 <sup>nd</sup> half	1.20 $\mu\text{m}$	1.06 $\mu\text{m}$	0.80 $\mu\text{m}$	106
10 injections 1 <sup>st</sup> half	1.35 $\mu\text{m}$	1.37 $\mu\text{m}$	0.95 $\mu\text{m}$	188
Raw material	1.47 $\mu\text{m}$	1.26 $\mu\text{m}$	0.93 $\mu\text{m}$	118

**Table 6-2.** Results of USP particle size refinement with HDC. The data is presented in terms of the first and second half of the eluting particle peak with individual notation of average particle diameter of the three different microstructure populations. Comparison is also made between the results of a single injection and a repeated throughput of 10 injections in a row. For comparison the particle diameter is provided for each particle type for the raw, unrefined material.

## 6.6 Figures

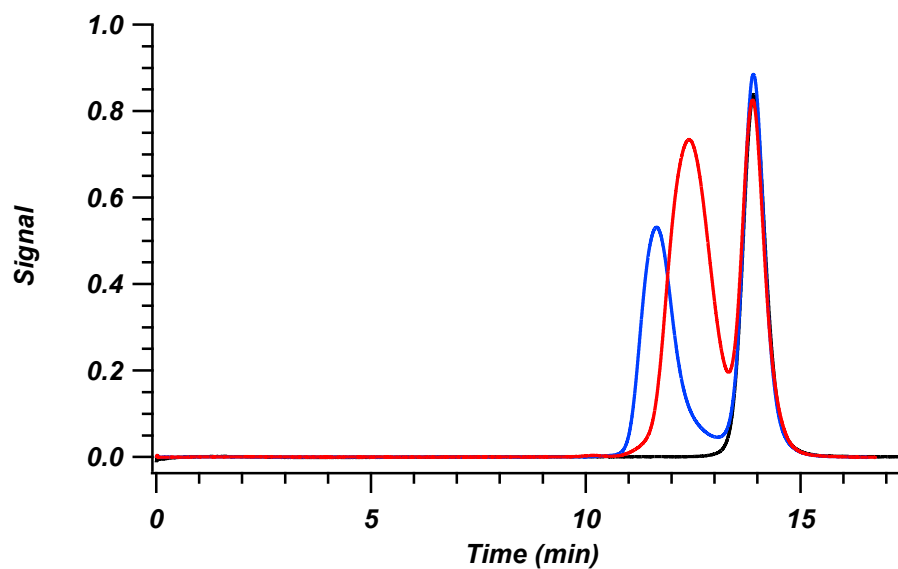


**Figure 6-1.** HDC runs of 0.5  $\mu\text{m}$  (red) and 1.5  $\mu\text{m}$  (blue) NPS standards. Here water is used as a mobile phase. For comparison the eluted peak for urea is plotted in black.

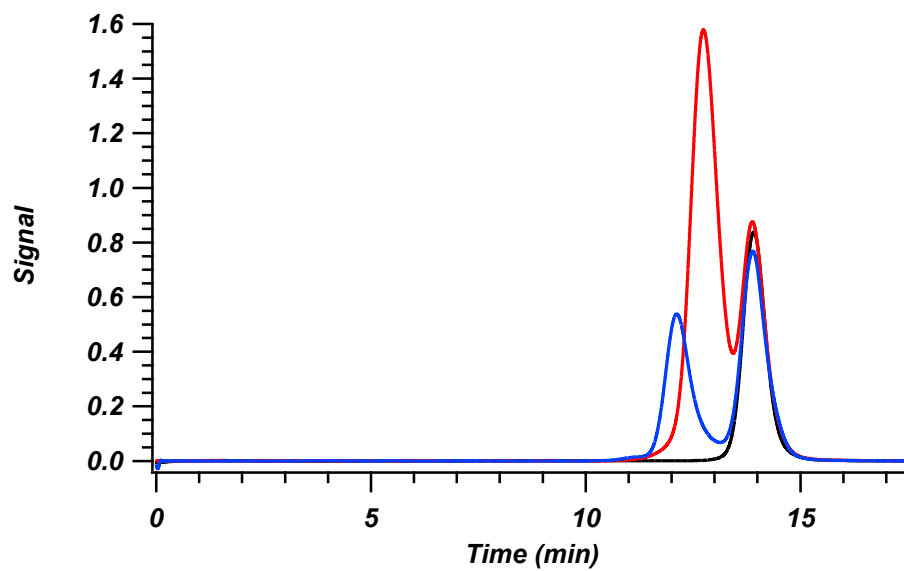


**Figure 6-2.** HDC runs of 0.5  $\mu\text{m}$  (red) and 1.5  $\mu\text{m}$  (blue) NPS standards with 1 mM ammonium hydroxide used as a mobile phase. For comparison the eluted peak for urea is plotted in black.

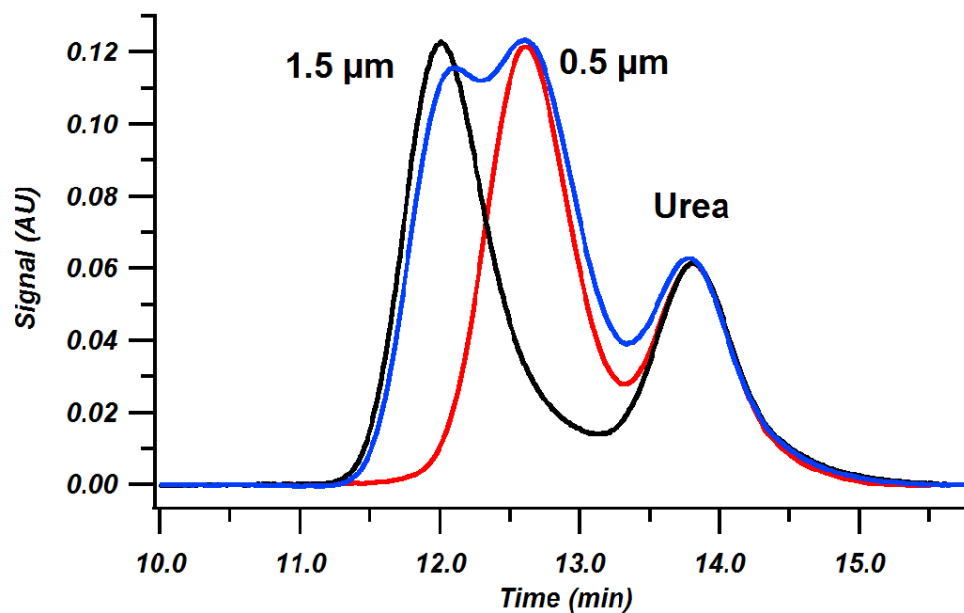


**Figure 6-3.** HDC separation of 1.5 and 0.5  $\mu\text{m}$  NPS size standards when injected together (blue). Overlaid are reference chromatograms for injections containing just one of the two size standards (1.5  $\mu\text{m}$  in black and 0.5  $\mu\text{m}$  in red).

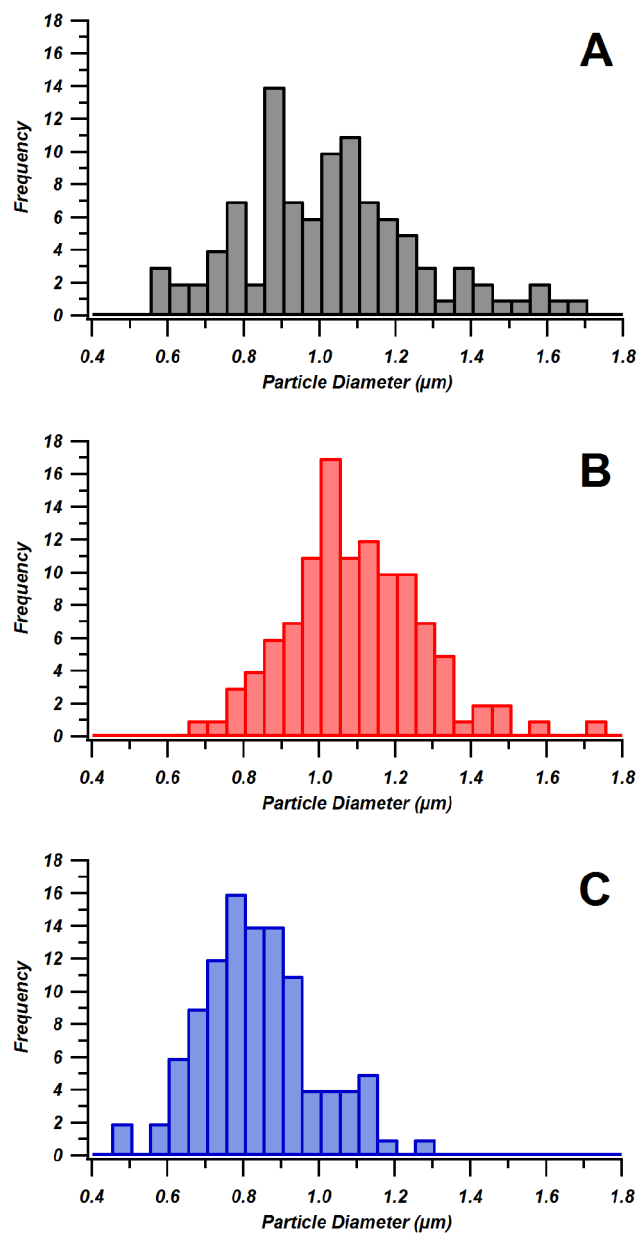


**Figure 6-4.** Histograms for the data representing the refinement of 0.9 μm BEH material.

Figure A represents the raw PSD while frames B and C represent the 1<sup>st</sup> and 2<sup>nd</sup> halves of the eluted BEH peak respectively. A clear difference in PSD is seen as a function of fractionation. The number of particles sized for each panel: A) 101 B) 112 C) 105.

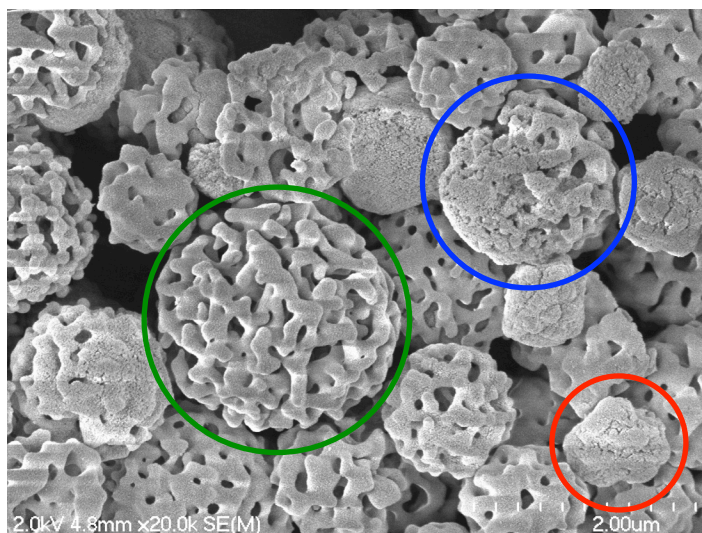


**Figure 6-5.** Overview image for the diversity in particle structure created when synthesizing sub-2  $\mu\text{m}$  particles by USP. The three particle types characterized in the discussion presented herein are circled: macroporous (green), hybrid (blue), microporous (red).

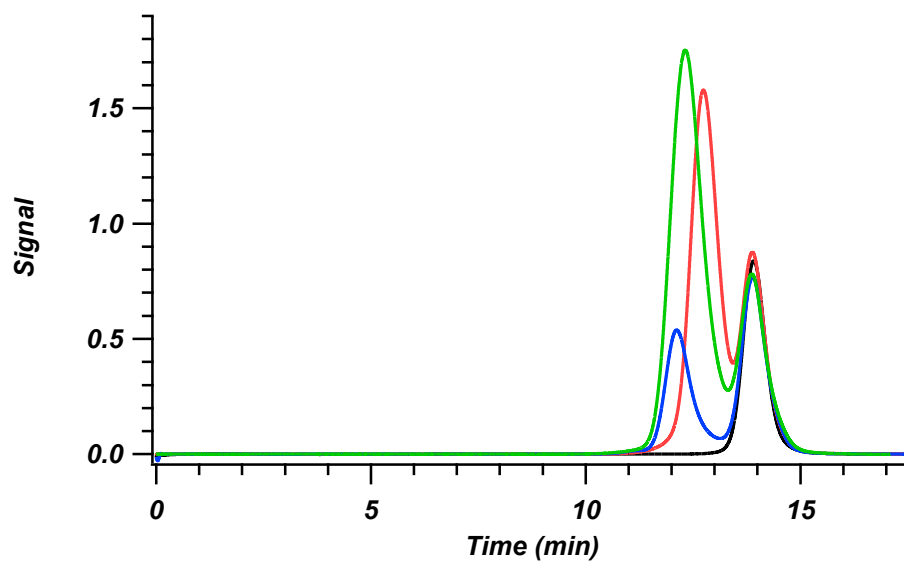


**Figure 6-6.** Overlay of the eluted USP peak (green), on HDC runs of 0.5 (red) and 1.5 (blue)  $\mu\text{m}$  NPS, and urea (black) demonstrating the suitability of the column and method for material in this size range.

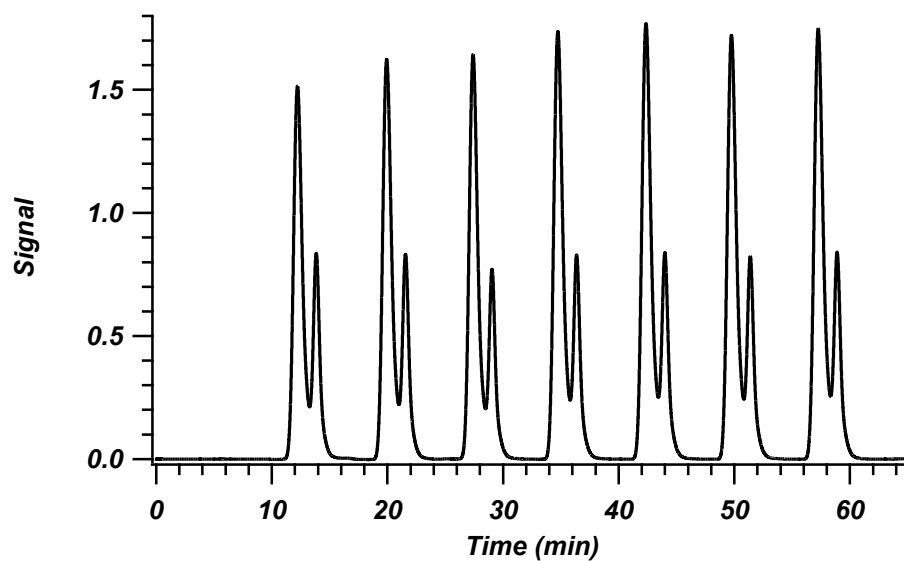
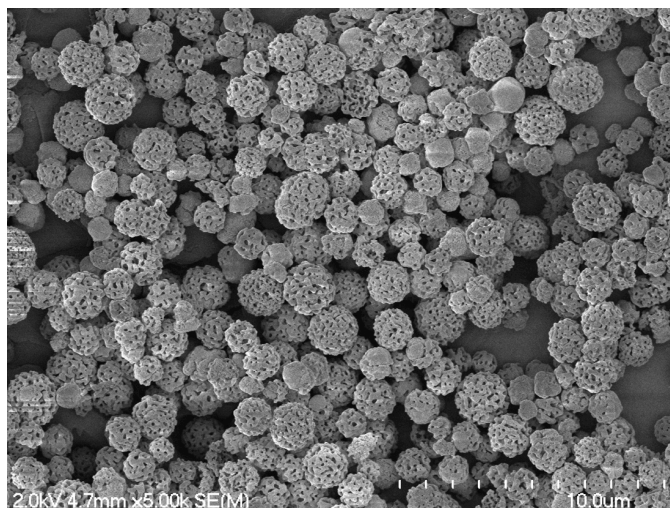


**Figure 6-7.** Example 1 hour run with staggered injections for the refinement of USP material. For each two peak pair, the first eluting peak was split into a 1<sup>st</sup> and 2<sup>nd</sup> fraction at the peak's maximum intensity. The second peak in each pair represents the elution of urea.



A)



B)

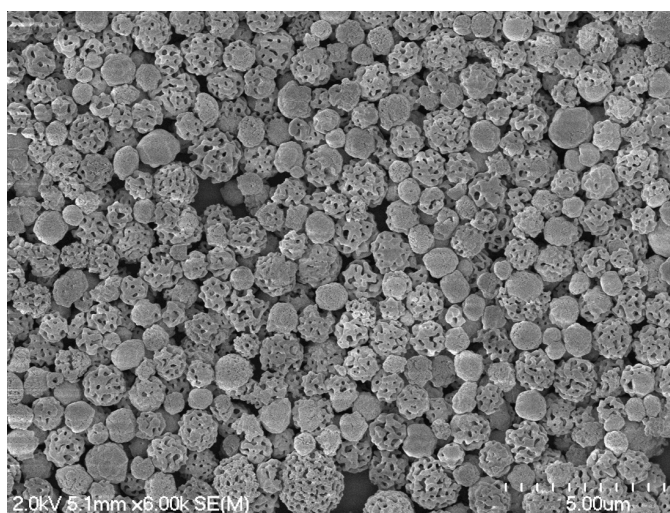


**Figure 6-8.** Panel A is an representative SEM image of the 1<sup>st</sup> eluting half of the USP peak. A clear population of larger, hybrid material is detectable by eye. Panel B is a representative SEM image for the 2<sup>nd</sup> half of the eluting USP peak and portrays a significant number of smaller particles that do not have the characteristic macroporous features.

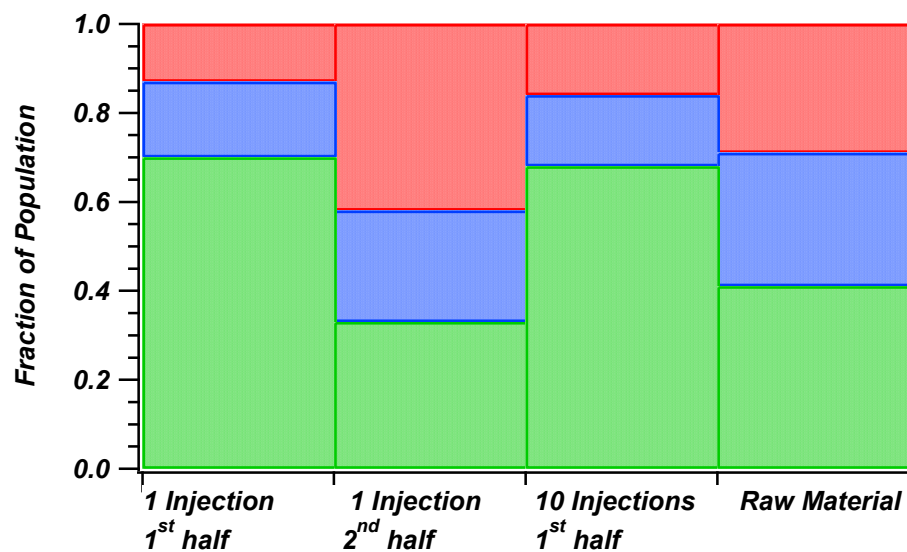


**Figure 6-9.** Graphical representations of the fraction of population for the 1<sup>st</sup> and 2<sup>nd</sup> half of a fractioned USP peak. The results of 10 repeated injects are also shown and all are compared to the raw material. Green represents the larger macroporous material, blue the hybrid, and red the microporous. The number of sized particles is listed in Table 6-2.

## 6.7 REFERENCES

- [1] A.M. Striegel, A.K. Brewer, *Ann. Rev. Anal. Chem.* 5 (2012) 15–34.
- [2] R. Tijssen, J. Bos, M.E. van Kreveld, *Anal. Chem.* 58 (1986) 3036–3044.
- [3] H. Small, *J. Colloid Interface Sci.* 48 (1974) 147–161.
- [4] W. Thompson, R.A. Lieberman, J.W. Jorgenson, *J. Chromatogr. A* 1216 (2009) 7732–7738.
- [5] A.K. Peterson, D.G. Morgan, S.E. Skrabalak, *Langmuir* 26 (2010) 8804–8809.
- [6] W. Smits, K. Nakanishi, G. Desmet, *J. Chromatogr. A* 1429 (2016) 166–174.

## **APPENDIX 1: MATERIALS AND METHODS**

Outlined here is a listing of materials and methods used for the packing and characterization of the majority of capillary columns presented in the preceding chapters. Specific experimental conditions and any departure from that listed and outlined here will be noted in the appropriate sections.

### **1. Chemicals and Materials**

Slurry packing of capillary columns was conducted with pushing and slurry solvents received from Fisher Scientific (St. Louis, MO). These solvents were HPLC grade and consisted of acetone and tetrahydrofuran (THF). HPLC grade acetonitrile (MeCN), reagent grade trifluoroacetic acid (TFA), and the test analytes for isocratic evaluation L-ascorbic acid (AA), 1,4-dihydroxybenzene (hydroquinone: HQ), 1,3-dihydroxybenzene (resorcinol: RES), 1,2-dihydroxybenzene (catechol: CAT) and 4-methylcatechol (4MC) were also obtained from Fisher Scientific (St. Louis, MO). Kasil frits for the packed capillaries were prepared with potassium silicate from PQ Corporation (Valley Forge, PA), and formamide from Sigma–Aldrich (St. Louis, MO). 75  $\mu\text{m}$  i.d. cylindrical fused-silica tubing was purchased from Polymicro Technologies (Phoenix, AZ). The capillaries were packed with bridged ethyl hybrid (BEH) particles provided by Waters Corporation (Milford, MA). Particle batches used ranged in size and will be noted in the appropriate section. BEH particles were bonded with n-octyldecyl (C18) by the manufacturer and used as received. Deionized water was obtained from a Nanopure ultrapure water system (Barnstead International, Dubuque, IA).

### **2. Chemicals and Methods Used for Slurry Packing and Column Creation**

The method of slurry packing has been described in detail elsewhere and will be presented briefly here [1-7]. Column blanks were fritted using the Kasil method [8]. Slurries

with a specific concentration were prepared by mixing a known mass of the particles in a known volume of slurry solvent. The particles were suspended with a 10 min sonication cycle prior to packing using a Cole Parmer Ultrasonic Cleaner 8891 (Vernon Hills, IL).

The slurry was then placed into a packing reservoir and the column blank was secured to the reservoir using an UHPLC fitting. Packing was initiated using acetone as a pushing solvent at 150 bar from a DSHF-300 Haskel pump (Burbank, CA). The packing pressure was increased until a final pressure of 2000 bar was reached. The column was allowed to pack until a desired bed length was reached. Then, the packing pressure was slowly released to atmospheric pressure. The column was then connected to a DSXHF-903 Haskel pump (Burbank, CA) using an UHPLC injection apparatus [2]. Each column was flushed for 1 h in 50:50 (v/v) water:MeCN + 0.1% TFA at 3500 bar, after which the pressure was gradually released and reinitiated at 700 bar to form a temporary inlet frit with a heated wire stripper from Teledyne Interconnect Devices (San Diego, CA). Columns were then clipped to a final bed length and an inlet frit was installed using the Kasil method.

### **3. Column Characterization**

Column efficiency was tested under isocratic elution conditions using 200  $\mu$ M of a test mixture (AA, dead-time marker; HQ, RES, CAT, and 4MC) and the UHPLC injection apparatus. The mobile phase used for evaluation was 50:50 (v/v) water:MeCN + 0.1% TFA. Analytes were detected amperometrically. Electrochemical detection was conducted at a 8  $\mu$ m  $\times$  300  $\mu$ m carbon fiber microelectrode held at +1.1 V vs. Ag/AgCl reference electrode [9]. This electrode was placed at the outlet of the UHPLC column. Current-to-voltage conversion was conducted using an SR750 current amplifier (Stanford Research Systems, Sunnyvale, CA) with a  $10^9$  V/A gain and a 3 Hz, 3 dB low-pass bandwidth filter. An Intel

Core 2 Duo desktop computer with a 16-bit A/D converter was used to acquire data at 21 Hz. Data were collected with a custom-written LabView 6.0 program (National Instruments, Austin, TX). Columns were analyzed over a range of mobile phase velocities to create plots of the plate height  $H$  vs. the average mobile phase velocity  $u_{av}$  for each analyte in the test mixture. High frequency noise was removed from the chromatograms using a digital frequency filter and low frequency baseline drift was eliminated by background subtraction. Retention times and theoretical plate counts,  $N$ , were determined using an iterative statistical moments algorithm written in Igor Pro 6.0 (Wavemetrics, Inc., Lake Oswego, OR) [4]. Briefly, the program eliminates operator bias by arbitrarily defining the beginning and end of each peak and an iterative marking process is used to mark the limits of integration. The program uses these values to calculate the first and second central moment. From the second central moment a standard deviation is obtained. Using this value the peak is then marked for  $\pm 3\sigma$  from the first moment. The program then calculates new values for the second moment and the standard deviation. If the value of the second moment differs by more than 1% the process is reiterated using the new standard deviation to mark  $\pm 3\sigma$  from the peak center. The process continues until the change in variance is less than 1%. The final values for the moments are then used to calculate  $N$ .

#### 4. REFERENCES

- [1] L.E. Blue, J.W. Jorgenson, *J. Chromatogr. A* 1380 (2015) 71–80.
- [2] J.W. Treadway, K.D. Wyndham, J.W. Jorgenson, *J. Chromatogr. A* 1422 (2015) 345–349.
- [3] E.G. Franklin, Ph.D. Dissertation, The University of North Carolina at Chapel Hill, 2012.
- [4] S. Hsieh, J.W. Jorgenson, *Anal. Chem.* 68 (1996) 1212–1217.
- [5] J.S. Mellors, J.W. Jorgenson, *Anal. Chem.* 76 (2004) 5441–5450.
- [6] K.D. Patel, A.D. Jerkovich, J.C. Link, J.W. Jorgenson, *Anal. Chem.* 76 (2004) 5777–5786.
- [7] R.T. Kennedy, J.W. Jorgenson, *Anal. Chem.* 61 (1989) 1128–1135.
- [8] A. Maiolica, D. Borsotti, J. Rappsilber, *Proteomics* 5 (2005) 3847–3850.
- [9] L.A. Knecht, E.J. Guthrie, J.W. Jorgenson, *Anal. Chem.* 56 (1984) 479–482.